2011-12

An observational study of tropical cyclone spin-up in Supertyphoon Jangmi and Hurricane Georges

Sanger, Neil T.

Monterey, California. Naval Postgraduate School

NAVAL POSTGRADUATE SCHOOL

MONTEREY, CALIFORNIA

DISSERTATION

AN OBSERVATIONAL STUDY OF TROPICAL CYCLONE SPIN-UP IN SUPERTYPHOON JANGMI AND HURRICANE GEORGES

by

Neil T. Sanger

December 2011

Dissertation Supervisor: Michael T. Montgomery

Approved for public release; distribution is unlimited

THIS PAGE INTENTIONALLY LEFT BLANK

REPORT DOCUMENTATION PAGE			Form Approved OMB No. 0704-0188
Public reporting burden for this collection of information is estimated to average 1 hour per response, including the time for reviewing instruction, searching existing data sources, gathering and maintaining the data needed, and completing and reviewing the collection of information. Send comments regarding this burden estimate or any other aspect of this collection of information, including suggestions for reducing this burden, to Washington headquarters Services, Directorate for Information Operations and Reports, 1215 Jefferson Davis Highway, Suite 1204, Arlington, VA 22202-4302, and to the Office of Management and Budget, Paperwork Reduction Project (0704-0188) Washington DC 20503.			
1. AGENCY USE ONLY ***(Leave blank)***	**2. REPORT DATE** December 2011	**3. REPORT TYPE AND DATES COVERED** Dissertation	
4. TITLE AND SUBTITLE: An Observational Study of Tropical Cyclone Spin-Up in Supertyphoon Jangmi and Hurricane Georges		**5. FUNDING NUMBERS**	
6. AUTHOR(S) Neil T. Sanger			
7. PERFORMING ORGANIZATION NAME(S) AND ADDRESS(ES) Naval Postgraduate School Monterey, CA 93943-5000		**8. PERFORMING ORGANIZATION REPORT NUMBER**	
9. SPONSORING / MONITORING AGENCY NAME(S) AND ADDRESS(ES) N/A		**10. SPONSORING / MONITORING AGENCY REPORT NUMBER**	
11. SUPPLEMENTARY NOTES The views expressed in this thesis are those of the author and do not reflect the official policy or position of the Department of Defense or the U.S. Government. IRB Protocol Number: N/A.			
12a. DISTRIBUTION / AVAILABILITY STATEMENT Approved for public release; distribution is unlimited		**12b. DISTRIBUTION CODE** A	

13. ABSTRACT (maximum 200 words)

An observational study of tropical cyclone spin-up is performed using dropsondes and satellite imagery from Supertyphoon Jangmi and Hurricane Georges. Additionally, ELDORA data are analyzed in Tropical Storm Jangmi. The dropsonde analysis shows that the peak tangential wind occurs persistently within the boundary layer and suggests that significant supergradient winds are present there. However, as a result of data limitations arising from asymmetries and irregular placement of dropsondes in both time and space, a strongly conclusive statement about the presence of supergradient winds in Tropical Storm Jangmi is not possible. A dense deployment of dropsondes across the RMW is recommended to resolve the pressure gradient with sufficient accuracy to validate that supergradient winds exist at the tropical storm stage. An examination of ELDORA data in Tropical Storm Jangmi indicates that multiple rotating updrafts are present near the eye underneath cold cloud tops of $\leq$ -65°C. Analysis of the infrared satellite imagery from both storms suggests that rotating updrafts are omnipresent before and during rapid intensification. The findings of this study support a new theoretical model positing that spin-up of the maximum winds occurs within the boundary layer and rotating deep convective cells are predominant during tropical cyclone intensification.

14. SUBJECT TERMS Tropical cyclone spin-up, vortical hot towers, Supertyphoon Jangmi, Hurricane Georges, tropical cyclone intensification, rapid intensification, rotating deep convection, tropical cyclone boundary layer.			**15. NUMBER OF PAGES** 187
			16. PRICE CODE
17. SECURITY CLASSIFICATION OF REPORT Unclassified	**18. SECURITY CLASSIFICATION OF THIS PAGE** Unclassified	**19. SECURITY CLASSIFICATION OF ABSTRACT** Unclassified	**20. LIMITATION OF ABSTRACT** UU

NSN 7540-01-280-5500

Standard Form 298 (Rev. 2-89)
Prescribed by ANSI Std. 239-18

THIS PAGE INTENTIONALLY LEFT BLANK

Approved for public release; distribution is unlimited

AN OBSERVATIONAL STUDY OF TROPICAL CYCLONE SPIN-UP IN SUPERTYPHOON JANGMI AND HURRICANE GEORGES

Neil T. Sanger
Lieutenant Colonel, United States Air Force
B.S., Florida State University, 1994
M.H.R., University of Oklahoma, 1997
M.S., Texas A&M University, 1999

Submitted in partial fulfillment of the
requirements for the degree of

DOCTOR OF PHILOSOPHY IN METEOROLOGY

from the

NAVAL POSTGRADUATE SCHOOL
December 2011

Author: _____
Neil T. Sanger

Approved by:

_____	_____
Michael Montgomery Professor of Meteorology Dissertation Supervisor	Russell Elsberry Professor of Meteorology
_____	_____
Patrick Harr Professor of Meteorology	Peter Black Professor of Meteorology
_____	_____
Francis Giraldo Professor of Mathematics	Roger Smith Professor of Meteorology

Approved by: _____
Wendell Nuss, Chair, Department of Meteorology

Approved by: _____
Douglas Moses, Vice Provost for Academic Affairs

THIS PAGE INTENTIONALLY LEFT BLANK

ABSTRACT

An observational study of tropical cyclone spin-up is performed using dropsondes and satellite imagery from Supertyphoon Jangmi and Hurricane Georges. Additionally, ELDORA data are analyzed in Tropical Storm Jangmi. The dropsonde analysis shows that the peak tangential wind occurs persistently within the boundary layer and suggests that significant supergradient winds are present there. However, as a result of data limitations arising from asymmetries and irregular placement of dropsondes in both time and space, a strongly conclusive statement about the presence of supergradient winds in Tropical Storm Jangmi is not possible. A dense deployment of dropsondes across the RMW is recommended to resolve the pressure gradient with sufficient accuracy to validate that supergradient winds exist at the tropical storm stage. An examination of ELDORA data in Tropical Storm Jangmi indicates that multiple rotating updrafts are present near the eye underneath cold cloud tops of $\leq$ -65°C. Analysis of the infrared satellite imagery from both storms suggests that rotating updrafts are omnipresent before and during rapid intensification. The findings of this study support a new theoretical model positing that spin-up of the maximum winds occurs within the boundary layer and rotating deep convective cells are predominant during tropical cyclone intensification.

THIS PAGE INTENTIONALLY LEFT BLANK

TABLE OF CONTENTS

THIS PAGE INTENTIONALLY LEFT BLANK

LIST OF FIGURES

LIST OF TABLES

THIS PAGE LEFT INTENTIONALLY BLANK

ACKNOWLEDGMENTS

I want to thank God for giving me the strength to complete successfully this important work. I could not have done this without His mercy and grace. I want to honor also my beautiful wife, Lily, who supported me through all the difficulties along this hard-fought journey. She took care of everything at home so I could focus completely on my research. She is my best friend and I could not have done this without her love and dedication to this endeavor. A huge thanks goes out to Lily's mom, Maura, for taking care of me with good cooking, especially as my final draft deadline neared. I owe my mom and dad a deep debt of gratitude for preparing me for this battle and being my rock of support during all of the difficulties. I also owe a debt of thanks to my awesome kids, Isabella, Clare, Connor, and Blaise, for understanding my late nights at work and insufferable grumpiness along the way.

I pour out many thanks to my dissertation advisor, Michael Montgomery, for all of his guidance and "milk and cookies" sessions. He taught me so much about tropical meteorology and life. He also gave me the unique opportunity to fly over 150 hours in western Pacific Ocean typhoons during the TCS08 experiment from which much of my data came from for my work on Supertyphoon Jangmi. I have dedicated this work to Michael Montgomery's father, who recently passed away in June 2010. I am also dedicating this research to my Grandpa Wesley Bishop, who passed away on 8 December 2010 at the ripe old age of 86.

I want to thank also all of my esteemed professors, faculty, and staff in the NPS Meteorology Department for their professionalism and dedication to academic excellence. I especially thank Professor Wendell Nuss for all of his advice, encouragement, and support throughout this five-year process. I owe tons of thanks to Robert LeeJoice for assistance with IDL code and being a great office mate. I thank the 53rd Weather Reconnaissance Squadron "Hurricane Hunters" for flying me into the teeth of some fierce typhoons in September 2008. I offer many thanks to Pete Black and his wonderful wife, Ada, for the wonderful meals and conversations. I owe tons of thanks to Bob Creasey for help on myriad computer issues. A big thanks to Pat Harr and Russ

Elsberry for giving me a chance to fly on multiple TCS08 missions and teaching me so much about tropical meteorology.

I want to thank also the Montgomery group for help and support in my studies. Thanks to Michael Riemer for assistance with IDL code. A huge thanks to Michael Bell for endless help with dropsonde and ELDORA data and computer code. Thanks to Saurabh Barve for all of the help with computers and presentations. A big thanks to my committee members: Pat Harr, Russ Elsberry, Frank Giraldo, Pete Black, and Roger Smith for all of their comments and suggestions to make my dissertation an outstanding product. Thanks to my colleagues, Bob Stenger, Mark Allen, Lou Lussier, and Beth Sanabia for all of their support and help in classes and preparing for the preliminary exams.

I want to send my thanks to John Knaff for his assistance with obtaining the high-resolution satellite data that was used in Hurricane Georges, among many other things.

I. INTRODUCTION

A. HISTORICAL OVERVIEW

Category 5 and supertyphoon class tropical cyclones are one of the most extraordinary natural marvels. There is no better way to gain a thorough appreciation of these astonishing phenomena than to be inside the eye of a violent tropical cyclone. The first scientist to observe and describe the inside of an intense hurricane was Robert Simpson, who co-developed the Saffir-Simpson scale of hurricane intensity with Herbert Saffir. While flying in the eye of Typhoon Marge (1951) on a RB-29 aircraft of the 54th Strategic Weather Reconnaissance Squadron, Simpson (1952) provided this detailed account:

> Here was one of Nature's most spectacular displays. 'Marge's' eye was a vast coliseum of clouds, 40 miles in diameter, whose walls rose like galleries in a great opera house to a height of approximately 35,000 feet where the upper rim of the clouds was smoothly rounded off against a background of deep blue sky.

Over five decades later, Emanuel (2005) described the inside of the eye:

> No mere photograph can do justice to the sensation of being inside the eye of a hurricane. Imagine a Roman coliseum 20 mi wide and 10 mi high, with a cascade of ice crystals falling along the coliseum's blinding white walls.

A photograph taken inside the eye of Supertyphoon Jangmi at a peak intensity of 905 hPa and 72 m s^{-1} (Figure 1) provides a glimpse into these awe-inspiring tropical tempests. Unfortunately, these natural wonders of the earth have killed more people globally in the past fifty years than any other natural disaster (Emanuel 2005). For example, Hurricane Katrina (2005) was one of the worst natural disasters in American history, with more than 1800 dead, 700 missing, and over $40B in damage (McTaggart-Cowan et al. 2007). In addition, these perilous storms have had a significant impact on certain cultures, the environment, and many other aspects of common life.

Due to the serious consequences of these fierce storms and the lack of significant improvement of intensity forecast skill in recent years, it is important to obtain a more

complete understanding of the tropical cyclone intensification process. To acquire this increased knowledge, aircraft reconnaissance missions are flown in tropical cyclones with an array of sophisticated instruments onboard to collect large amounts of data for analysis.

Figure 1. Photograph taken by author inside the eye of Supertyphoon Jangmi at maximum intensity (905 hPa/ 72 m s^{-1}) on 27 September 2008 at 0801 UTC from a WC-130J "Hurricane Hunter."

Currently, these critical reconnaissance missions are flown primarily by the United States Air Force Reserve (USAFR) "Hurricane Hunters" of the 53rd Weather Reconnaissance Squadron stationed at Keesler Air Force Base in Biloxi, Mississippi, and the National Oceanic and Atmospheric Administration (NOAA) Aircraft Operations Center (AOC) located at MacDill Air Force Base in Tampa/St.Petersburg, Florida. The Hurricane Hunters use the Lockheed-Martin WC-130J aircraft, while the NOAA/AOC uses the Lockheed-Martin WP-3D and NOAA Gulfstream IV aircraft. These aircraft have state-of-the-art technology onboard to collect a wide range of high-resolution data. During a major field experiment on tropical cyclone formation and intensification in the

Atlantic Ocean in the summer of 2010, a pilotless Global Hawk aircraft was flown at high altitudes in several tropical cyclones. Thus, significant strides have been made in data collection in tropical cyclones since the first "Hurricane Hunter" mission in 1943. However, the one thing that has not changed is the bravery and professionalism of the aircrews that voluntarily fly into these intense storms. It is important to remember that without these courageous men and women, there would be no in situ data available to help improve our understanding of tropical cyclones.

B. CHALLENGES OF TROPICAL CYCLONE INTENSIFICATION FORECASTING

Despite a rapid increase in the amount of data collected in tropical cyclones, the problem of intensification forecasting poses formidable challenges. Currently, the forecasting of tropical cyclone intensification for storms similar to Hurricane Georges (September 1998) and Supertyphoon Jangmi (September 2008) remains a perplexing problem to forecasters at the National Hurricane Center (NHC) in Miami, Florida, and the Joint Typhoon Warning Center (JTWC) in Honolulu, Hawaii. While a 45% (3% y^{-1}) decrease in the 48-h track forecast error of tropical cyclones has been achieved between 1990 and 2005, only a modest decline of around 17% (1.1% y^{-1})yr^{-1}) in the 48-h intensity forecast errors has been attained over the same time period (Rogers et al. 2006).

Hurricane Georges provides a premier example of the hurricane intensity forecasting problem. The first five official predictions after Georges became a tropical storm at 1200 UTC 16 September had an average error of 9 m s^{-1} in the 12-h to 48-h intensity forecast (Guiney 1999). In addition, the Statistical Hurricane Intensity Prediction Scheme model intensity errors were comparable to the official forecast errors. However, the Geophysical Fluid Dynamics Laboratory model performed much worse with an average error of 15 m s^{-1} in the 12-h to 48-h intensity forecasts, and an average error of 28 m s^{-1} in the 72-h intensity forecasts. All of these large intensity errors occurred during the rapid intensification stage.

Supertyphoon Jangmi is another excellent example of a rapidly intensifying tropical cyclone that had large intensity forecast errors. The JTWC had intensity errors

of just 2.5 m s^{-1}– 5.0 m s^{-1} during the tropical storm and weak typhoon stages of Jangmi. After the weak typhoon stage, the intensity errors of JTWC increased significantly. For instance, the 72-h forecast at 0600 UTC 24 September had predicted an intensity of 49 m s^{-1}, which was well below the observed intensity of 72 m s^{-1}. Consequently, the 72-h JTWC forecast had an error spanning three categories of the Saffir-Simpson scale (Category 2 to Category 5). The 48-h forecast at 0600 UTC 25 September had a large error of 18 m s^{-1}. The 24-h forecast issued at 0600 UTC 26 September still had an error of 18 m s^{-1}. Even the 12-h forecast issued at 1200 UTC 26 September under-forecast the intensity by 15 m s^{-1}. The 1200 UTC 26 September JTWC forecast discussion just 12 h prior to Jangmi attaining supertyphoon status included the following statements:

> The initial intensity estimate of 95 knots is based on subjective weighting of satellite intensity estimates from PGTW, KNES, and RJTD ranging from 90 to 105 knots. The initial intensity is at the low end of this spectrum due to the slight weakening reflected in intermediate Dvorak estimates suggesting a system as weak as 80 knots… Outflow into the TUTT to the east, in addition to overall strong radial outflow, continues to facilitate strengthening…the forecast philosophy has not changed significantly since the previous issuance of the prognostic reasoning message.

The official JTWC intensity forecast that corresponded to the 26 September 1200 UTC discussion is listed below:

```
TYPHOON 19W (JANGMI) WARNING #12
261200Z POSIT: NEAR 17.7N 127.9E
MOVING 310 DEGREES TRUE AT 12 KNOTS
MAXIMUM SIGNIFICANT WAVE HEIGHT: 28 FEET
26/12Z, WINDS 095 KTS, GUSTS TO 115 KTS
27/00Z, WINDS 105 KTS, GUSTS TO 130 KTS
27/12Z, WINDS 115 KTS, GUSTS TO 140 KTS
28/00Z, WINDS 120 KTS, GUSTS TO 145 KTS
28/12Z, WINDS 105 KTS, GUSTS TO 130 KTS
29/12Z, WINDS 090 KTS, GUSTS TO 110 KTS
30/12Z, WINDS 040 KTS, GUSTS TO 050 KTS
01/12Z, WINDS 020 KTS, GUSTS TO 030 KTS
```

The next intensity forecast issued by JTWC at 1800 UTC 26 September was much more accurate with an error of only 5 m s^{-1}. However, a 12-h intensity forecast is expected to have small errors of < 5 m s^{-1}. The large intensity 24 h – 72 h forecast errors could have led to a lack of preparation and loss of human life if Jangmi had been closer to land.

Two previous studies have documented the importance of improving intensity forecasting skill for rapidly intensifying storms. Holliday and Thompson (1979) found 75% of the 305 western North Pacific typhoons between 1956 and 1976 with pressures less than 920 hPa had experienced rapid intensification. They defined rapid intensification as a pressure fall of 42 hPa in a 24-h period. Similarly, Wang and Zhou (2007) discovered that 90% of all supertyphoons between 1965 and 2004 experienced at least one phase of rapid intensification, which they defined as a 15 m s^{-1} increase in the surface wind speeds in 24 h. This definition is the same as Kaplan and DeMaria (2003). Since these studies indicate that most intense tropical cyclones undergo at least one rapid intensification period, it is extremely important to improve the forecasting of rapid intensity changes. The in situ and satellite data from Hurricane Georges and Supertyphoon Jangmi will provide new insights needed to improve the understanding of rapid intensification.

According to Rogers et al. (2006), the slow improvement of intensity forecast skill may be related to three main factors:

> 1) deficiencies in systematically collecting inner-core data to provide real-time estimates of TC intensity and structure to the forecasters at NHC and for assimilation into the numerical models at EMC and elsewhere; 2) limitations in the numerical models themselves, such as insufficient computing resources to run operational forecast models at high horizontal and vertical resolution, inadequate specification of the TC vortex in the initial conditions of the numerical models, and deficient representation of physical processes; and 3) gaps in our understanding of the physics of TCs and their interaction with the environment.

An additional challenge of intensity forecasting is revealed in a recent study by Nguyen et al. (2008; hereafter NSM08). These authors showed in their idealized three-dimensional, nonhydrostatic numerical study of the benchmark intensification problem on an *f*-plane that the inner-core asymmetries in a tropical cyclone are dominated by

rotating deep convection[1] that possesses a significant random component and may be intrinsically unpredictable. NSM08 argue that this lack of predictability is due to the convective nature of the inner-core region, which limits the intensity prediction skill. Consequently, there may be a bound to the predictability of tropical cyclone intensification.

Now that it has been established that there is a significant deficiency in tropical cyclone intensity forecasting, it is important to discuss its ramifications and the path to gaining more knowledge on this important topic. Thus, the next section will cover the motivation behind this research followed by a brief discussion of key definitions, hypotheses, datasets, and the link between this research and other field experiments.

C. SCIENTIFIC EXPLORATION OF SPIN-UP

1. Motivation

None of the three primary spin-up (this term is used interchangeably with intensification throughout the thesis) theories that will be described later in Chapter II has been tested thoroughly with observations to determine which is the most appropriate fundamental description of the intensification process in the real atmosphere. Without a basic understanding of the dominant spin-up process operating in the real atmosphere, it will be difficult to improve significantly intensity forecasting of tropical cyclones. Since so many lives and assets depend on accurate intensity forecasts, the focus of this research is limited to the spin-up phase of tropical cyclones that have already attained tropical storm status (surface winds between 17 m s^{-1} and 33 m s^{-1}) via tropical cyclogenesis.

[1]The term "rotating deep convection" is used in lieu of vortical hot towers (VHTs), which were first described in Hendricks et al. (2004) and later studied in Montgomery et al. (2006a) and NSM08, among others. To avoid any potential controversy that surrounds the definition of VHTs, the term 'rotating deep convection' will be used throughout the rest of this thesis. In addition, using the term VHT has led some to the impression that only extremely intense convection has strong rotation. However, a recent study by Wissmeier and Smith (2011) suggests that all rotating deep convection should be considered in total, since they showed that moderate convection can have a greater impact on stretching of low-level relative vorticity than the most intense convection. Thus, a broad definition is required for studying the aggregate impact of these convective elements on tropical cyclone spin-up.

2. Inner Core and Outer Core Definitions

To ensure a proper assessment of the two hypotheses that will be introduced below in Section 3, it is first necessary to define the terms "inner core" and "outer core" that will be used frequently in this thesis. The definition of the inner-core region of the tropical cyclone is adopted from Wang and Wu (2004):

> The inner core structure represents the structure within a radius of twice the RMW, including the deep eyewall clouds, the eye of the storm, and convective asymmetries in the eyewall, such as convectively coupled vortex Rossby waves and spiral rainbands.

The outer core of the tropical cyclone is hereafter defined as the region spanning approximately twice the radius of maximum winds (RMW) to the radius of gales (surface winds of ~ 17 m s^{-1}).

3. Hypotheses to be Tested in This Thesis

The primary objective of this research is to conduct an observational study of tropical cyclone spin-up to aid in determining the most appropriate fundamental theory for this important process. Specifically, the following two hypotheses are proposed:

(H1) Spin-up of the inner-core vortex of Supertyphoon Jangmi and Hurricane Georges occurs within the boundary layer where significant supergradient winds are present, and,

(H2) Rotating deep convective cells occur frequently during the spin-up of Supertyphoon Jangmi and Hurricane Georges, which confirms recent theoretical studies that rotating deep convective cells are predominant during intensification.

H1 will be tested using both composite and individual dropsonde radial profiles of tangential and radial wind speed in the eyewall region together with an assessment of gradient wind balance at six altitudes in the inner core. The following metrics will be used to test H1: (i) composite vertical profiles of radial and tangential wind speed will be constructed to document that in the mean sense, the peak tangential wind speed occurs within the inner-core boundary layer; (ii) examination of individual vertical profiles of radial and tangential wind speed within the inner core will document that the majority of

these profiles have maximum tangential wind speeds within the boundary layer; and iii) analysis of the deviations from gradient wind balance will document that significant supergradient tangential winds exist within the boundary layer near and just within the RMW of these two storms.

H2 will be tested utilizing the Naval Research Laboratory (NRL) P-3 Electra Doppler Radar (ELDORA) data from the tropical storm stage of Jangmi and high-resolution satellite imagery (in both space and time) during the spin-up of both Jangmi and Georges. The analyses of these observations will document: (i) one or more instances of rotating deep convection observed by ELDORA data occur underneath areas of overshooting tops and/or sufficiently cold cloud-top temperatures ($\leq$ -65°C); and (ii) similar convective activity is witnessed in infrared satellite imagery throughout the spin-up phase.

To gain a better appreciation of the importance of the current work presented, it is necessary to discuss the relevance of this study on the inner-core spin-up of tropical cyclones. Thus, the next section will discuss the critical link between this research and recent hurricane field campaigns.

4. Relation of Current Research to Recent Hurricane Field Experiments

a. TCS08/T-PARC

The observations of Jangmi were collected during two field experiments in August–September 2008: The Observing systems Research and Predictability Experiment (THORPEX) Pacific Asian Regional Campaign (T-PARC); and the Tropical Cyclone Structure 2008 (TCS08). The multiple reconnaissance missions flown in Supertyphoon Jangmi at various stages of its spin-up and mature phase offer a unique opportunity to obtain a better understanding of the tropical cyclone spin-up process.

The combined TCS08/T-PARC was a multi-national field experiment that explored the entire life cycle of tropical cyclones in the western North Pacific(Parsons et al. 2008; Elsberry and Harr 2008; Elsberry et al. 2008). The primary motivation behind this western North Pacific field experiment was to better understand and forecast tropical cyclones during formation, intensification and structure change, and recurvature and

extratropical transition (Elsberry and Harr 2008). The primary aircraft used for penetrations of the inner core of developing and mature storms was the USAFR 53rd Weather Reconnaissance Squadron WC-130J aircraft. The NRL P-3 with its ELDORA was available also, but could not penetrate the inner core of a typhoon (Elsberry and Harr 2008). In addition, the Taiwanese DOTSTAR and German Aerospace Center (Deutsches Zentrum für Luft- und Raumfahrt; DLR) Falcon aircraft flew at high altitudes in the outer environment of tropical cyclones. As additional justification for such far-reaching international participation, it is expected that observations and results gathered during this program will be applicable to other ocean basins that contain tropical cyclones. Elsberry and Harr (2008) provide a more detailed description of the TCS08 field experiment and the various scientific hypotheses to be tested.

According to Parsons et al. (2008, section 1, paragraph 1), the primary aim of TCS08/T-PARC was:

> To increase understanding of the mechanisms that will lead to improved predictive skill of high impact weather events.

The other primary science objectives of TCS08/T-PARC are described in Parsons et al. (2008, section 1, paragraph 1).

The main objectives of this research and the associated hypotheses (H1 and H2) address the following objective of this major field experiment:

> Improved understanding of the dynamics and factors that limit the predictability of downstream high-impact weather events due to typhoons, extratropical transition events, and other intense cyclogenesis events originating in the North Pacific and adjacent land areas.

This study will address this objective by examining the dynamics of spin-up within the inner core of rapidly intensifying Supertyphoon Jangmi during three distinct stages of its evolution: investigating small-scale rotating deep convective structures during Jangmi's transition from a tropical storm to a typhoon; and exploring the dynamics of steady-state maintenance in Hurricane Georges.

b. IFEX

The data collected and analyzed in both Georges and Jangmi addresses two of the three goals of the National Oceanic and Atmospheric Administration (NOAA) Intensity Forecasting Experiment (IFEX), which according to Rogers et al. (2006) are:

> (1) Collect data that covers the tropical cyclone life cycle in multiple environments; (2) create and improve measurement technologies that yield better real-time monitoring of tropical cyclone intensity, structure, and environment; and (3) enhance our knowledge of the physical mechanisms critical to intensity change for all stages of a tropical cyclone's life cycle.

This study will address goals (1) and (3) by conducting an investigation similar to the one used for addressing the two objectives of TCS08/T-PARC. This study will address also goal (2) by documenting a relatively new dropsonde data collection method used in Supertyphoon Jangmi.

5. Data Collection Missions in Hurricane Georges and Supertyphoon Jangmi

A high degree of success was achieved in collecting critical data in Hurricane Georges and during the evolution of Jangmi from a tropical storm to a supertyphoon. Multiple aircraft reconnaissance missions obtained observations from dropsondes launched in the inner core. Moreover, critical airborne ELDORA data was obtained during the Tropical Storm stage of Jangmi as it was rapidly nearing typhoon strength. In addition to these in situ observations, high-resolution (in space and time) satellite data were available for analysis during the entire spin-up of both storms. Analyses of these data in conjunction with previous modeling simulations will contribute to understanding of some common dynamical features of the tropical cyclone spin-up process.

6. Outline of This Study

Before presenting the observational data, analysis, and physical interpretation of this research, a succinct review of the boundary layer and its role in the three prevailing tropical cyclone spin-up theories is portrayed first in Chapter II. This material serves to establish basic concepts and guide the interpretation of the observations. Chapter III includes a description of the data collected and the methodology used in this study. In

Chapter IV, an axisymmetric perspective of the inner-core spin-up process is shown for the three-day evolution of Supertyphoon Jangmi and for the one-day evolution of Hurricane Georges. An axisymmetric approach is used first to perform an analysis of gradient wind balance in the inner-core region of these two storms. Here, both individual and composite kinematic profiles within and just above the boundary layer are presented. In addition, a comparison of the thermodynamic and dynamic boundary layer depths is conducted for the inner cores of Jangmi and Georges. The asymmetric aspects of the tropical cyclone spin-up process are considered in Chapter V. For both Jangmi and Georges, high-resolution satellite imagery is analyzed to document the deep convective cells during the spin-up process. Mesoscale ELDORA radar observations are displayed during the spin-up of Tropical Storm Jangmi to document a representative rotating deep convective burst for comparison with coincident satellite imagery. Finally, Chapter VI includes a brief discussion, conclusions, and recommendations for future work.

THIS PAGE LEFT INTENTIONALLY BLANK

II. TROPICAL CYCLONE SPIN-UP REEXAMINED

Later in this chapter, it will be argued that there is a strong connection between the boundary layer and the spin-up of the inner-core tangential winds. To prepare for this discussion, it is first necessary to review the physical role of the hurricane boundary layer and how it has been defined and modeled in previous research.

A. IMPORTANCE OF THE BOUNDARY LAYER

It has been long known that the boundary layer of a tropical cyclone is an important region of the storm. At the bottom of the boundary layer, the storm gains energy from the underlying ocean surface primarily from moisture fluxes, and loses absolute angular momentum to the ocean because of frictional stress. The absolute angular momentum per unit mass of air is defined by the moment of absolute momentum about the spin axis of the tropical cyclone. Since the objective is to study the rate of change of the primary circulation of the vortex, the component of angular momentum that is rotating around the storm's axis is usually the focus of interest. This vertical component (M) is given by the sum of the angular momentum of the storm's tangential flow and the angular momentum due to the rotation of the earth: $M = rv + 1 / 2\, fr^2$, where r is the radius from the storm center, v is the tangential wind speed, and f is the Coriolis parameter. The structure and evolution of M will figure prominently in the upcoming discussion of tropical cyclone spin-up theories below.

The boundary layer was featured prominently in several early studies of tropical cyclone spin-up (Ooyama 1969; Anthes and Chang 1978; Garstang 1979). Over the past decade and a half, there has been a resurgence of studies on the hurricane boundary layer in regards to spin-up (Emanuel 1995, 1997; Zhang et al. 2001; Smith et al. 2009; Zhang et al. 2009; Smith and Montgomery 2010).

B. DEFINITIONS OF THE BOUNDARY LAYER

A particularly controversial issue has been the definition of the tropical cyclone boundary layer, especially within the inner-core region of the cyclone. Since dissimilar definitions can lead to the use of differing parameterizations of the boundary layer, it is important to select the most appropriate definition for studying spin-up in the inner core of tropical cyclones. Smith and Thomsen (2009) have found that the use of various parameterization schemes in the MM5 model can produce variations in the gestation time, intensification rate, and boundary-layer structures of the tropical cyclone vortex. The adoption of a single definition of the inner-core tropical cyclone boundary layer will help standardize its parameterization in the inner core. To aid this determination, the thermodynamical and dynamical boundary-layer definitions are reviewed briefly below along with boundary-layer observations from a recent tropical cyclone field experiment.

1. Thermodynamic Definition

A popular definition of the tropical cyclone boundary layer is the thermodynamical well-mixed layer. Moss and Merceret (1976) defined the boundary layer as the vertical layer next to the sea surface in which constant small-scale, surface-generated turbulence exists that is not associated with "towering cumuli." Their definition is nearly identical to that of Deardorf (1972) and Garstang (1979). Anthes and Chang (1978) defined the boundary layer as the height at which the potential temperature of the air exceeds that at the ocean surface by 0.5 K.

The thermodynamical definitions reviewed above are appropriate where air is generally sinking into the boundary layer in the environmental region of the tropical cyclone. However, these definitions of the boundary layer are not appropriate in regions where air is rising out of the boundary layer in an unstable atmosphere. Additionally, they do not account explicitly for dynamical processes such as gradient wind imbalance due to surface friction. Typically, the inner core of a tropical cyclone contains a shallow layer of significant radial inflow ($\geq$ 20% of surface value) that is usually 500 m to 1 km in vertical extent. The prevalence of this stout radial inflow suggests that departures from gradient wind balance may be significant and need to be accounted for properly. Since

the thermodynamical definition does not consider dynamical effects, it is believed to be an inappropriate choice for understanding the spin-up processes in the inner core of a tropical cyclone.

2. Dynamical Definition

Smith et al. (2009; hereafter SMN09) adopted a dynamical definition of the inner-core boundary layer in their three-dimensional model simulations of tropical cyclone spin-up. They defined the boundary layer as a shallow layer of strong inflow near the ocean surface that is generally 500 m to 1 km deep. They noted also that this strong inflow is generated primarily by the frictional disruption of gradient wind balance near the surface (e.g., Figures 5 and 6 of Bui et al. 2009).

3. Challenges in Defining the Boundary Layer in the Inner Core

SMN09 noted the similarity between fluid dynamical separation and the eruption of the boundary layer into the vortex interior near the eyewall region of the tropical cyclone. They compared this flow eruption to that which occurs on an airfoil or other smooth obstacle immersed in a flow. Separation occurs when there is an adverse pressure gradient force acting to decelerate the fluid flowing along the surface of the airfoil or obstacle. Kundu (1990; hereafter K90) and Batchelor (1967) provide a lucid explanation of the special flow pattern of separation in the region of a solid boundary such as an airfoil. K90 provides an illustration of separation in Figure 2 (adapted from his Figure 6.2).

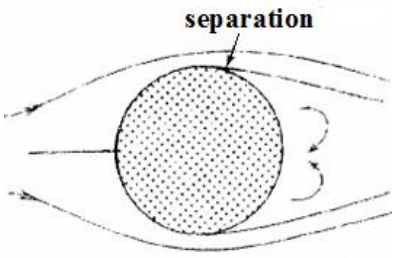

Figure 2. Example of flow separation as air streams from left to right above and below a solid sphere. Arrow at top of sphere shows location where separation first occurs. Arrows downstream of separation point indicate turbulent eddies. Adapted from K90, Figure 6.2.

For the case of the tropical cyclone inner core, the governing radial force that is responsible for accelerating and decelerating the boundary layer flow is the so-called "agradient force" (*AF*), which is defined by the difference between the local radial pressure gradient force and the sum of the centrifugal and Coriolis forces in the radial direction: $AF = - (1/\rho) (\partial p/\partial r) + (v^2/r + fv)$, where p is the air pressure, ρ is the density of air, f is the Coriolis parameter, r is the radius from the storm center, v is the tangential wind velocity, v^2/r is the centrifugal force, and fv is the Coriolis force. When $AF = 0$, the tangential flow is in gradient wind balance. If $AF < 0$, the tangential flow is subgradient. When $AF > 0$, the tangential flow is supergradient.

Let us now consider in a little more detail how the agradient force influences the boundary-layer dynamics of a tropical cyclone vortex. Near the ocean surface at some distance beyond the radius of maximum gradient wind, the tangential flow in the boundary layer is less than the bulk flow above the boundary layer on account of friction (i.e., the flow is subgradient). In that radial region, the centrifugal and Coriolis forces are decreased relative to those forces in the bulk flow above the boundary layer. The corresponding imbalance of the radial pressure gradient force and the centrifugal and Coriolis forces results in a radially inward-directed force ($AF < 0$). This inward-directed force causes acceleration toward the center of circulation and a frictionally-induced inflow results. If the inward acceleration of air parcels spiraling in toward the center is large enough, M may decrease more slowly than the radius, enabling the flow to become supergradient. If this occurs, the flow decelerates rapidly, the *AF* becomes positive, and the effective radial force reverses sign from negative (inward) to positive (outward). In this region of decelerated boundary-layer flow, the bulk of the flow will turn upward and erupt out of the boundary layer.

The concept of boundary-layer air erupting into the eyewall is similar to the discussion by Stull (1988) in regards to defining the boundary layer in the inter-tropical convergence zone (ITCZ), in which air is rising into the vast convective cloud complexes of this region of the atmosphere (see his Figure 1.6). Stull (1988, Chap. 1) succinctly describes the challenge of determining a boundary layer in the ITCZ region:

> In low pressure regions, the upward motions carry boundary-layer air away from the ground to large altitudes throughout the troposphere. It is difficult to define a boundary-layer top for these situations.

Supporting evidence for this viewpoint in tropical cyclones was expressed long ago by Shapiro (1983), who explicitly noted that near and within the eyewall the boundary layer becomes "ill defined" as the air is drawn upwards into the strong convection. Due to the inability of the above definitions to describe the complex boundary-layer separation process, a practical definition is required for this dissertation. To determine an appropriate definition, recent observational studies from an important field experiment are examined.

4. Recent Observations

A large amount of data from the tropical cyclone boundary layer has been analyzed over the last decade following the implementation of the National Center for Atmospheric Research (NCAR) Global Positioning System (GPS) dropsonde in specialized boundary-layer experiments. One of these experiments was the Coupled Boundary Layer Air-Sea Transfer (CBLAST) field campaign. The primary goal of this experiment was to observe directly turbulent fluxes and other turbulent properties of the high wind region (20 – 30 m s^{-1}) in between spiral bands (Zhang et al. 2009; hereafter Z09). Thorough summaries of the CBLAST experiment are found in Black (2004), Black et al. (2007), Drennan et al. (2007), and French et al. (2007).

Z09 (their Figure 10) highlighted the importance of the radial inflow in their conceptual model of the hurricane boundary layer by computing mean vertical profiles of virtual potential temperature, and radial and tangential wind components from nine GPS dropsondes. It is noteworthy that Z09 found that a marked delineation exists between the thermodynamical and dynamic boundary layers. That is, the turbulent momentum fluxes tend toward zero at an altitude between the maximum tangential wind velocity at ~ 700 m and the top of the radial inflow at ~ 950 m instead of at the top of the mixed layer at ~ 400 m. These results led Z09 to note:

> Our results emphasize the importance of understanding the turbulent structure within the inflow layer, crucial to the parameterization of the hurricane boundary layer.

These important findings from Z09 strongly support the use of a dynamical definition rather than a thermodynamic definition of the inner-core tropical cyclone boundary layer.

5. Boundary Layer Definitions Used in this Thesis

Based on the considerations discussed above, a dynamical definition of the inner-core boundary layer will be used for diagnosis of tropical cyclone spin-up. Specifically, the definition of the inner-core tropical cyclone boundary layer is adapted from SMN09 as the *layer of significant gradient wind imbalance ($\geq$ 10%), typically at least 500 m to 1 km in depth, which arises primarily from frictional effects.* The dynamical boundary layer can be approximated by the layer of significant radial inflow (typically 500 m - 1 km in depth) as was done in SMN09. A schematic of the expected profiles in the inner-core region of the radial wind (u), agradient force (AF), virtual potential temperature (θ_v), and equivalent potential temperature (θ_e) is shown in Figure 3. Observations to be presented in Chapter IV will confirm that these schematic profiles correctly demonstrate that the dynamical boundary layer so defined is significantly elevated relative to the thermodynamic boundary layer.

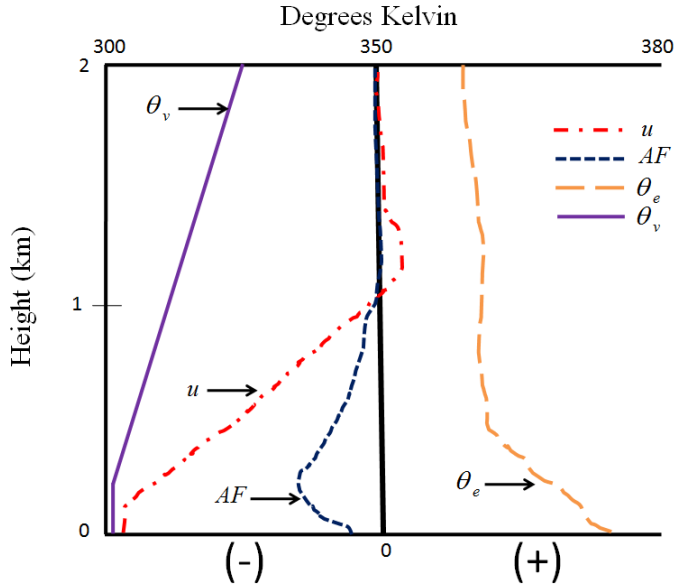

Figure 3. Conceptual profiles of virtual potential temperature (θ_v; solid purple curve); radial wind (u; dashed red curve), agradient force (AF; dotted blue curve), and equivalent potential temperature (θ_e; long-dashed orange curve) in the inner-core region of a tropical cyclone.

C. TROPICAL CYCLONE SPIN-UP THEORIES REVIEWED

To establish a foundation for understanding the spin-up process as observed in the real atmosphere to be discussed in Chapters IV and V, three primary spin-up theories will be reviewed.

1. Conventional Spin-Up Theory

The conventional view of tropical cyclone spin-up is based on the Ooyama (1969) axisymmetric, quasi-balanced vortex model with three layers of incompressible fluid, with the lowest layer being the planetary boundary layer and the other two representing the lower and upper troposphere (Figure 4). The conventional theory has been discussed in somewhat more general contexts by Ooyama (1982) and Willoughby (1988, 1995). The conventional theory of tropical cyclone spin-up emphasizes a deep layer of convectively-induced convergence of M above the boundary layer, where the flow above is assumed to be essentially frictionless so that M is materially conserved. Owing to conservation of M, fluid rings of air converging inward above the boundary layer lead to

an increased tangential velocity. Whereas friction in the boundary layer depletes *M* that is brought in from outer radii, the frictional convergence supplies "fuel" needed to sustain the deep convection in the form of water vapor acquired from the underlying ocean through evaporation of seawater.

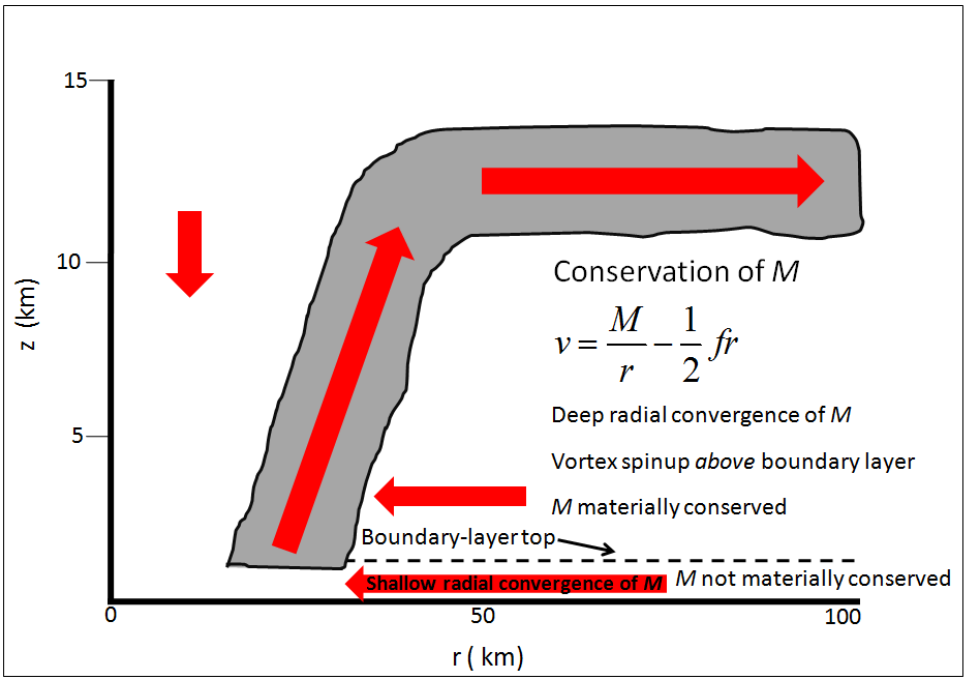

Figure 4. Schematic diagram of the conventional view of tropical cyclone spin-up in the radius-height (R-Z) plane. Red arrows indicate the flow of air parcels above and within the frictional boundary layer, the absolute angular momentum (*M*) is materially conserved. From the formula $v = M/r - 1/2\ fr$, an inward moving air parcel that conserves *M* will increase its tangential velocity. *M* is not materially conserved in the boundary layer and is progressively lost to the underlying sea. However, the frictionally-induced inflow acts to bring in water vapor that is evaporated from the underlying ocean outside the eyewall. The frictional inflow therefore supplies "fuel" (water vapor) to sustain the deep moist convection in the eyewall clouds.

2. WISHE Spin-Up Theory

The second spin-up theory that has come into vogue emphasizes thermodynamic processes, and focuses in particular on the wind-speed dependence of the surface moist entropy fluxes (Emanuel 1989, 1995, 1997; Emanuel et al. 1994). This thermodynamic model posits a Wind Induced Surface Heat Exchange (WISHE) instability mechanism.

The WISHE idea was formulated by Yano and Emanuel (1991) and later articulated in greater detail by Emanuel et al. (1994, section 5a). The WISHE theory purports that tropical cyclone spin-up is due to a positive feedback between the near-surface wind speed and the evaporation of water from the underlying ocean, which is a function of wind speed (Emanuel 1989, 1995, 1997). A schematic of the WISHE spin-up mechanism is shown in Figure 5.

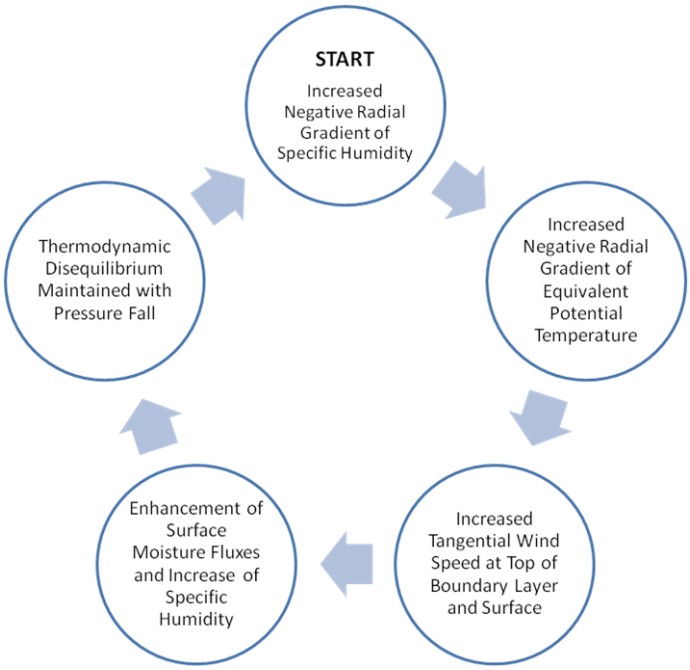

Figure 5. Schematic of the (Emanuel 1989, 1995, 1997; Emanuel et al. 1994) evaporation-wind intensification mechanism known as WISHE. The closed circle at top center of the figure is the beginning of the WISHE feedback loop for tropical cyclone intensification.

The conventional and WISHE tropical cyclone spin-up theories coexisted for approximately 22 years. The primary difference between the two theories is that WISHE emphasizes the wind-speed dependent fluxes and the feedback between θ_e and the swirling wind field near the ocean surface, while the conventional view focuses on convectively-induced convergence of M above the boundary layer and frictionally-induced moisture convergence in the boundary layer to feed the convection in the eyewall. Gray and Craig (1998) and Craig and Gray (1996) presented numerical model simulations in support of the hypothesis that tropical cyclone spin-up is a result of the

postulated WISHE feedback mechanism. Subsequently, the WISHE paradigm has overshadowed the conventional theory of tropical cyclone spin-up, and has attained extensive acceptance in tropical weather discussions, dynamic meteorology textbooks, and current journal articles (Lighthill 1998; Smith 2003; Holton 2004; Molinari et al. 2004; Montgomery et al. 2006b; Ahrens 2007; Rauber 2008).

3. Rotating Deep Convection

The studies of NSM08, Montgomery et al. (2009; hereafter MNSP09), SMN09, and Bui et al. (2009; hereafter BSMP09) comprise a third paradigm for the tropical cyclone intensification process, that consists of an asymmetric and axisymmetric perspective (Figure 6). The paradigm is based on the recent demonstration that the enhanced moisture fluxes in a tropical depression environment provide sufficient forcing to sustain an asymmetric upscale organization process involving rotating deep convective structures. These rotating cells are hypothesized to be the fundamental elements that collectively drive the spin-up of the system-scale vortex. A low-level vorticity maximum is hypothesized also to exist in the lower troposphere (~ 1 – 2 km altitude) of the inner-core region that is largely a result of vortex tube stretching due to these updrafts. The peak vertical velocities are typically located between an altitude of 5 km and 7 km. The latent heat released within the cores of these rotating clouds is hypothesized to be responsible in the aggregate for the convectively-induced inflow in the lower troposphere. This asymmetric viewpoint is summarized in Figure 6a.

From an axisymmetric perspective (Figure 6b), the convectively-induced inflow is responsible for two spin-up mechanisms. The first mechanism, which leads to spin-up of the outer core, is associated with the radial convergence of M above the boundary layer in conjunction with its material conservation. The second mechanism, which is responsible for spin-up of the inner core, is associated with strong radial convergence of M within the boundary layer. The enhanced frictional convergence eventually leads to the development of strong low-level inflow and supergradient tangential winds within the boundary layer of the inner core. Although M is not materially conserved within the boundary layer, large wind speeds can be achieved if the radial inflow is sufficiently

large to bring air parcels to small radii with minimal loss of *M*. This mechanism is tied ultimately to the dynamics of the boundary layer, where the flow is not in gradient wind balance and deviations therefrom are significant over a substantial radial span.

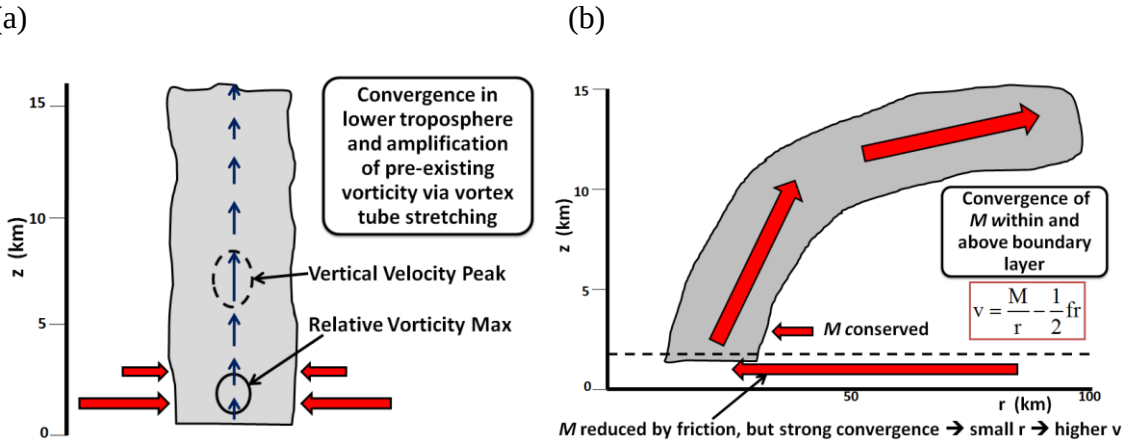

Figure 6. Schematic of the new theory of tropical cyclone spin-up. The schematic portrays the asymmetric and axisymmetric views of spin-up as demonstrated in NSM08, MNSP09, SMN09, and BMSP09. (a) Local (i.e., asymmetric) view of spin-up. The vertical blue arrows represent the upward vertical velocities inside the rotating updraft and indicate the presence of vortex tube stretching. Vertical velocity peak shown with dashed black circle at 5 km – 7 km altitude and relative vorticity max depicted with solid black circle between 1 km and 2 km altitude. The solid red arrows within the lower troposphere show convergence in lower troposphere. (b) System-scale (i.e., azimuthally-averaged) view of spin-up. Solid red arrows depict convectively-induced convergence within and above the boundary layer. The enhanced convergence in the boundary layer progressively leads to the development of strong low-level inflow and supergradient tangential winds in the inner-core region of the vortex. The schematic of the new spin-up theory in Figure 6b is similar to the conventional theory above the boundary layer, with convergence of *M* occurring above the boundary layer; however, there is a distinct difference in the boundary layer region, where the new theory hypothesizes spin-up is occurring due to strong convergence of *M* driven by gradient wind imbalance and rotating deep convection.

a. Asymmetric Viewpoint in Detail

NSM08, SMN09, and MSNP09 demonstrated that *rotating deep convective clouds observed in their idealized three-dimensional numerical model were the basic coherent structures of the tropical cyclone spin-up process*. They demonstrated also that the spin-up process was intrinsically asymmetric and possessed a stochastic

component. They observed that it is the gradual segregation, merger, and axisymmetrization of rotating deep convective updrafts, and the *low-level convergence* they produce collectively that is fundamental to the tropical cyclone spin-up process. The primary reason for the strong low-level convergence in the boundary layer is the gradient wind imbalance due to friction. However, the aggregate effect of the deep convection enhances the inflow in the axisymmetric sense by increasing the radial pressure gradient at the top of the boundary layer.

During the organizational period in their idealized experiments, a segregation of the vorticity anomalies occurs in which the cyclonic vorticity anomalies move slowly inward, and the anticyclonic vorticity anomalies move slowly outward relative to the cyclonic anomalies, decay in amplitude, and succumb to the vortex axisymmetrization process. The reader is referred to (McWilliams and Flierl 1979; Smith and Ulrich 1990; Montgomery and Enagonio 1998; Schecter and Dubin 1999) for a more detailed discussion of vortex motion, axisymmetrization, and the segregation process in idealized geophysical flows.

NSM08 and SMN09 demonstrated that merger and axisymmetrization of the deep rotating convective cells and the net diabatic heating and associated lower-tropospheric inflow that these structures produce, which results in the strengthening of the primary vortex. This new asymmetric spin-up pathway is consistent with and extends prior studies (e.g., Montgomery and Enagonio 1998; Möller and Montgomery 2000; Enagonio and Montgomery 2001; Heymsfield et al. 2001; Braun 2002; Hendricks et al. 2004; M06a).

To evaluate the new theory of spin-up with the observations from this research, some of the main findings from the NSM08 study are listed. The axisymmetrization, segregation, and merger process described above is illustrated in their idealized, high-resolution (1.67 km) numerical model results (Figure 7; adapted from their Figure 18.). The 850 hPa relative vorticity field is shown at 7 h (Figure 7a), 36 h (Figure 7b), 48 h (Figure 7c), and 78 h (Figure 7d) during the simulated spin-up process. After 7 h, the positive relative vorticity begins to expand horizontally in scale and becomes more intense by 36 h. NSM08 show that this horizontal growth is due primarily

to merger and axisymmetrization with nearby cyclonic vorticity anomalies, and in response also to convergence of like-signed vorticity from the local environment. During this period, vorticity segregation is evident as the cyclonic anomalies move slowly inward, and the anticyclonic anomalies move slowly outwards in relation to the cyclonic vorticity anomalies. A ring of intense cyclonic vorticity forms by 78 h, and the negative relative vorticity has been expelled to the outer fringes of the cyclonic vortex ring. A representative example of the rotating deep convective clouds at the 24 h point of vortex spin-up is shown in Figure 8 (adapted from their Figures 8a, 9a). The relative-vorticity field is highly asymmetric in the sense that the flow varies substantially around the azimuth. Moreover, the three maximum upward vertical velocity cores in Figure 8a are roughly co-located with the three regions of peak cyclonic vorticity in Figure 8b.

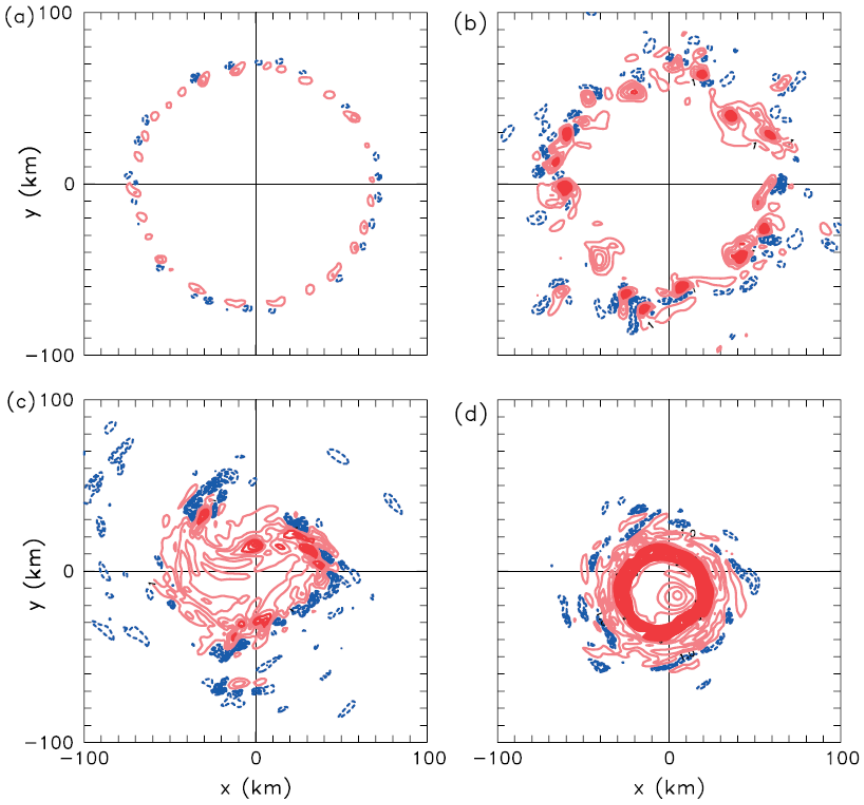

Figure 7. 850 hPa relative vorticity fields for the experiment with 1.67 km horizontal grid spacing by NSM08 (their Figure 18), after (a) 7 h; (b) 18 h; (c) 36 h; (d) 78 h. Positive values are shown by solid red contours, with a contour interval of 10^{-3} s^{-1}. Areas with values greater than 5×10^{-3} s^{-1} are highlighted by dark red contours. The zero contour is not plotted. Negative values are shown by dashed blue contours at intervals of 0.5×10^{-3} s^{-1} in (a) – (b) and 0.2×10^{-3} s^{-1} in (c) – (d).

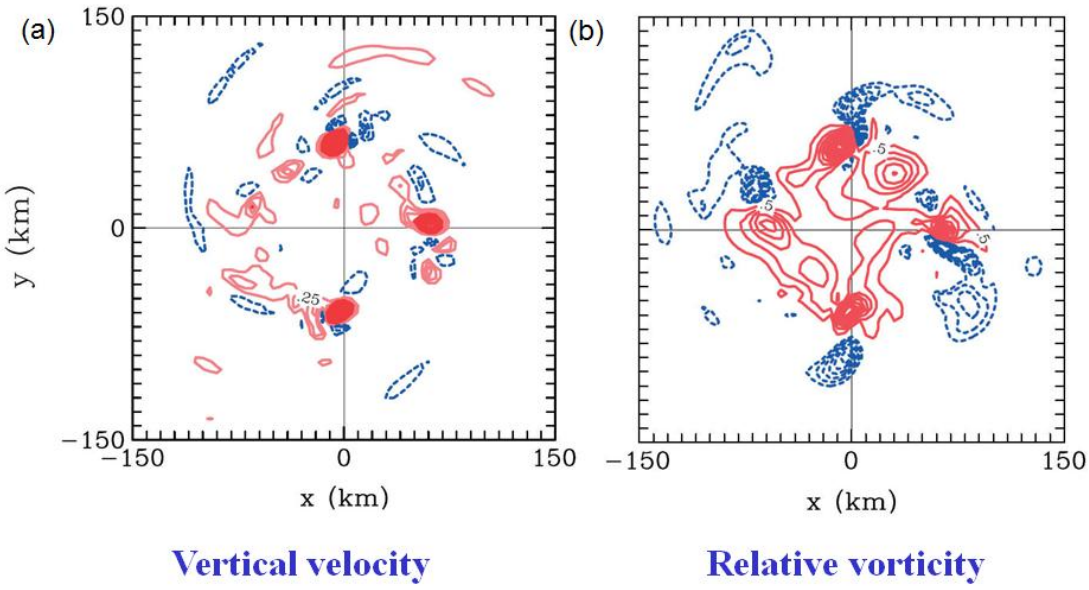

Figure 8. (a) 850 hPa vertical velocity field at 24 h for control experiment and (b) 850 hPa relative vorticity field for control experiment at 24 h. Adapted from NSM08's Figure 8a and Figure 9a.

b. Axisymmetric Viewpoint in Detail

An axisymmetric or "mean field" view of the spin up process is first adopted by azimuthally–averaging all of the three-dimensional flow fields. The frictionally-induced agradient force (defined previously in Section B3) eventually leads to the development of a strong low-level radial inflow within the boundary layer. The speed of this inflow is generally a function of boundary-layer depth and the gradient wind profile at larger radii (Smith et al. 2008; hereafter SMV08).The slab-model boundary layer computations of Smith and Vogl (2008) and SMV08 indicate that the strong low-level radial inflow helps develop the supergradient winds by increasing the radial convergence. SMN09 noted in their numerical simulations that significant supergradient winds can develop in the inner-core boundary layer throughout the intensification process. Another ingredient of this spin-up model is the assumption of weak, but nonzero convergence, above the boundary layer. This convergence is necessary to increase the tangential winds above the boundary layer, which will then serve to increase the radial pressure gradient at the top of the boundary layer and thereby enhance the inflow within the boundary layer. Considering the absolute angular momentum equation ($v = M/r - ½$

fr), although M is not conserved within the boundary layer, if the convergence is strong enough and parcels are pushed to smaller radii, the tangential wind speeds will increase.

As discussed above, the radial inflow in the region of supergradient tangential winds decelerates rapidly until the tangential component becomes subgradient again, or the radial wind speed goes to zero. The region of radial wind deceleration in the boundary layer is marked by enhanced ascent out of the boundary layer. If winds carried aloft remain supergradient, they will then have a significant outward component until they have come back into gradient wind balance with the mass field aloft. At this point, the flow should turn upward into the eyewall. The revised schematic in Figure 6b of the inner-core region of an intensifying storm is consistent with the Marks et al. (2008) flight level and radar observations from Hurricane Hugo shown in Figure 9 (their Figure 3) and Hurricane Isabel (Montgomery et al. 2006b; hereafter M06b, their Figure 3). The revised schematic is consistent also with the numerical model results of Montgomery et al. (2001, their Figure 3c and Figure 6c) and Persing and Montgomery (2003, their Figures 8, 9, and 12). For the case of Hurricane Hugo, a cross-section of the storm observed by the NOAA P3 aircraft as the storm was nearing the completion of a rapid intensification phase is shown in Figure 9. Four distinct upward vertical velocity peaks between 4 m s^{-1} and over 20 m s^{-1} occur in the intense reflectivity eyewall region. In addition, the peak horizontal wind velocities are nearly co-located with the vertical velocity and radar reflectivity maxima. As will be demonstrated in this dissertation, these observations strongly support the new model for inner-core spin-up.

To ensure an accurate assessment of the present observational study on tropical cyclone spin-up, the datasets will be described along with the analysis methodology. A brief background of the storm history will be provided for both Supertyphoon Jangmi and Hurricane Georges to provide a context for the analysis and interpretations.

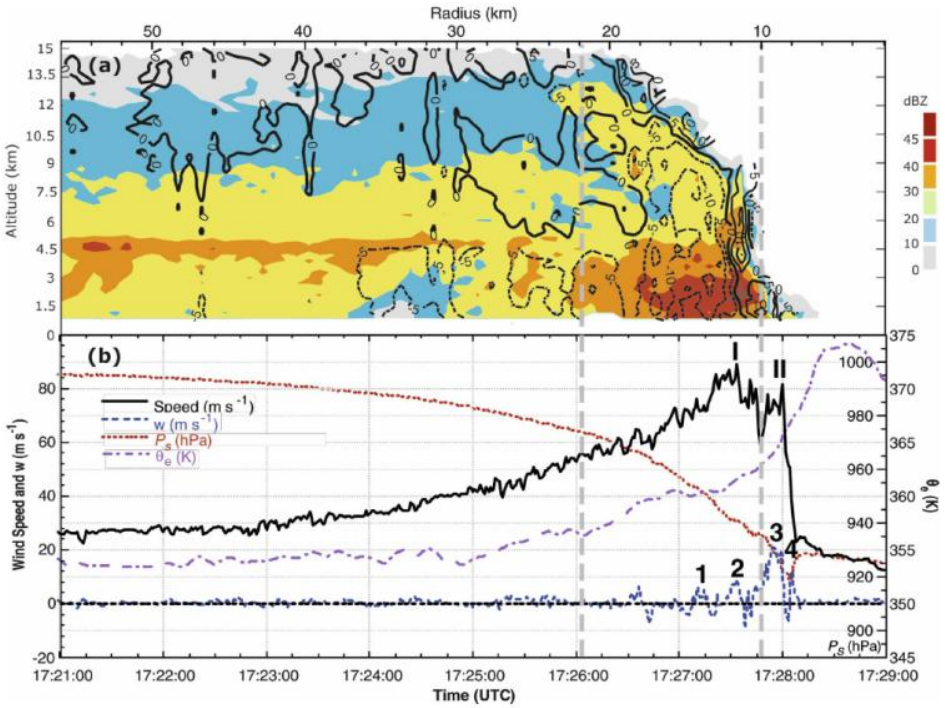

Figure 9. (a) Time versus altitude cross-section of tail radar reflectivity (dBZ) from NOAA WP-3D N42RF research aircraft for 1721 – 1728 UTC 15 September 1989. N42RF flight track was at 450 m altitude. Solid and dashed lines depict vertical velocity, and radar reflectivity is shown using color scale on the right. (b) Time series plots of (i) vertical velocity (w) in m s^{-1}, shown with dashed blue line; (ii) horizontal wind velocity in m s^{-1}, depicted by solid black line; (iii) surface pressure (P_s) in hPa, highlighted by dotted red line; and (iv) equivalent potential temperature (θ_e) in degrees Kelvin, shown with dashed dotted purple line for the period 1721 – 1730 UTC 15 September 1989. Significant updrafts are labeled 1, 2, 3, and 4, while large wind speed peaks are identified with I and II. The thick dashed lines in (b) roughly depict the outer and inner radii of intense eyewall reflectivity maxima in the lower troposphere ($1 < z < 5$ km altitude). Adapted from Figure 3 of Marks et al. (2008).

III. DATA AND METHODOLOGY

A. SUPERTYPHOON JANGMI (2008)

1. Storm History

Supertyphoon Jangmi was the most intense tropical cyclone of the 2008 season in both hemispheres. In addition, Supertyphoon Jangmi was the only Category 5 storm observed worldwide in 2008 (Wikipedia 2009). Fortunately, it weakened significantly before making its only landfall in Taiwan. As a result, only two fatalities and two missing people have been attributed to Jangmi; however, the total damage due to Supertyphoon Jangmi was $240.4 million (Wikipedia 2009). The JTWC best-track of Supertyphoon Jangmi is displayed in Figure 10.

Supertyphoon Jangmi developed from an easterly tropical wave that crossed into the western North Pacific Ocean near longitude 170°E on 17 September 2008 (M. T. Montgomery and L. Lussier 2008, personal communication). After struggling to develop for nearly a week, Jangmi organized quickly and became a tropical depression (10-min average surface winds $\geq$ 13 m s^{-1}) at 1200 UTC 23 September, approximately 435 km south-southwest of Guam (Chu et al. 2009). This tropical depression then evolved rapidly into a tropical storm just 12 hours later at 0000 UTC 24 September. The storm moved on a primarily northwestward track along the periphery of the low to mid-level subtropical ridge to the northeast. During the time period of the three WC-130J aircraft center fixes for Tropical Storm Jangmi, the translation speed increased from 6.7 m s^{-1} to 8.3 m s^{-1}.

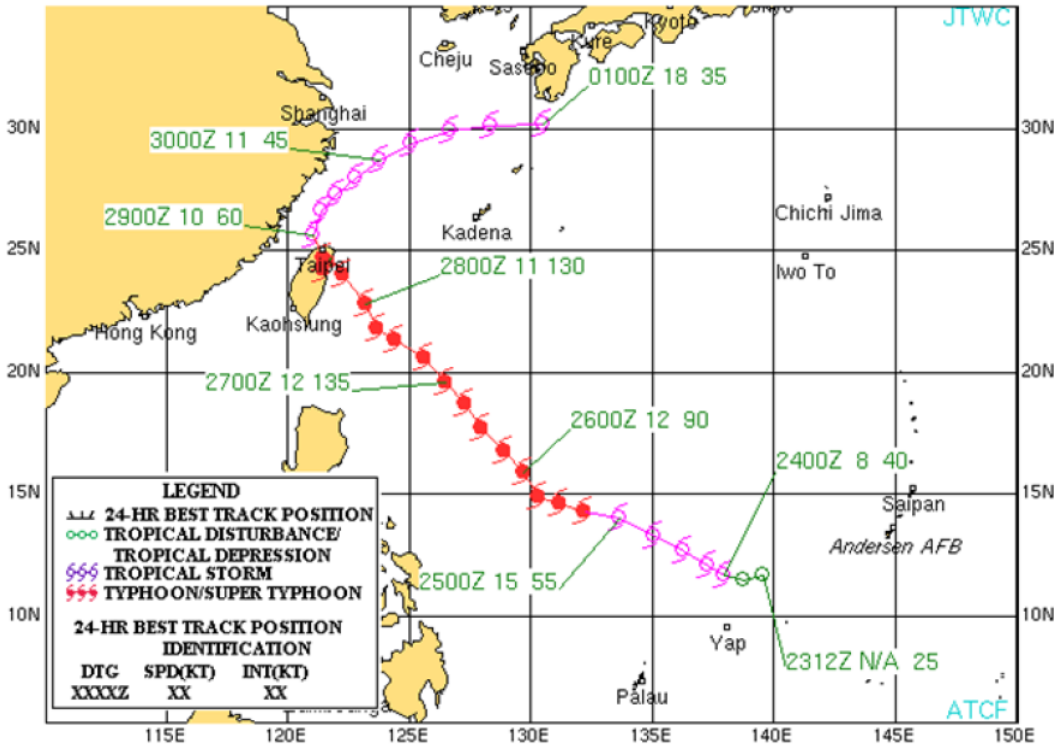

Figure 10. JTWC best-track of Supertyphoon Jangmi from Cooper and Falvey (2009). Green circle indicates tropical depression, open purple tropical cyclone symbol is tropical storm, and closed red tropical cyclone symbol is typhoon. Text indicates date-time group (DDHH), storm speed (kt), and storm intensity (kt).

Jangmi continued to intensify gradually under the influence of an upper-level anticyclone over its center and strong poleward outflow. During the third penetration of the storm by the WC-130J aircraft at 2359 UTC 24 September, the radar imagery (not shown) showed that the eye diameter decreased from around 111 km to 59 km in just over 2 h (Sanger 2008a). Six hours later, Jangmi matured into a typhoon with sustained surface wind speeds of 33 m s^{-1} and a minimum central pressure of 974 hPa at 0600 UTC 25 September (Chu et al. 2009). Over the next 18 hours, Jangmi began the first of its two rapid-intensification phases and reached an intensity of 46 m s^{-1} by 0000 UTC 26 September. The first rapid-intensification phase occurred under the following favorable conditions: (i) low vertical wind shear of only 2 - 3 m s^{-1} km^{-1} (C. Velden 2008, personal communication); (ii) high SSTs of ~ 30°C; (iii) large ocean heat content (e.g., depth of warm water) of 100 – 150 J cm^{-2}; (iv) strong upper-level divergence; and (v) high relative

humidity in low to mid-levels. These extremely favorable conditions for rapid intensification continued over the next 24 h with a decrease of the vertical wind shear to ~ 1 m s^{-1} km^{-1} (C. Velden 2008, personal communication).

Jangmi experienced a second rapid intensification phase and became a supertyphoon at 0000 UTC 27 September with an intensity of 69 m s^{-1}. This rapid intensification was verified when a USAFR WC-130J reconnaissance aircraft flying at approximately 3 km above the ocean surface measured maximum flight-level winds of 84 m s^{-1} at 0616 UTC 27 September. In addition, a dropsonde indicated a minimum central pressure of 905 hPa at 0924 UTC and a peak surface wind speed of 71 m s^{-1} at 0751 UTC (Sanger 2008c). According to the JTWC best-track data, Supertyphoon Jangmi reached its peak intensity of 72 m s^{-1} at 0600 UTC 27 September approximately 790 km southeast of Taipei, Taiwan. The storm maintained Category 5 intensity until 0000 UTC 28 September, whereupon the storm experienced a swift decrease in intensity (23 m s^{-1} in 12 h) after traveling over an area with SSTs of 26°C – 27°C and low ocean heat content of 15 – 35 J cm^{-2}. Jangmi made landfall around 0900 UTC 28 September approximately 55 km southeast of Taipei, Taiwan.

After Jangmi exited northwestern Taiwan into the western North Pacific Ocean, it started to recurve northeastward toward the Japan mainland. However, it never regained more than tropical storm strength after spending more than 24 hours over the mountainous terrain of northern Taiwan. The storm finally dissipated just south of southwestern Japan on 1 October after a nine-day life cycle.

2. Data Overview

The USAFR WC-130J and a NRL P-3 flew six research missions in Jangmi from tropical depression to supertyphoon stage. In addition, 138 GPS dropsondes and 56 Airborne Expendable Bathythermographs (AXBTs) were launched in Jangmi. The WC-130J missions were flown in Jangmi while it is was a strong tropical storm, a Category 1 storm beginning to undergo rapid intensification, and a supertyphoon with a near steady-state inner core. The NRL P-3 aircraft collected high-resolution ELDORA data in the storm while it was a weak tropical depression, a strong tropical storm, and a steady-state

Category 5 tropical cyclone. Since this research is focused on inner-core tropical cyclone spin-up, only in situ data during the tropical storm stage and above are used.

Five aircraft reconnaissance missions totaling 22 h were made in Jangmi during the tropical storm, weak typhoon, and supertyphoon stage. The start and stop time of these missions are depicted in relation to the best-track intensity in Figure 11 The USAFR WC-130J was flown into the eye and eyewall on three of these missions, while the NRL P-3 was flown primarily outside of the eyewall in the outer core during its two missions. However, the NRL P-3 was flown near the developing eyewall during the tropical storm stage of Jangmi and data collected during this mission are analyzed for this study. The four combined missions led to the collection of data that provided a unique perspective of the spin-up of a tropical cyclone into an intense, near steady-state system.

In addition to these in situ observations, a large amount of high-resolution satellite data was available for analysis. These data consisted of microwave imagery and 1-km infrared and visible satellite imagery every 30 minutes. It will be shown that these images revealed that deep convective cells were prevalent during the spin-up of Jangmi.

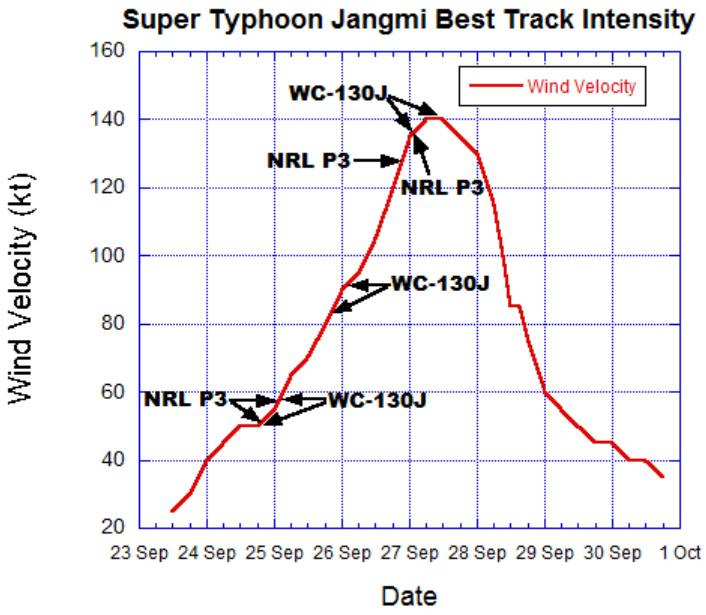

Figure 11. JTWC best-track intensity (kt) for Supertyphoon Jangmi during 23 September to 1 October 2008. Arrows indicate start and stop times of the various research missions within the storm environment.

B. HURRICANE GEORGES (1998)

1. Storm History

Hurricane Georges developed from an easterly tropical wave that crossed the African west coast late on 13 September 1998 (Guiney 1999). The NHC best-track and intensity categories of this storm are shown in Figure 12. Ship reports on 15 September revealed the presence of a low-level closed circulation. NHC declared the system a tropical depression at 1200 UTC 15 September when it was centered about 300 n mi south-southwest of the Cape Verde Islands in the far eastern Atlantic. The system became a tropical storm at 1200 UTC 16 September when it was centered approximately 620 n mi west-southwest of the Cape Verde Islands. Georges maintained a west-northwest track (i.e., standard tropical easterlies track) in response to a mid-level ridge. The vortex continued to strengthen progressively and achieved hurricane status around 1800 UTC 17 September. On 19 September, an upper-level anticyclone became firmly entrenched above Georges, and satellite imagery indicated that the storm was starting to strengthen rapidly. This rapid intensification was confirmed on 19 September when a USAFR reconnaissance aircraft measured maximum flight-level winds of 76 m s^{-1} at 2053 UTC, and a minimum central pressure of 937 hPa at 2048 UTC (Guiney 1999).

There were 27 dropsondes deployed within the eye and eyewall during the period of peak intensity of the storm from 19 – 20 September. The near-surface (below 200 m) dropsonde measurements showed maximum wind speeds between 69 m s^{-1} and 77 m s^{-1}. The maximum intensity of the storm was estimated by NHC to occur at 0600 UTC 20 September with maximum sustained surface winds of 69 m s^{-1} and a minimum central pressure of 937 hPa, while located about 285 n mi east of Guadeloupe in the Lesser Antilles (see Figure 12). The in situ data revealed that Hurricane Georges intensified rapidly within 24 h from a Category 2 storm with maximum sustained winds of 46 m s^{-1} at 0000 UTC 19 September into a borderline Category 5 storm. This rapid intensification is shown in Figure 13, which indicates that the first reconnaissance mission in Georges caught the last few hours of the rapid intensification phase.

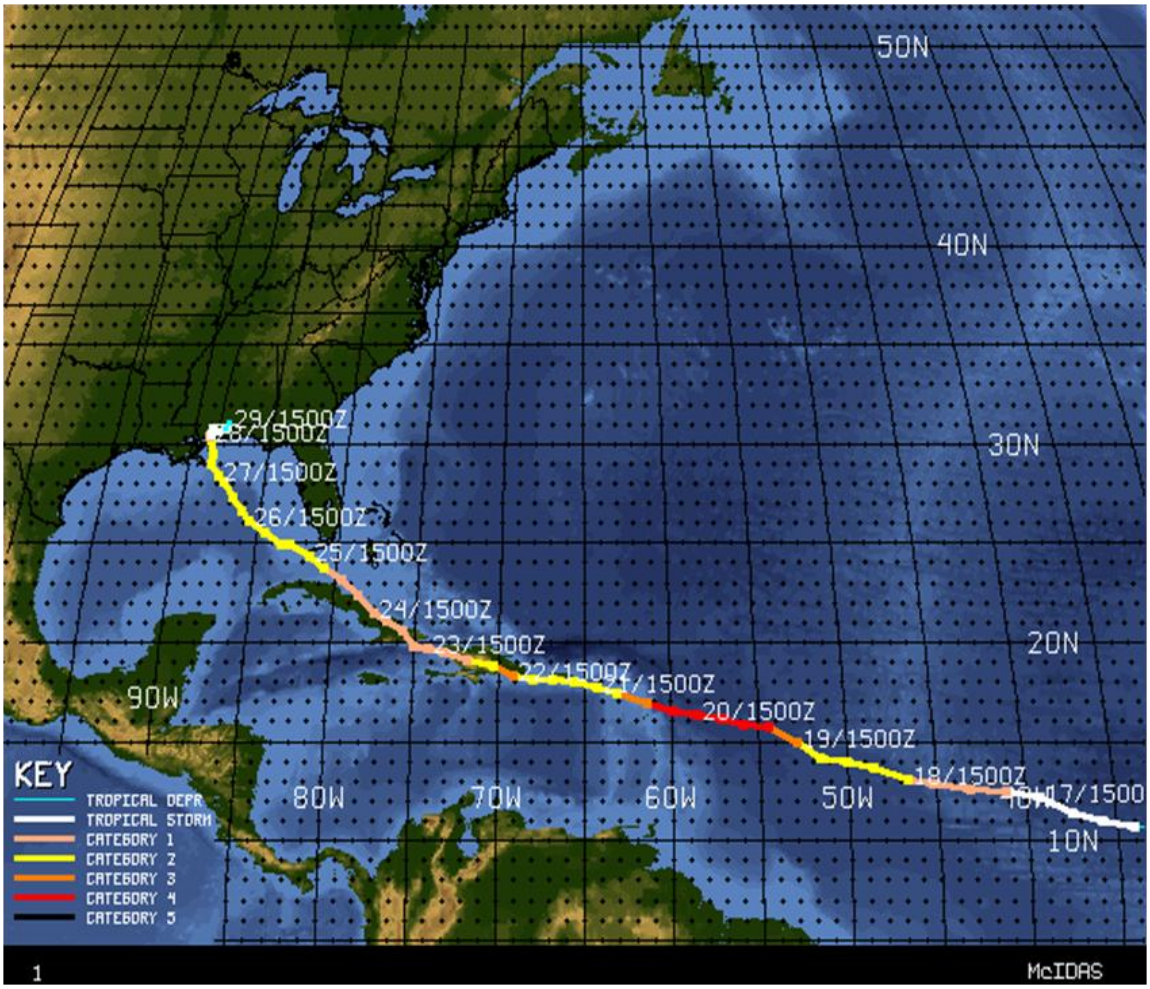

Figure 12. National Hurricane Center best-track for Hurricane Georges from 15 – 29 September 1998. The track is color coded based on the best-track intensity. The legend in lower left corner shows the Saffir-Simpson intensity scale and associated colors for each category (From CIMMS, University of Wisconsin).

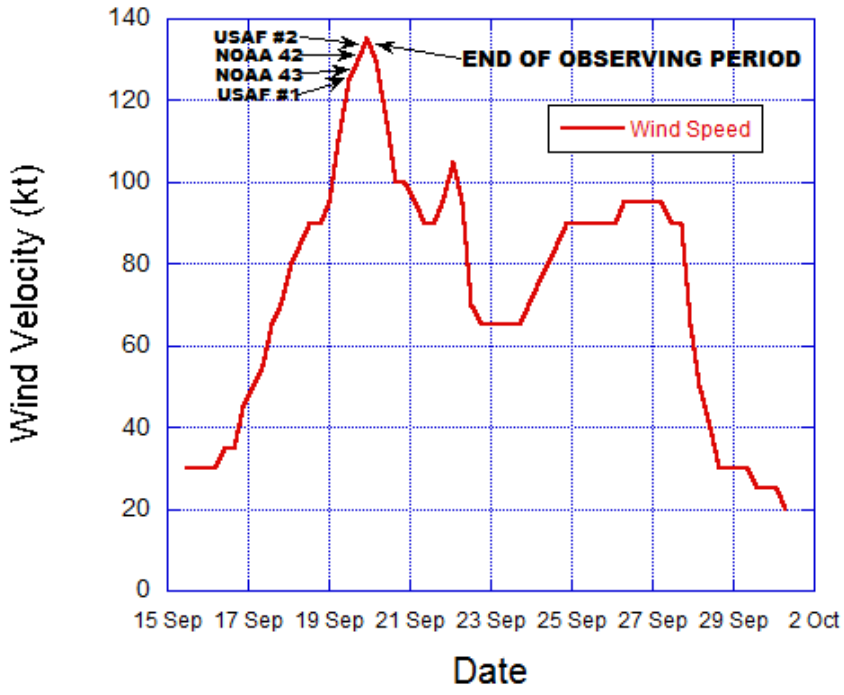

Figure 13. National Hurricane Center best-track intensity (kt) for Hurricane Georges from 15 September to 1 October 1998. Arrows indicate the start time of a reconnaissance mission in Georges with the top-most arrow showing the end of the observation period. USAF #1/USAF # 2 are the WC-130 "Hurricane Hunter" aircraft and the NOAA 42/NOAA 43 are the WP-3D aircraft.

Georges maintained Category 4 or near-Category 5 strength on the Saffir-Simpson scale from 1800 UTC 19 September to 1200 UTC 20 September. Shortly after 0600 UTC 20 September, the storm encountered strong upper-level northwesterly vertical wind shear (> 10 m s^{-1}) and began a rapid weakening with the central pressure rising 26 hPa by 1800 UTC 20 September. Despite this weakening, Georges was the second-strongest and second-deadliest hurricane in the Atlantic basin during the 1998 season (Pasch et al. 2001). Georges made eight landfalls during its 17-day journey from the northeastern Caribbean to the coast of Mississippi, and there were 602 fatalities, mainly in the Dominican Republic and Haiti.

2. Data Overview

Although the in situ data collected for Georges did not occur during TCS08/T-PARC, it addresses objectives (1) and (2) of this field experiment outlined previously in

Chapter I, Section C4a. Four reconnaissance missions in the storm were made using two NOAA WP-3s and two USAFR WC-130s during a 15-h observation period while the storm was a strong Category 4 or near Category 5 hurricane, which resulted in the release of 82 dropsondes. The dropsonde analysis will show that during the approximate steady-state period the peak tangential wind speed was occurring *within* the boundary layer. Based on observations from Jangmi that the maximum tangential wind speed occurred within the boundary layer during both spin-up and near steady-state periods and the SMN09 theoretical and modeling study showing similar results, it will be argued in Chapter 4 that the peak tangential wind was located also within the boundary layer of Georges during spin-up.

In addition to the in situ observations in Georges, the 4-km resolution GOES-8 infrared and visible satellite imagery was available at 30-minute intervals. As in the Jangmi case, this imagery reveals also that there is a frequent occurrence of deep convective clouds during spin-up.

C. IN SITU FLIGHT-LEVEL OBSERVATIONS

1. Jangmi

The 53rd Weather Reconnaissance Squadron (i.e., "Hurricane Hunters") aircrews kindly provided the High-Density/High-Accuracy (HD/HA) flight-level data that contains time (UTC), aircraft position, static pressure, geopotential height, extrapolated sea-level pressure (SLP), air temperature, dew-point temperature, wind direction, wind speed, peak 10-s average wind speed, and the peak 10-s average surface wind speed from the Stepped Frequency Microwave Radiometer (SFMR). The High-Density Observation (HDOB) message transmits 30-s averages of the HD/HA data from the USAFR WC-130J aircraft, with the exception of the peak value data mentioned above (Williamson 2009, Chap. 5).

The SFMR onboard the USAFR WC-130J provides a continuous estimate of the tropical cyclone surface wind speeds along the flight path. The SFMR measures the lowest point brightness temperature at six C-band frequencies (4.74 GHz, 5.31 GHz, 5.57 GHz, 6.02 GHz, 6.69 GHz, and 7.09 GHz) and an algorithm is used that estimates a surface wind speed based on an empirical relationship between emissivity and surface

wind speed (Uhlhorn et al. 2007). Since the surface wind speed is based partially on wave action, which is still fairly robust in the eye of developing tropical storm, the surface winds typically do not decrease to near zero at $r = 0$. The fact that the total (ground-relative) wind speed does not go to zero in the eye does not adversely impact the main results for TS Jangmi in any way, since this research is concerned with the eyewall region of the storm, not the eye. Additionally, SFMR winds are more representative of the surface tangential wind speed in the eyewall region, since the surface winds are highest there and the tangential wind dominates the radial wind. As a result, the SFMR total wind speed becomes approximated by the swirling (tangential) wind field, v, since $(u^2 + v^2)^{1/2} \cong v$.

An updated SFMR model algorithm by Uhlhorn et al. (2007) was used on all of the NOAA/Hurricane Research Division (HRD) WP-3D and USAFR WC-130J reconnaissance aircraft SFMR observations. The NOAA AOC flew SFMRs on their research aircraft for operational surface wind speed measurements in 2005 to test the accuracy of the new algorithm. There were a sufficient number of storms to provide sufficient data to measure both instrument performance and surface wind speed accuracy up to 70 m s^{-1}. It was found that the SFMR winds were accurate within ~2% at 30 m s^{-1}. In addition, the SFMR wind speeds are within 4 m s^{-1} of the dropsonde near-surface estimate. Finally, a series of statistical tests showed that the SFMR reduces the overall bias in the maximum surface wind speed by around 50% over the current flight-level wind reduction method.

The NRL P-3 1-s flight-level data were provided generously by NCAR/Earth Observing Laboratory (EOL), which is sponsored by the National Science Foundation.

2. Georges

The NOAA/HRD provided the flight-level data used in this research on Hurricane Georges. The data are available at 1-s resolution for the NOAA WP-3D and 10-s resolution for the USAFR WC-130 and consist of time (UTC), aircraft position, outside air temperature and dew-point temperature, wind direction, wind speed, geopotential height, and vertical velocity.

D. NCAR GPS DROPSONDES

The primary observational tool that was used in this research is the NCAR GPS dropwindsonde (hereafter dropsonde or sonde) produced by Väisälä. For more information on the NCAR GPS dropsondes, please refer to Appendix A.

E. DIAGNOSED TROPICAL CYCLONE CENTERS

The analysis of the inner-core structure of both Georges and Jangmi requires a conversion of the in situ data from Cartesian to cylindrical coordinates in a storm-relative reference frame. In the cylindrical coordinates, the wind field is partitioned into radial and tangential components, and decomposed into azimuthal harmonics (wavenumbers). Accurate center estimates are required for an appropriate coordinate transformation.

The Willoughby and Chelmow (1982; hereafter WC82) center-finding method is used to acquire an accurate set of center estimates for Georges. The WC82 center-finding method relies on high-resolution 1-s flight-level pressure and wind data, and is shown to be accurate to within approximately 3 km. However, the changes in the time-period between center fixes, variability of the center with height, and localized pressure and wind minima linked to mesovortices near the eye-eyewall interface, lead to difficulties in calculating an accurate set of centers for an entire storm lifetime.

The center track file for Hurricane Georges was provided kindly by the NOAA/HRD. A cubic spline fit was applied to the WC82 centers used for Georges and interpolated to a 10-min interval (S. Aberson 2009, personal communication). The 10-min track file was then used to determine a storm center for each observation point in the flight-level and dropsonde data via a simple linear interpolation. In addition, the NOAA/HRD track file provided the storm-motion vector associated with each center position. The storm movement of Georges was generally west-northwesterly with a translation speed of around 7 m s^{-1}.

Due to the unavailability of WC-130J 1-s flight-level data for Jangmi at the time of analysis, an alternate method was used to create a set of storm centers using WC-130J aircraft center fixes. The JTWC best-track centers were used to ensure a reasonable starting point for the cubic spline interpolation to the first aircraft center fix. The 0621

UTC 27 September storm center was missing from the Jangmi dataset. Since the other seven aircraft fixes correspond to the eye dropsonde position at launch time, the missing center position was obtained by using the eye dropsonde position at its release time.

The storm centers from all of the aircraft fixes and the JTWC best-track data were fit using a cubic spline interpolation method, and then linearly interpolated to a 10-min storm track file. In addition, the storm-motion vector was computed using the JTWC best-track. These storm-motion data were placed into a track file using the same interpolation methods used for Hurricane Georges. The track file was then used to determine a storm center and motion vector for each observation point along the flight track and dropsonde descent via a simple linear interpolation.

The aircraft center fixes have an accuracy to within one-half of the diameter of light and variable winds in the center (Williamson 2009, pp. 5–11). Consequently, less accuracy is expected in the storm centers during the tropical storm stage. The mean accuracy of the storm center for all three missions into Jangmi was ~ 5 km. The mean accuracy of the centers for the tropical storm, typhoon, and supertyphoon individual missions were approximately 7 km, 5 km, and 3 km, respectively. For Tropical Storm Jangmi, the three estimated aircraft center errors documented in the vortex data message were ~ 10 km, 7 km, and 5 km. Thus, the storm center accuracy of the aircraft fixes was less than the WC82 center-finding method, especially in Tropical Storm Jangmi.

To ensure the inherent center errors did not significantly affect the results, a sensitivity analysis of the storm-center errors on the radial and tangential winds was carried out for the two storms. To this end, incremental perturbations to the storm center were made in the radial direction (5 km and 10 km) and four azimuthal directions (0°, 90°, 180°, and 270°) to account for errors resulting from trochoidal oscillations, interpolation error, and vortex tilt. The perturbation of the radius was held constant, while the perturbation in azimuth was moved around the radial circle at 90-degree angles. The radial and tangential winds were computed at each perturbed point and compared to the actual values obtained using the original storm center point. An average Root Mean Squared Error (RMSE) value was computed for each of the two radial displacements using the RMSE values for each 90-degree azimuthal-perturbation point along the fixed

radius. Such a sensitivity analysis was conducted for dropsonde data at all heights and radii in the storm environment. The results of the analysis are summarized in Table 1

Table 1. Storm center sensitivity analysis for radial wind (VR) and tangential wind (VT) based on 5 km and 10 km radial displacement of storm center. Values are mean RMSE of radial and tangential winds (m s^{-1}) using 4 different azimuthal displacements with a fixed radial perturbation of 5 km and 10 km.

STORM	VR 5 km	VR 10 km	VT 5 km	VT 10 km
TS Jangmi	1.3 m s^{-1}	2.7 m s^{-1}	2.3 m s^{-1}	2.4 m s^{-1}
TY Jangmi	2.3 m s^{-1}	3.3 m s^{-1}	1.4 m s^{-1}	1.6 m s^{-1}
STY Jangmi	6.0 m s^{-1}	10.0 m s^{-1}	2.7 m s^{-1}	3.9 m s^{-1}
Georges	4.5 m s^{-1}	7.9 m s^{-1}	1.6 m s^{-1}	3.3 m s^{-1}

The storm center sensitivity for both Jangmi and Georges was analyzed by computing the RMSE of both the radial and tangential wind speeds for various perturbations to the storm center using the formula:

$$\left[\sum_{i=1}^{n}\frac{(x_1-x_2)^2}{n}\right]^{1/2}, \qquad (1)$$

where x_1 is the radial or tangential speed based on the perturbed storm center, x_2 is the radial or tangential speed using the original storm center, and n is the total number of observations. The RMSE analysis in Table 1 indicates that accurate results can be obtained from the dropsonde data for storm center errors less than or equal to 5 km. Although the storm center error for Tropical Storm Jangmi was around 7 km, the results obtained during this stage should be reasonably accurate, since the average RMSE for a 10 km center error was only 2.7 m s^{-1} and 2.4 m s^{-1} for the radial and tangential wind speeds, respectively.

To mitigate any significant errors in the analysis of TS Jangmi due to inaccurate center fixes, it was decided to use WC82 storm centers that were recently made available by NOAA/HRD. As done in Georges, a cubic spline fit was applied to the WC82 centers

and interpolated to a 10-min interval. In addition, the JTWC best-track file provided the storm-motion vector associated with each center position, which was then also interpolated to a 10-minute interval using a cubic spline fit. The resulting 10-min track file was then used to determine a storm center and motion vector for each observation point in the flight-level (every 30 s) and dropsonde data (every 0.5 s) via a simple linear interpolation.

F. COMPOSITING TECHNIQUE

A simple compositing technique was used to develop the azimuthal-mean displays of various kinematic and thermodynamical variables. The first step in this technique consisted of placing all of the dropsondes into an appropriate bin based on their location in storm-relative coordinates. The storm-track file was used to perform a decomposition into cylindrical coordinates. Each observation point in the dropsonde and flight-level data was identified according to its radius from the storm center and placed into one of the following bins: eye, outer eye, eyewall, outer core, and ambient. These bins were estimated using the RMW, radius of the eye, and the radius of gales (total wind speed > 17 m s^{-1}). The RMW was determined roughly by using the dropsonde data near the altitude of the azimuthally-averaged peak tangential wind speed. The eye bin was defined using satellite and aircraft radar imagery and dropsonde data. The eye bin consisted of an area near the center of the storm, as observed via radar and satellite, to a radius at which the tangential wind speed remains $\leq$ 10 m s^{-1}. The outer-eye bin was determined to cover the region of the eye immediately adjacent to the eyewall with tangential wind speeds $>$ 10 m s^{-1}. The eyewall region contained deep convection just outside of the outer eye as observed on satellite and radar imagery with tangential winds at least 80 percent of the RMW value. The outer-core bin was determined to be the region covering twice the RMW out to the radius of gales. The ambient region (e.g., environment) was defined approximately as the radius just beyond the outer-core region of gales to approximately 800 km. Due to differences in the eye radius and the wind field, the binned regions varied slightly between Georges and Jangmi.

The second step of the compositing process was to place the dropsondes into 50 m vertical bins between the surface and an altitude of 2000 m above the surface. The 50 m vertical bin was most effective at smoothing the data while keeping distinct signals from being completely washed out, which was essential for Jangmi since there was not a large amount of observations, especially near the surface.

The third step of the compositing technique involved linearly interpolating all of the data from each dropsonde to the 50 m vertical grid. This was accomplished using an interpolation function in the Interactive Data Language (IDL) computer program that also flagged all missing dropsonde data and determined the altitude of the last reported observation. These techniques ensured that missing data were not included in the compositing and there were no occurrences of extrapolation.

After the dropsonde observations were placed into appropriate bins and fit to the vertical grid, a mean value of selected kinematic and thermodynamical variables in each of the bins was computed at each vertical grid point. Subsequently, graphs of azimuthal-mean kinematic and thermodynamical variables were calculated for the eye, eyewall, outer core, and ambient regions of Georges and Jangmi. The thermodynamical variables of θ, θ_e, θ_v, q, and relative humidity were computed using the Bolton (1980) method.

G. SUMMARY OF CALCULATIONS TO COMPARE GRADIENT-BALANCE WINDS AND TANGENTIAL WINDS IN THE BOUNDARY LAYER

Dropsonde observations and HDOB flight-level data were used to obtain an estimate of the axisymmetric pressure gradient for the calculation of the gradient wind balance curves for both Georges and Jangmi. A six-step process was used to compare the gradient wind and tangential wind in the inner-core boundary layer region of both storms.

First, the gradient wind balance equation from Holton (2004, p. 61) is used to define the gradient wind speed:

$$\frac{v_{gr}^{\ 2}}{r} + fv_{gr} = \frac{1}{\rho_0}\frac{\partial p}{\partial r}, \tag{2}$$

where v_{gr} is the gradient tangential wind speed (m s^{-1}), r is the radius, f is the Coriolis parameter at approximately 20°N (5×10^{-5} s^{-1}), p is the pressure (Pa), and ρ is the density of air (Kg m^{-3}). The first term in Equation (2) is the centrifugal force, while the second and third terms are the Coriolis and pressure-gradient forces, respectively.

Second, Equation (2) is solved for the gradient wind speed. Since we are interested only in cyclonic flow, it is necessary to compute only positive root solutions. Thus, solving for v_{gr} in Equation (2) yields:

$$v_{gr} = \frac{r}{2}\left[-f + \sqrt{f^2 + \frac{4}{r\rho}\frac{\partial p}{\partial r}}\right]. \quad (3)$$

Equation (3) provides the basis for computing the gradient wind speed at each dropsonde grid point for a fixed altitude.

In the third step, six fixed altitudes were chosen for the gradient wind analysis: 275 m, 500 m, 750 m, 1000 m, 1250 m, and 1500 m. Selecting a standard height facilitates the calculation of the pressure gradient at a fixed altitude.

The fourth step involved performing a polynomial curve fit of pressure and radius as in Bell and Montgomery (2008). The polynomial function fits a curve through the data using the equation $y = A_0 + A_1x + A_2x^2 + A_3x^3 + \ldots + A_kx^k$, where y is the pressure (hPa), x is the radius (km), A_k are the coefficients of the polynomial, and k is the order of the polynomial. A third-order polynomial fit (k = 3) is used for the case of a strong and variable pressure gradient in the region of the eyewall. The polynomial curve fit is a form of a least squares method, which attempts to minimize the square of the local error between the original values and those predicted by the equation. The main limitation with this type of curve fit is the sensitivity to outliers in the data set.

The fifth step calculates the radial pressure gradient, $\partial p/\partial r$, in units of Pa m^{-1} using the raw polynomial curve fit of radius and pressure from step (4). The pressure gradient at each reported location was computed using the derivative function in the Kaleidagraph computer software program based on the pressure fit value at two adjacent points along the polynomial curve at the same fixed altitude starting from the outermost radius and working in toward the eye. This derivative function calculates the incremental

slope of a curve, given the x-y data points describing the curve. The function then generates a new curve and calculates the slope from the current data point and the following data point.

The last step of the analysis is to compare the gradient wind speeds in the inner and outer core of Hurricane Georges and Supertyphoon Jangmi with the actual tangential wind speeds of the dropsonde observation. The density of air was computed explicitly for each dropsonde observation using the Ideal Gas Law (e.g., $\rho = p / R_d T$), where R_d is the gas constant for dry air (287 $J\ K^{-1}\ kg^{-1}$), T is temperature in degrees Kelvin, and p is pressure in kilo-pascals. As in Bell and Montgomery (2008), moisture is not taken into account in the density calculation, which introduces a negligible error into Equation (2).

H. ANALYSIS OF DEEP CONVECTION

1. Satellite Imagery

An investigation of deep convective clouds is carried out during the spin-up of both Supertyphoon Jangmi and Hurricane Georges using high-resolution infrared, visible, and microwave satellite imagery to establish that there is a preponderance of deep convective cells (> 14 km altitude) with extremely low infrared cloud-top temperatures of ≤ -65°C. The satellite analysis will enable a quantitative assessment of the characteristics of some of the updrafts in Jangmi using results from the ELDORA mesoscale analysis of cells in TS Jangmi that were underneath extremely low cloud-top temperatures of ≤ -65°C.

2. ELDORA Data

To gain more insight into the deep convective updrafts mentioned above, NRL P-3 ELDORA data collected on 24 September during the tropical storm stage of Jangmi were analyzed. These data were used to diagnose the structure of relative vorticity, convergence, and vertical velocity underneath the very low cloud-top temperatures of the deep convective cells and to help determine if rotation was present in the low-mid levels

of the storm. These airborne radar data were provided by NCAR/EOL. For details on the design, scanning strategy, and analysis process used in this study, the reader is referred to Appendix C.

THIS PAGE INTENTIONALLY LEFT BLANK

IV. AXISYMMETRIC VIEW OF TROPICAL CYCLONE SPIN-UP

A. INNER-CORE STRUCTURE OF TROPICAL CYCLONE JANGMI: 24–27 SEPTEMBER 2008

The three-day evolution of the axisymmetric inner-core structure of Tropical Storm Jangmi, Typhoon Jangmi, and Supertyphoon Jangmi in the radial and vertical plane is conducted utilizing in situ high-density flight-level observations and 39 eye and eyewall dropsondes released during all three stages of the storm. The dropsondes were deployed from a USAFR WC-130J flying at an altitude of approximately 3 km and a NRL P-3 cruising at around 3.5 km altitude. The dropsonde paths and multiple aircraft radial penetrations into Jangmi as a tropical storm, typhoon, and supertyphoon are shown in Figures 14a,c,e. The radial and vertical coverage of the dropsonde data points are shown in Figures 14b,d,f. The modest number of dropsondes released in the inner core of Jangmi was a result of having only one plane available to conduct reconnaissance missions in the high wind region of the storm and because of long ferry times to the storm of three to four hours during the typhoon and supertyphoon stages.

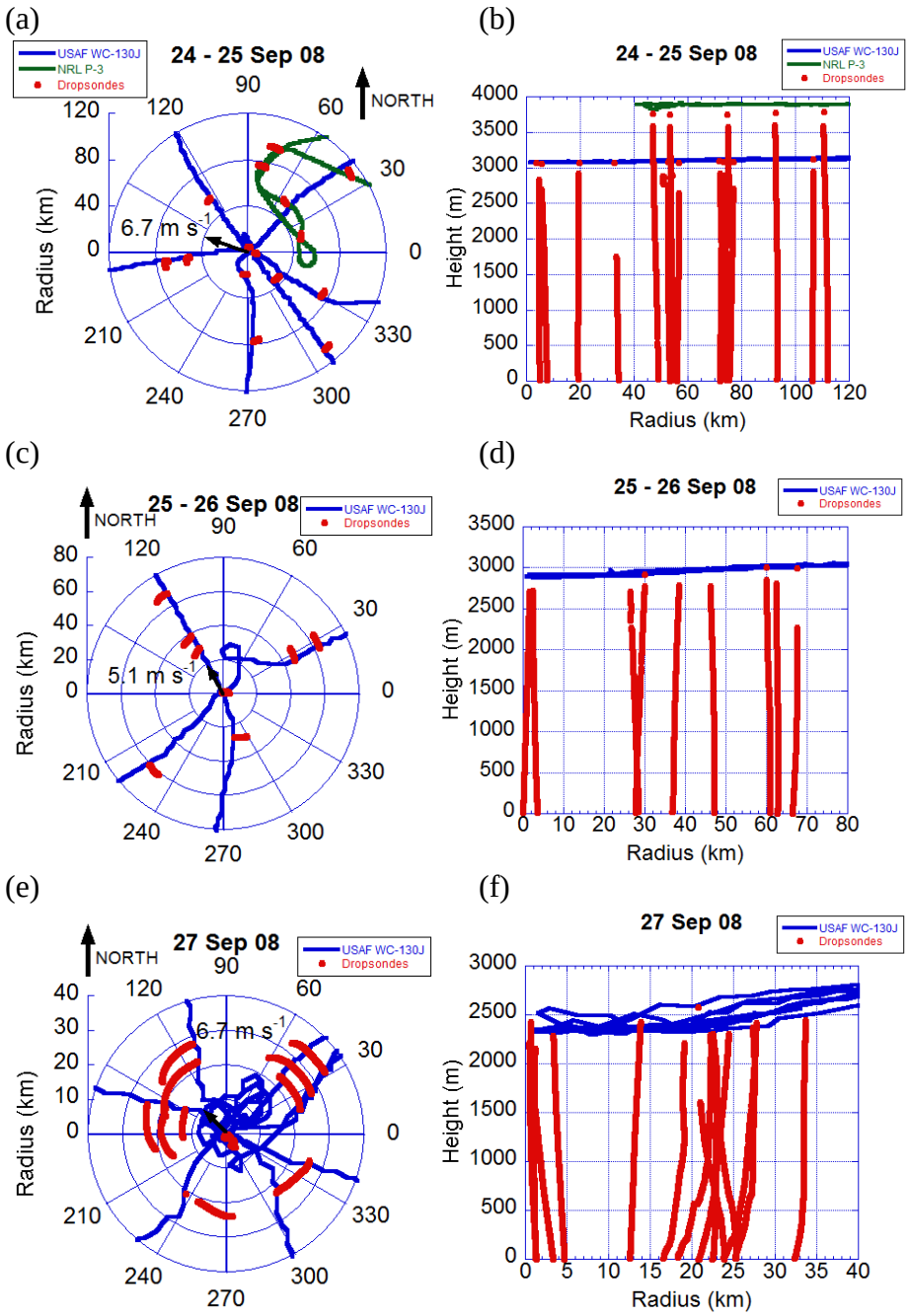

Figure 14. Dropsonde locations, trajectories, and aircraft flight tracks from 24 – 27 Sep 2008. Storm-relative data distributions in geographical radius-azimuth (*R*-θ) coordinates (a,c,e) and radius-height (*R*-*Z*) coordinates (b,d,f). The plots display the WC-130J track (blue), the NRL P-3 track (green), and dropsonde trajectories (red). Dropsondes move cyclonically in (a,c,e). The horizontal scale is not the same in the three sets of panels: In (a,b) the horizontal scale is 120 km; in (c,d) the scale is 80 km; and in (e,f) the scale is 40 km. The thin black arrow in the center of (a), (c), and (e) is the storm motion vector, with storm translation speed indicated in light black (m s^{-1}).

1. Observed wind field characteristics

a. Dropsondes

The near-surface locations of the Jangmi eyewall dropsondes are shown in Figures 15a,c,e and the storm-relative tangential wind speeds for all three stages of the storm are displayed in Figures 15b,d,f. The altitudes of the tangential wind plots coincide with the estimated height of the maximum tangential wind speed in the eyewall for each day. The red squares in Figure 15a depict significant supergradient tangential wind observations based on the dropsonde-derived gradient wind curve to be discussed in more detail in the upcoming sections and in Figure 19b.

The three-day evolution of the tangential wind speed reveals a significant structure change. In the tropical storm stage, the tangential wind speeds lack a distinct increase with decreasing radius. In addition, there is high variability in the wind speeds. During the typhoon and supertyphoon stage, the wind speeds exhibit a distinct increase with decreasing radius up to the RMW and display much less variability. Furthermore, the RMW becomes much more defined and closer to the storm center. Based on Figures 15d,f, the RMW is estimated to be 55 km for Typhoon Jangmi and 24 km for Supertyphoon Jangmi. Due to the horizontally expansive, asymmetric wind field and the small number of observations in TS Jangmi, it was decided to use the SFMR data to obtain a more accurate estimate of the RMW.

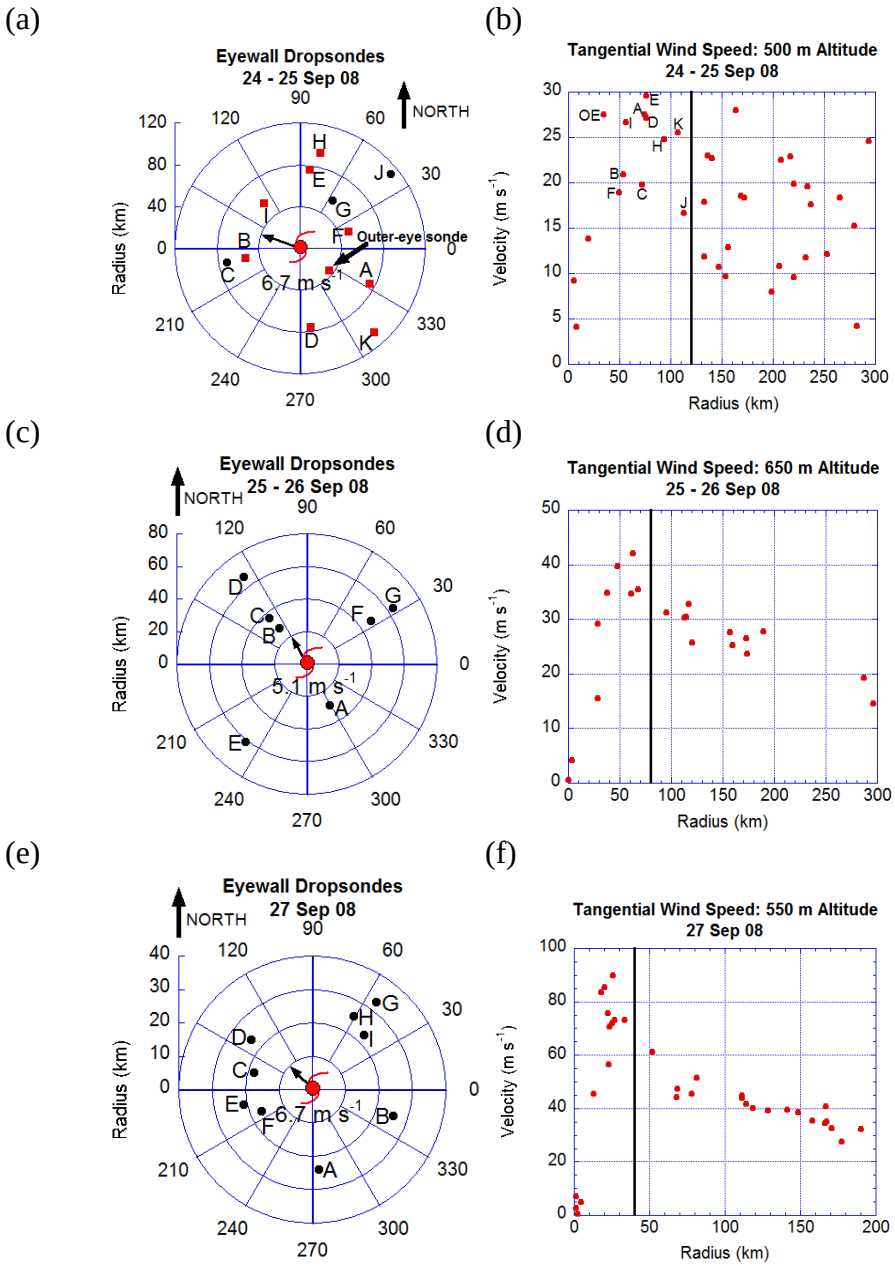

Figure 15. (a) Near-surface radius versus azimuth displays of *only eyewall dropsondes* in geographic-oriented coordinates; dropsondes listed in order (A-K) for (a) TS Jangmi, (c) TY Jangmi, and (e) STY Jangmi. (b) Storm-relative tangential wind (m s^{-1}) from dropsonde observations versus radius out to 300 km radius at an altitude of ~ 500 m for TS Jangmi (red dots), (d) same as (b) but at ~ 650 m altitude out to 300 km for TY Jangmi, and (f) same as (b) but at ~ 550 m altitude out to 200 km for STY Jangmi. Thin, black arrow depicts storm motion vector with storm translation speed indicated in light black text near the storm translation vector (in m s^{-1}). Vertical black line delineates the start of the inner-core region of the storm. Red squares in (a) show significant supergradient tangential winds shown later in Figure 19b.

b. Stepped Frequency Microwave Radiometer (SFMR)

To help mitigate the impact of the asymmetric wind field in TS Jangmi on determining the RMW, we take advantage of the high temporal resolution (every 30 s) characteristics of the SFMR total surface wind speed observations from the HDOB flight-level data (Table 2) and flight-level tangential wind speed (see Ch. III, Section C for more details on SFMR data). The RMW at flight level and the surface was estimated using a third-degree polynomial curve fit of the flight-level tangential wind and SFMR total wind for each quadrant. Then, a third-degree polynomial curve was fit to all of the data points (not shown) to estimate the axisymmetric mean RMW (see Figure 16 below). The FL RMW average was ~100 km and the SFMR RMW was ~75 km. The RMW for each quadrant is shown in Table 2 below. There is not much quadrant variation in the SFMR RMW. However, there is more disparity in the flight-level RMW.

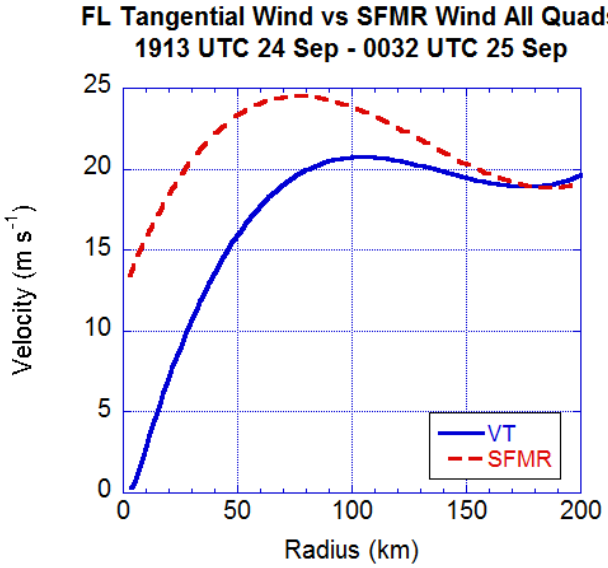

Figure 16. TS Jangmi axisymmetric flight-level tangential wind speed in m s^{-1} (solid blue curve) and SFMR total wind speed in m s^{-1} (dashed red curve) estimated by a third-degree polynomial curve fit of the dropsonde observations in all quadrants from 1913 UTC 24 Sep 08 to 0032 UTC 25 Sep 08. The plot reveals an SFMR RMW of ~ 75 km and a flight-level RMW of ~100 km.

Table 2. Radius of maximum total surface wind speed (RMW) in six quadrants based on Stepped Frequency Microwave Radiometer (SFMR) observations listed in chronological order from the first radial leg to the last radial leg (East-Southeast-ESE, West-Southwest-WSW, South-Southeast-SSE, Northeast-NE, Northwest-NW, and Southeast-SE) for TS Jangmi from 1856 UTC 24 Sep 08 to 0048 UTC 25 Sep 08. The SFMR data was collected along three WC-130J radial legs that were flown while penetrating the storm center. Due to storm asymmetry, a third-degree polynomial curve fit of the observations was used to identify the RMW in each quadrant.

QUADRANT	TIME	SFMR RMW	FL RMW
ESE	1856-1947 UTC 24 Sep	75 Km	125 Km
WSW	1947-2022 UTC 24 Sep	70 Km	125 Km
SSE	2114-2147 UTC 24 Sep	90 Km	90 Km
NE	2147-2257 UTC 24 Sep	65 Km	100 Km
NW	2258-2352 UTC 24 Sep	85 Km	120 Km
SE	0000-0047 UTC 25 Sep	65 Km	70 Km

2. Gradient Wind Balance Analysis Overview

An investigation into whether or not supergradient winds were present in the boundary layer during the spin-up of Jangmi is carried out using the method outlined in Section G of Chapter II for the dropsonde-derived pressure observations. The calculations assume that the data may be meaningfully composited together and treated as a reasonable estimate of the azimuthally-averaged structure in the inner-core region of the storm. The analysis was performed at six altitudes: 275 m, 500 m, 750 m, 1000 m, 1250 m, and 1500 m.

The HDOB extrapolated sea-level pressure data were used to estimate the radial pressure gradient at the six altitudes and compute the gradient wind speed for both TS Jangmi and Supertyphoon Jangmi. Recalling the boundary layer approximation that the radial pressure gradient is nearly constant with height within the boundary layer, the HDOB pressure fit based on the extrapolated sea-level pressure field was used for all six vertical levels within this boundary layer region. The higher temporal resolution (every 30 s) HDOB extrapolated sea-level pressure observations were used to help mitigate the impact of computing the gradient wind in an asymmetric storm such as TS Jangmi. The extrapolated sea-level pressure data were not available for Typhoon Jangmi.

The gradient wind analyses were carried out using a software program called Kaleidagraph to calculate a polynomial curve fit of pressure with respect to radius. As described in Section G of Chapter 3, the Kaleidagraph program uses this curve fit to differentiate radially the pressure field. The resulting radial pressure gradient is then used to calculate the appropriate gradient wind profile in the boundary layer, following Equation (3) from Chapter 3, Section G, for the six altitudes given above.

a. Limitations of Dropsonde Compositing Method

Despite the accuracy and reliability of the dropsondes, there are some significant limitations of using a composite axisymmetric mean pressure gradient based on dropsondes due to significant asymmetries in TS Jangmi, irregular spacing of observations in both time and space, and uncertainties in the pressure, wind speeds, and storm centers. There is some uncertainty also in the positions of the surface pressure estimates associated with the center fix position because a curve is being fit to the data and the center position is an anchor in that curve-fitting. Additional uncertainty arises because of the variable locations of the maximum surface pressure gradients along each radial leg, and those maximum surface pressure gradients are varying in time and space over the five-hour mission. In addition, the small number of dropsondes, and their irregular distribution in time and space, may result in large uncertainty in the gradient wind using a composite methodology. Furthermore, changes in the storm translation speed and intensification may also create additional errors. During the five-hour reconnaissance mission, TS Jangmi was beginning to undergo rapid intensification and increased its translation speed from 6.7 m s^{-1} to 8.3 m s^{-1}.

The possible significant uncertainty in the gradient wind as a result of these issues discussed above prevents one from making any strong conclusions on the presence of supergradient winds in TS Jangmi. All of these limitations make it clear that a dense deployment of dropsondes across the RMW in each radial leg will be necessary to validate whether or not axisymmetric supergradient winds exist during the tropical storm stage.

Although TS Jangmi's primary circulation is asymmetric during the period of investigation, it is still feasible to define a symmetrically-averaged circulation for analysis of the gradient wind. It is possible also to define an agradient wind relative to this circulation. However, these two definitions above do not allow for strongly conclusive statements about the agradient winds in an asymmetric storm such as TS Jangmi. One may certainly call into question the meaning of this agradient wind in general, but the methodology used to calculate this quantity follows what others have accomplished in the peer-reviewed literature (e.g., Kepert 2006, Bell and Montgomery 2008), albeit not for an asymmetric storm such as TS Jangmi. As discussed shortly in Section 1c below, it is simply not possible to obtain an accurate and meaningful estimate of the agradient wind along a certain azimuth, since there is no method to determine the local radius of curvature of the air parcel trajectories within the boundary layer. This is most likely the reason why Kepert (2006) and others have decided to use the azimuthally-averaged wind field to diagnose agradient wind effects in the boundary layer of a tropical cyclone's inner-core region.

b. Analysis of Asymmetry in Tropical Storm Jangmi

To assess roughly the degree of asymmetry in TS Jangmi, quadrant-by-quadrant plots of flight-level geopotential height, flight-level tangential wind speeds, and extrapolated SLP were created (see Figures 17a,b,c, and Figures 50 - 52 in Appendix M). Additionally, a standard deviation analysis of the extrapolated SLP was performed (see Table 3, Appendix M).

The quadrant by quadrant radial plots of observed geopotential height from flight-level observations and the axisymmetric average (based on a 3rd-order polynomial curve fit) of the HDOB observations in all quadrants reveal that TS Jangmi contained non-trivial deviations in the radial gradients of the geopotential height (Figure 17b; Figures 50a-f, Appendix M). These deviations will negatively impact the significance of the gradient wind calculations using the dropsonde compositing method. However, the largest asymmetry in geopotential height lies outside of the RMW in the outer core of the storm, which is the not the focus of this study.

The quadrant by quadrant radial plots of extrapolated SLP from flight-level observations and the axisymmetric average (based on a 3rd-order polynomial curve fit) of the HDOB observations in all quadrants reveal that TS Jangmi had non-trivial deviations in the radial pressure gradient (see Figure 17c; Figures 51a-f, Appendix M). These results are consistent with those above for the geopotential height shown in Figure 17b.

The standard deviation analysis in Table 3 of Appendix M shows that all quadrants contain roughly the same amount of variation in the pressure observations. Thus, the axisymmetric average pressure gradient is considered representative and useful for diagnosing the presence of supergradient winds.

The radial plots of the flight-level tangential wind speed and the axisymmetric average using a 3rd-order polynomial curve fit of all data points in each quadrant show that there are relatively large variations in the flight-level tangential wind speeds (Figure 17a; Figures 52a-f, Appendix M). The RMW ranges from a minimum of ~70 km in the southeastern quadrant to a maximum of ~125 km in the northwestern quadrant (see Table 2 above). In addition, there is a significant spread of tangential wind speeds within each quadrant near the same radius. All quadrants, with the exception of the northwestern quadrant, have speeds > 20 m s^{-1} within 100 km radius of the storm center. Despite having a large RMW, the northwestern quadrant still has tangential wind speeds > 20 m s^{-1} within a 125 km radius of the center. Lastly, along each radial leg, there are large tangential wind speeds relative to the composite mean within the eyewall of TS Jangmi.

There is no question that TS Jangmi has significant wind and pressure asymmetries. However, there is relatively less asymmetry seen in the pressure field than in the tangential wind field. Only the pressure gradient is explicitly required in the calculation of the gradient wind speed. However, the asymmetries observed in the pressure field are non-trivial and are likely to result in a negative impact on the significance of the azimuthally-averaged supergradient wind using dropsondes.

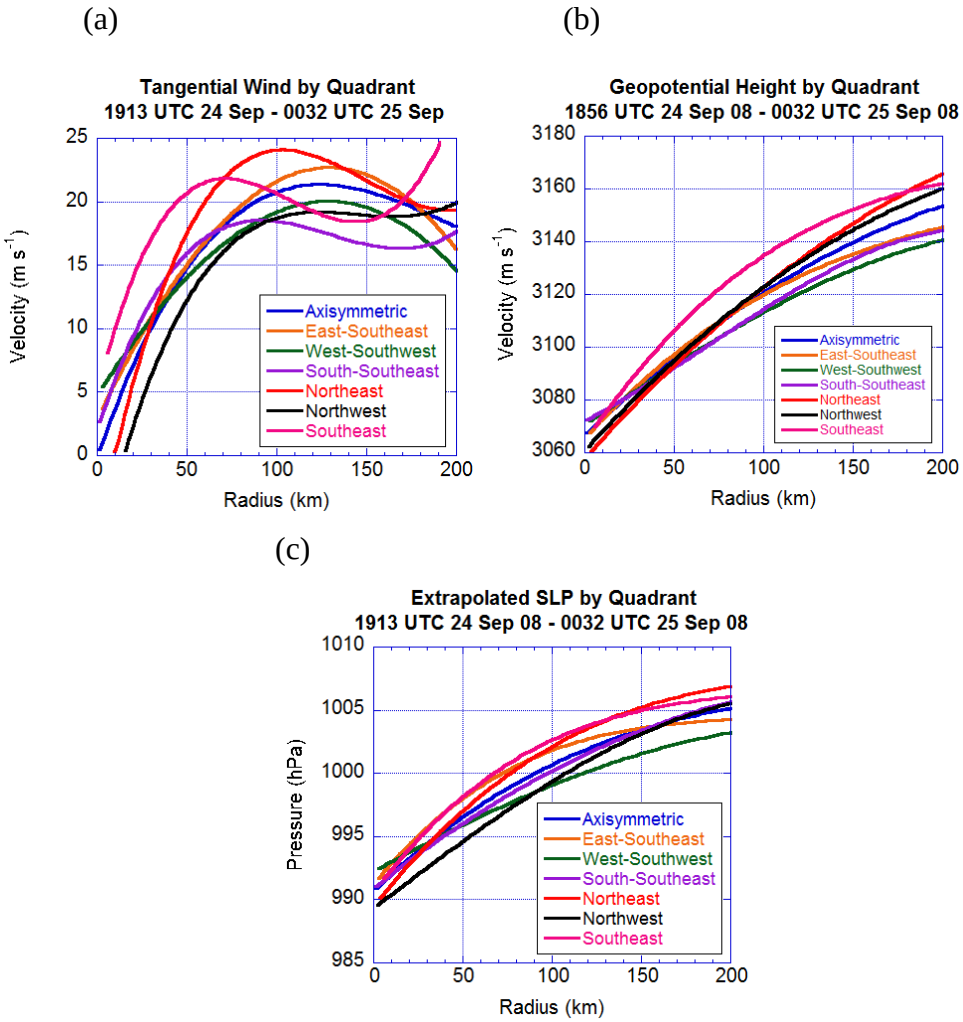

Figure 17. (a) 3rd-order polynomial curve fit of (a) flight-level tangential wind speed (m $s^{-1)}$; (b) geopotential height (m); and (c) extrapolated SLP from HDOB flight-level data (hPa) for each quadrant of TS Jangmi (orange-ESE, green-WSW, purple-SSE, red-NE, black-NW, pink-SE) and axisymmetric value (blue) from 1913 UTC 24 Sep to 0032 UTC 25 Sep.

c. Limitations of HDOB Extrapolated Sea-Level Pressure

Although the HDOB flight-level data provide estimated sea-level pressure observations every 30 s to help alleviate the asymmetry problem, there are significant limitations associated with using the gradient wind curve derived from these observations: (i) the HDOB extrapolation method assumes that the radial pressure gradient in the boundary layer, and near the surface in the eyewall region in particular, is essentially the same as at flight level; however, there is generally a slow increase of the

temperature field with decreasing radius as the plane flies towards the center of circulation; (ii) there are significant upward and downward vertical velocities in the eyewall region between flight level and the boundary layer, which raises a concern about the strict validity of the hydrostatic approximation (see Figure 36 in Chapter 5, Section C3); (iii) there is a lack of peer-reviewed publications detailing the accuracy of the extrapolated sea-level pressure observations near the RMW of the storm for the tropical storm, typhoon and supertyphoon stages; and (iv) a manual quality control check of HDOB-derived surface pressure data revealed frequent occurrences of spurious observations. All of these factors present a challenge in determining meaningful uncertainty estimates for the gradient wind in the boundary layer region using the extrapolated sea-level pressure data.

The foregoing assumption that the radial pressure gradient in the boundary layer is essentially the same as at flight level is questionable in the boundary layer of the developing eyewall region of the storm. In this region, the air is rapidly decelerating and the corresponding pressure gradient must decrease in step. Stated in another way, the extrapolation method is not consistent with Newton's 2nd Law of motion in the radial direction, which generally requires that the dynamic contributions to the pressure be accounted for in the inner-core region of the storm. The inconsistency is shown in the comparison of the plots of HDOB and dropsonde-derived pressure profiles for TS Jangmi and Supertyphoon Jangmi (Figures 18b,d). To aid comparison of the two datasets, the flight-level extrapolated sea-level pressures were reduced using a constant offset of 55 hPa and 47 hPa in TS Jangmi and Supertyphoon Jangmi, respectively. The offset value was determined by subtracting the HDOB pressure value from the dropsonde pressure value at a radius of 75 km in TS Jangmi and 25 km in Supertyphoon Jangmi. These two radii were chosen since they were located near the RMW. It is clear from Figure 18b that for the tropical storm stage there is only a small discrepancy between the HDOB-derived radial pressure profile and the dropsonde-derived radial pressure profile in the boundary layer of the eyewall region. Thus, for TS Jangmi, it is seems reasonable to use the HDOB extrapolated SLP to calculate the gradient wind speed, especially in light of the large pressure asymmetries implied in Figure 18a below and discussed above in Section

2b. In the supertyphoon stage, the discrepancy in the pressure profiles increases in magnitude on account of the increase of dynamic accelerations within and immediately above the boundary layer (see Figures 18c,d below).

The limitation of the assumption of an unchanged radial pressure gradient from flight level downward to the boundary layer in the eyewall region of Category 5 Hurricane Isabel was analyzed and discussed in Bell and Montgomery (2008; hereafter BM08). They performed an inward integration of the azimuthally averaged radial momentum equation using a Boussinesq approximation in storm-center cylindrical coordinates to estimate contributions of each term:

$$-\frac{\partial \bar{p}}{\rho \partial r} = \left(-\frac{\bar{v}^2}{r} - f\bar{v} \right) + \frac{D\bar{u}}{Dt} + F \,, \tag{4}$$

$$F = -\left(\overline{v'^2}\right)/r + \partial\left(\overline{ru'^2}\right)/r\partial r + \partial\left(\overline{u'w'}\right)/\partial z \,, \text{ and} \tag{5}$$

$$D\bar{u}/Dt = \partial\bar{u}/\partial t + \bar{u}\partial\bar{u}/\partial r + \bar{w}\partial\bar{u}/\partial z \,, \tag{6}$$

where F represents the mean eddy flux divergence; $D\bar{u}/Dt$ is the material derivative of the average radial wind; u, v, and w are the cylindrical velocity components; t is time; f is the Coriolis parameter (assumed constant); p is the total pressure, and ρ is the total density. The overbar identifies the azimuthal average and prime notation signifies perturbations from the azimuthal average. Their results showed that *the transverse advection and eddy flux divergence terms act in concert to offset the cyclostrophic and Coriolis accelerations and reduce the radial pressure gradient. These two terms increase the pressures by as much as 6 hPa to 8 hPa in the eyewall region at ~ 100 m altitude, well within the boundary layer* (see Figure 19a).

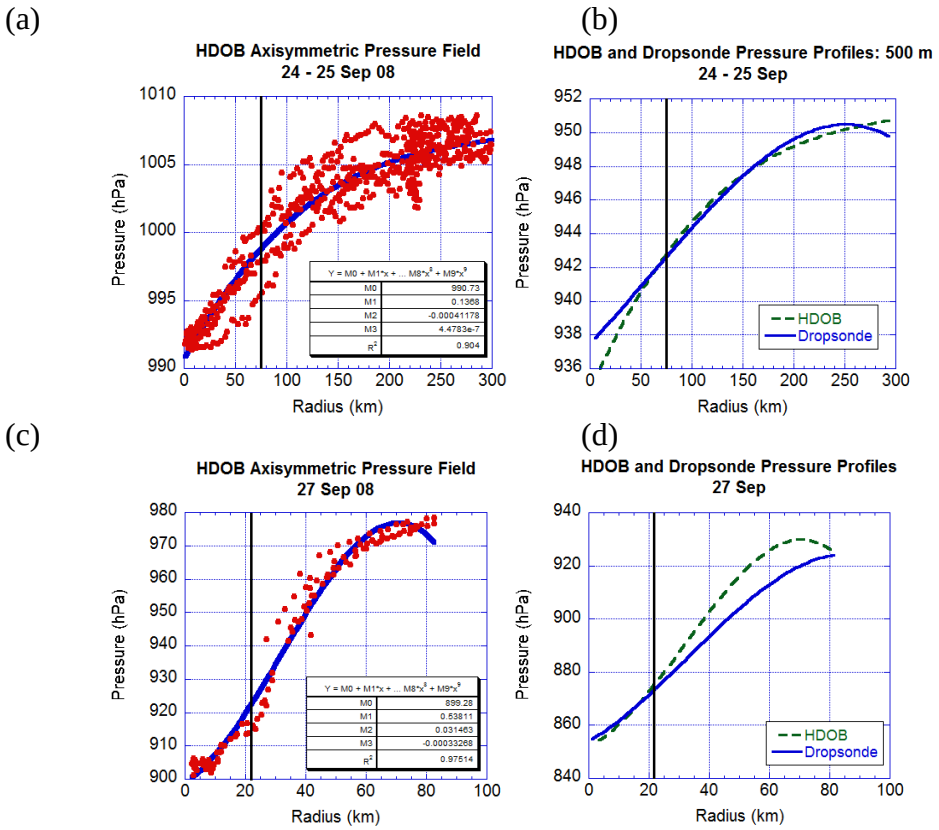

Figure 18. Observed extrapolated sea-level pressure (hPa) from HDOBs as a function of radius (solid red circles) and 3rd degree polynomial fit of these observed pressures (solid blue line) from (a) 1856 UTC 24 Sep 2008 – 0119 UTC 25 Sep 2008 and (c) 0318 – 1022 UTC 27 Sep 2008. Inset tables show curve fit coefficients with r^2 values of 0.90 (panel a) and 0.98 (panel c). The solid black vertical lines in (a-d) denote the mean RMW determined from the SFMR data shown in Figure 16. Panels (b) and (d) show plots of radial pressure profiles (in units of hPa) at 500 m altitude estimated by a 3rd-order polynomial curve fit of in-situ dropsonde observations (solid blue line) and a 3rd-order polynomial curve fit of HDOB extrapolated sea-level pressure for (b) Tropical Storm Jangmi and (d) Supertyphoon Jangmi. The HDOB extrapolated SLP was reduced using a constant offset of 55 hPa and 47 hPa in (b) and (d), respectively. The offset value was determined by subtracting the HDOB pressure value from the dropsonde pressure value at a radius of 75 km in (a) and 25 km in (c). These two radii were chosen since they were located near the RMW between the HDOB-derived curve and the dropsonde-derived curve. The HDOB curves near the RMW in (b) and (d) have a steeper slope than the dropsonde curves, which is consistent with the findings of BM08 discussed above. For reasons discussed in the main text, the difference between the two curves is expected to increase as the storm strength increases. The solid black vertical lines in (a-d) denote the mean RMW.

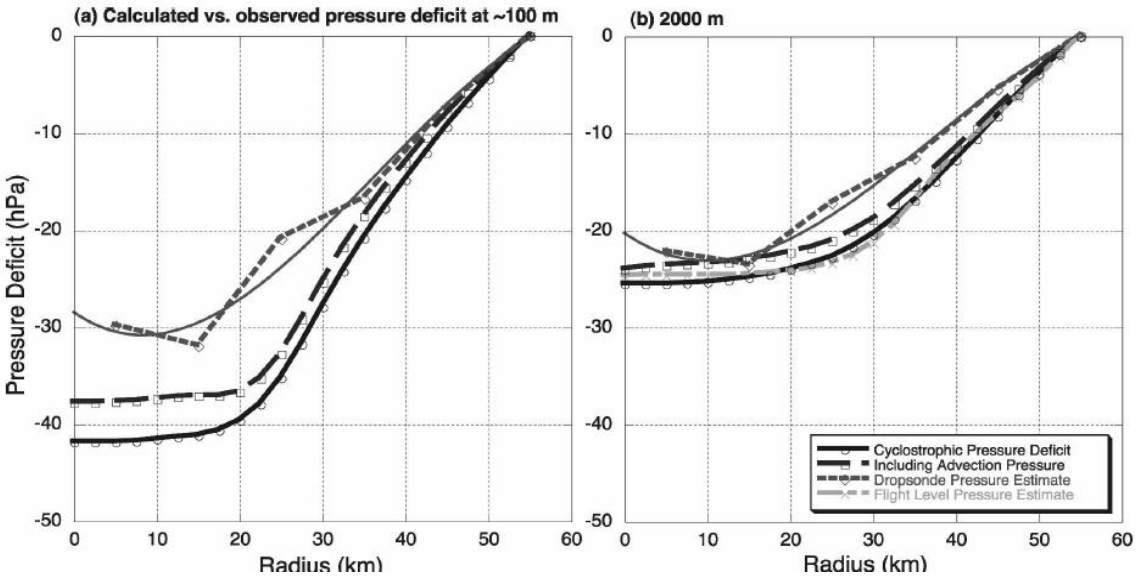

Figure 19. Calculated pressure deficit in Category 5 Hurricane Isabel obtained by integrating the radial pressure Equation (4) inward from 55-km radius with (dark gray dashed curve; square) and without (black solid curve; circles) advection terms versus the pressure deficit observed by dropsonde data (light gray dotted curve; diamonds) at (a) 100-m altitude and (b) 2-km altitude. The third-degree polynomial fit of the observed pressure deficit at each altitude is shown by the light gray thin curves. Adapted from BM08 Figure 8.

d. Using Extrapolated Sea-Level Pressure to Calculate the Gradient Wind in Each Quadrant

Since there is very little difference between the dropsonde and HDOB pressure gradients as noted in Figure 18b, it is reasonable to use the flight-level extrapolated sea-level pressure, with the aid of the hypsometric equation, to calculate the gradient wind in the boundary layer of each quadrant of the storm. However, this method is not without difficulties. For one thing, one has the same problem as discussed above in computing the pressure gradient in the boundary layer across the streamline. For another thing, there is no way to determine the local radius of curvature in the boundary layer with the dataset at hand. Holton (2004, Ch. 3, Section 3.2) discusses the requirement of knowing the local radius of curvature to compute the local gradient wind speed, *V*, and shows this necessity in his Equation 3.15:

$$V = -\frac{fR}{2} \pm \left(\frac{f^2 R^2}{4} + fRV_g \right)^{1/2}, \tag{7}$$

where, f is the Coriolis parameter, R is the radius of curvature following the parcel motion, and V_g is the geostrophic wind. Nevertheless, due to the large storm asymmetry, it is important to conduct a quadrant-by-quadrant gradient wind analysis using the HDOB extrapolated SLP data, which have much more frequent observations than the dropsonde dataset.

3. Axisymmetric Gradient Wind Results

All of the pressure curve fits derived from the HDOB and dropsonde pressure observations were judged excellent with coefficient of determination values (r^2) between 0.89 and 0.98 (Figures 18a,c, Figures 18a,c,e; Figures 39a,c,e,g,i in Appendix C; Figures 40a,c,e,g,i in Appendix D; and Figures 41a,c,e,g,i in Appendix E). The coefficient of determination in this case is the amount of variation in pressure (i.e., *y*-ordinate) that can be explained by the regression line. Thus, for all three days, between 89% and 98% of the total variation in pressure can be explained by the regression line. However, for TS Jangmi, there is a large degree of asymmetry as implied from the pressure field in Figure 18a.

The gradient wind analyses in Jangmi suggests the presence of supergradient winds near and just inside of the RMW at all six altitudes during the entire spin-up of the storm (Figures 20b,d,f; Figures 39b,d,f,h,j in Appendix C; Figures 40b,d,f,h,j in Appendix D; and Figures 41b,d,f,h,j in Appendix E). The dashed blue curves are the gradient wind estimates derived from dropsondes and the dashed green curves are an independent estimate using HDOBs, when they are available. For all three days, the tangential winds are most supergradient near and just within the RMW relative to the dropsonde-derived axisymmetric mean gradient wind curve. Although dynamical reasons have been given to support the existence of supergradient winds in the boundary layer during the entire intensification process, more dropsonde observations are required for the early stages of intensification in many storms to make a definitive statement about the ubiquity of supergradient winds during the tropical storm stage.

From the analysis below, the degree to which the tangential winds are supergradient near and just within the RMW in the tropical storm, typhoon, and supertyphoon stages of the storm ranges from an average value of approximately 25%, 14%, and 35% respectively. The peak mean supergradient winds typically occur just within the RMW. These analyses suggest also that there are subgradient winds observed within the inner core during all three stages of the storm, primarily just outside of the RMW. As shown in SMN09, the presence of subgradient winds outside the RMW is a result of frictionally-reduced tangential flow within the boundary layer (i.e., agradient force < 0).

a. Boundary-Layer Depths Summarized

Based on the gradient wind balance analyses, the inner-core dynamic boundary-layer depth is estimated to be at least 1250 m for TS Jangmi, 1500 m for Typhoon Jangmi, and 1500 m for Supertyphoon Jangmi. These boundary layer depths are based on the definition in Chapter II, Section B5 (layer of significant gradient wind imbalance). Since the gradient wind balance analysis was carried out at six heights up to only 1500 m, an approximation is made that the boundary layer is at least as deep as the last level of significant gradient wind imbalance. Thus, the dynamic boundary layer heights estimated in Jangmi, represent the lowest depth of the inner-core boundary layer. It is useful to recall again that it is challenging to define a precise boundary layer depth in the inner-core region, where there is strong upward vertical motion. In the next section, the estimated boundary layer depths will now be used to study inner-core spin-up using the kinematic composites of radial and tangential wind.

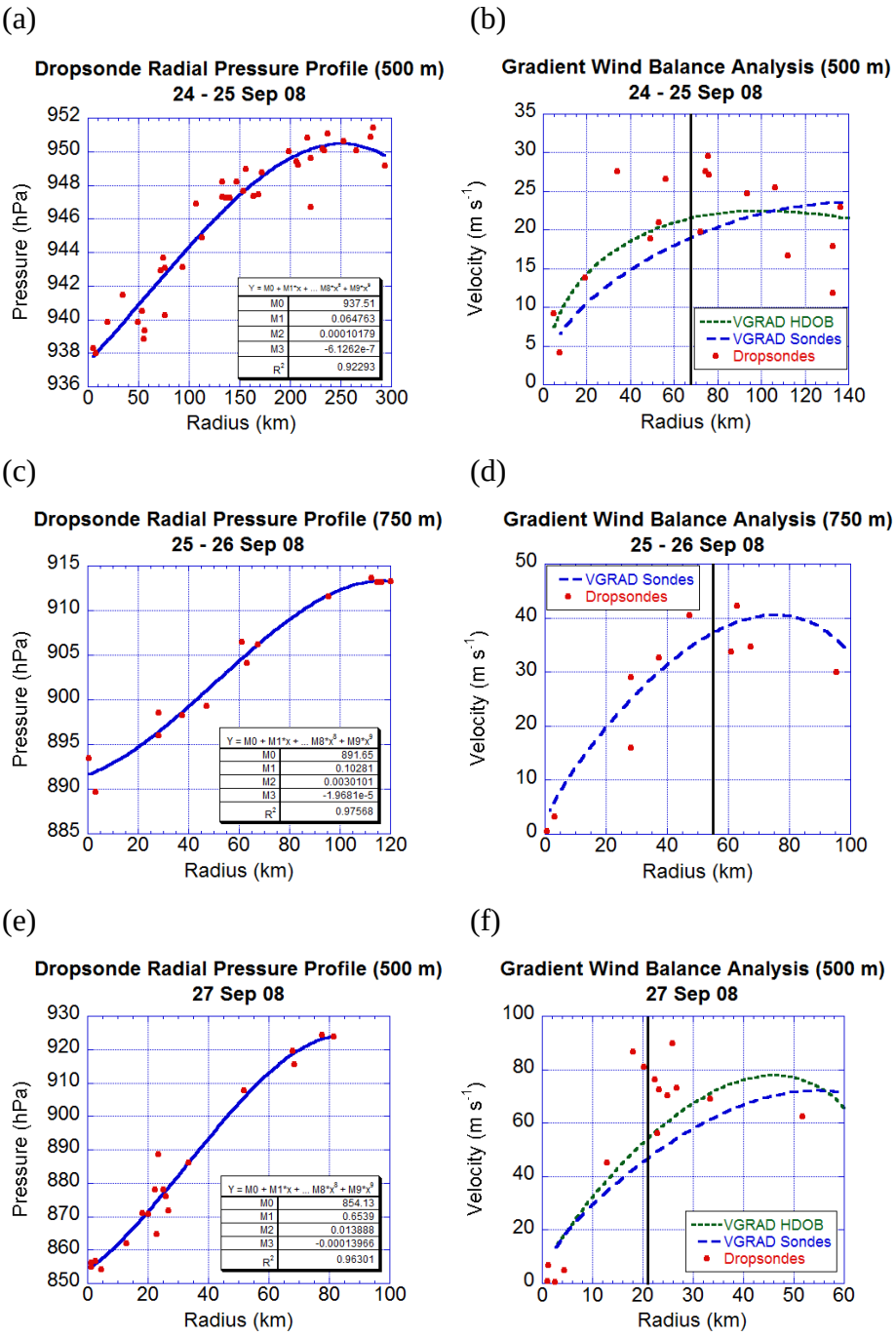

Figure 20. Observed pressure (hPa) from dropsondes (solid red circles) and 3rd degree polynomial fit (solid blue line) at (a) 500 m for TS Jangmi, (c) 750 m for Typhoon Jangmi, and (e) 500 m for Supertyphoon Jangmi. Table shows curve fit coefficients and r^2 values. Tangential wind in m s^{-1} at (b) 500 m for TS Jangmi (d) 750 m for Typhoon Jangmi, and (f) 500 m for Supertyphoon Jangmi from dropsondes (solid red circles) and gradient wind from HDOB data (short-dashed green curve) and dropsonde data (long-dashed blue line). The solid black vertical lines in (a-d) denote the mean RMW.

b. Analysis of Asymmetric Tangential Wind Field

The degree of variability in the tangential wind speed with azimuth raises the possibility that the variability may be an artifact of the locations of dropsonde observations near a similar radius in various quadrants of an asymmetric storm. To investigate this further, an examination was carried out on five dropsonde observations with the most significant supergradient tangential wind speeds (> 26 m s^{-1}) based on the dropsonde-derived gradient wind curve in Figure 20b. Four of these dropsondes are shown in Figure 15a with the letters 'A', 'D', 'E', and 'I'. Dropsonde A was launched at 1935 UTC 24 Sep 08 at a radius of around 78 km and an azimuth of 331° (i.e., southeastern quadrant). Dropsonde E was released at 2306 UTC 24 Sep 08 at a radius of 80 km and an azimuth of 80° (i.e., northeastern quadrant). Dropsonde I was launched at 2345 UTC 24 Sep 08 near a radius of 51 km and an azimuth of 127° (i.e., northwestern quadrant). Dropsonde D was released a couple of hours earlier at 2134 UTC 24 Sep 08 near a radius of 56 km and an azimuth of 282° (i.e., southeastern quadrant). The fifth dropsonde was released at 0004 UTC 25 Sep 08 in the outer eye region in the same quadrant as Dropsonde D near 40 km radius in the southeastern quadrant and at an azimuth of 312° (see Figure 15a).

Dropsonde I and the outer eye dropsonde were both launched during the same radial leg on the airplane's way in and out of the storm center, respectively. During this radial leg, the asymmetry in Tropical Storm Jangmi is evident in satellite imagery that is shown in panels 8 and 9 of Figure 31 in Chapter V, Section B1 and the WC-130J aircraft radar imagery (Figures 59 and 60 in Appendix M). It is clear that the primary convection is located south and east of the center. Dropsonde I is in an area with very little convection, but still recorded a high tangential wind speed of 27 m s-1 (the peak tangential wind in recorded by dropsondes in TS Jangmi was 29 m s^{-1}). The outer-eye dropsonde is near an area of deep convection as observed in the satellite imagery shown in panel 3 of Figure 31 and aircraft radar imagery (Figures 60a,b in Appendix M). This dropsonde recorded a large tangential wind speed of 28 m s^{-1}. Dropsonde D is in the same quadrant as the outer-eye dropsonde, but was released about two and a half hours

earlier. This dropsonde recorded similarly a large tangential wind speed of 28 m s^{-1} despite not being located near deep convection (see Figure 55, Appendix M).

Despite the fact that these five dropsondes were launched in three different quadrants of the storm at varying radii and times, they all recorded approximately the same high tangential wind speeds. Moreover, each of these dropsondes recorded significantly supergradient tangential winds based on the dropsonde-derived mean gradient wind curve and this result appears independent of whether they were launched into areas of deep convection.

c. Does Deep Convection Influence Supergradient Winds?

To assess the impact of deep convection on the finding of supergradient winds in TS Jangmi , an analysis was carried out on the WC-130J radar images 1-2 minutes prior to the splash down of all nine dropsondes that measured significant supergradient winds. A similar analysis was carried out on the radar images at the time of splash down of the dropsondes. The results are shown in Figures 53 - 61 of Appendix M. The radar imagery reveals that only two supergradient wind observations may have been influenced by deep convection, which is indicated by reflectivity values $\geq$ 45 dBZ (Sonde A and Outer-Eye Sonde). Sonde B was near a precipitation area, but it was of a stratiform nature with a large area of reflectivity values $\leq$ 35 dBZ.

This analysis raises some new questions. It is unknown how close a dropsonde must be to convection in order for it to be significantly influenced by the flow induced locally by the convection. Furthermore, how does one meaningfully distinguish between the effects of convection and boundary-layer dynamics on the supergradient wind observation? Lastly, how does one explain the presence of significant supergradient winds in an area completely devoid of convection? It is unclear how to answer these questions, even with a good dataset. Just because a supergradient wind observation is near an area of convection does not necessarily mean it is a result of the convection. It may be, for example, the result of axisymmetric boundary layer dynamics described in Section 2a.

d. An Uncertainty Estimate from a Quadrant-by-Quadrant Analysis

Due to the limitations of the dropsondes and compositing methodology mentioned in the Section 2c, it was decided to perform a rough uncertainty estimate and quadrant-by-quadrant analysis using the more frequent 30 s HDOB extrapolated SLP data despite the drawbacks of this dataset mentioned in Section 2a. The error estimate was computed using the steepest pressure-gradient curve (NE Quadrant; see Figure 51d in Appendix M) and the flattest pressure-gradient curve (WSW Quadrant, Figure 51b in Appendix M) to compute an estimated upper and lower bound of the gradient wind curve. These two curves provide a rough uncertainty estimate due to the asymmetric pressure field observed in TS Jangmi. The upper-bounding curve (NE Quadrant) and the lower-bounding curve (WSW Quadrant) have been placed onto the gradient wind plot in Figure 20b and the result is shown in Figure 21.

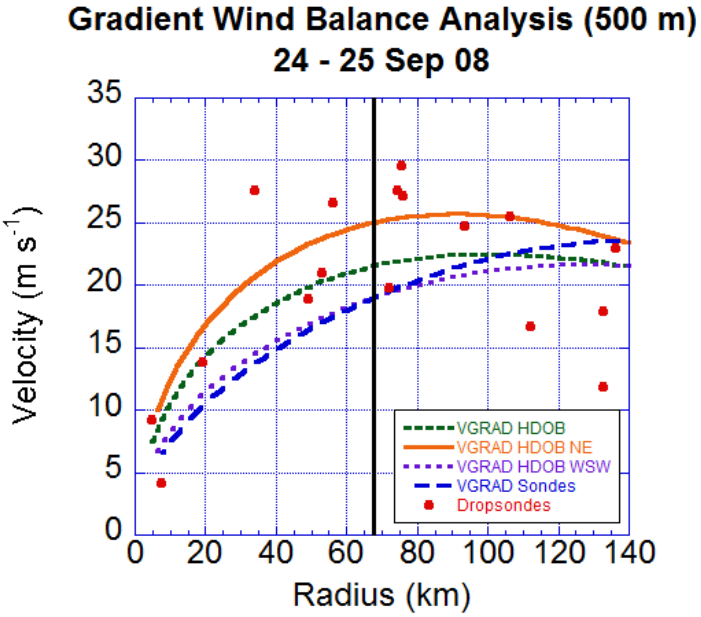

Figure 21. Tangential wind speed in m s^{-1} at 500 m altitude for TS Jangmi from dropsondes (solid red circles) and gradient wind speed in m s^{-1} derived from all flight-level HDOB data (short-dashed green curve), flight-level HDOB data in NE Quadrant (solid orange line), flight-level HDOB data in WSW Quadrant (dotted purple line), and dropsonde data (long-dashed blue line). The solid black vertical line denotes the axisymmetric RMW based on the SFMR data. The NE and WSW quadrant curves were used to plot an upper and lower bound of the gradient wind curve, respectively. The NE Quadrant contained the steepest pressure gradient (see Figure 51d, Appendix M), while the WSW Quadrant had the flattest pressure gradient (see Figure 51b, Appendix M).

The plot in Figure 21 above shows that using the gradient wind curve with the steepest pressure gradient (NE quadrant-solid orange line) still results in five supergradient wind observations near and just within the RMW. Note also that the dropsonde curve is very similar to the gradient wind curve obtained using the flattest pressure gradient (WSW quadrant-dotted purple line). The difference between the upper and lower bound gradient wind curves is approximately 5 m s^{-1} just outside the RMW and then around 6 - 7 m s^{-1} near and just within the RMW. This difference is used to define an uncertainty estimate of ~ $\pm$ 3 m s^{-1} for the gradient wind curve.

The tangential winds are in excess of the mean HDOB-derived gradient wind curve (dashed green line) by 5 - 6 m s^{-1}. Considering the fact that the error bar associated with the asymmetric storm structure is $\pm$ 3 m s^{-1} implies that the tangential winds still exceed the largest HDOB-derived gradient wind speed curve by 2 - 3 m s^{-1}. Recalling that the instrument error of the dropsonde is less than $\pm$ 0.5 m s^{-1} (See Hock and Franklin 1999), implies that the tangential wind is in excess of the largest HDOB-derived gradient wind speed by about 2.5 m s^{-1}.

For the quadrant-by-quadrant gradient wind analysis, the HDOB-extrapolated SLP for each of the six radial legs was used to compute the pressure gradient at the surface. Because of the boundary layer approximation, the radial pressure gradient at the surface was used to estimate the gradient wind curve for each quadrant at an altitude of 500 m. It was assumed also that the radius of curvature was equal to the local radius. Next, using the gradient wind curve, the dropsonde tangential wind observations in the corresponding quadrant were used to diagnose the presence of supergradient winds in the respective quadrant of the storm. The results of this analysis are shown in Figures 49a-l, Appendix M and suggests that there is at least one observation of supergradient winds in each quadrant (ESE-1; WSW-1; SSE-1; NE-1; NW-1; SE-2). Moreover, all seven of the supergradient observations in each quadrant lie above the $\pm$ 3 m s^{-1} error bar estimated previously.

The new results shown in Figures 49a-l of Appendix M and Figure 21 using the HDOB data by quadrant suggest that the supergradient winds in the boundary layer of TS Jangmi may exceed analysis and instrument errors. Thus, based on the

analysis presented, it is clear that that a high density deployment of dropsondes across the RMW is required in each radial leg to validate the HDOB-derived extrapolated sea-level pressure and provide more frequent evidence of whether or not supergradient winds exist in a particular quadrant. In addition, these high density dropsondes would vastly improve the estimates of the asymmetries and their impacts on the compositing technique.

4. Summary

The observational analysis presented in this chapter is consistent with the three-dimensional model simulation results of SMN09, which showed the prevalence of supergradient winds in this region during intensification. SMN09 found in their Experiment 1 (p. 1328, column 1) that the peak amount by which the mean tangential wind speed surpasses its gradient value is 23% at 24 h, 14% at 48 h, and 22% at 72 h. Furthermore, the suggestion of supergradient winds in TS Jangmi, which had a highly asymmetric wind profile (Figure 15b), challenges the findings of Kepert (2006a) that only storms with a "peaked" wind profile can have significant supergradient winds. This disparate result will be discussed in more depth after the discussion of gradient wind balance for Hurricane Georges in Chapter IV, Section B1.

This study appears to present the first finding of supergradient tangential winds in the boundary layer of an intensifying tropical storm. However, the limitations of the data due to asymmetries and the compositing technique does not allow for a strongly conclusive statement. Nevertheless, as discussed above, one can still define an azimuthally-averaged gradient wind for the study of spin-up of the mean tangential wind in tropical cyclones, such as Jangmi. The overall axisymmetric gradient wind analyses for Jangmi supports the hypothesis that supergradient winds exist in the boundary layer near and just within the RMW during much of the spin-up of Jangmi. *However, upon considering all of the caveats involved with the symmetric gradient wind calculations, it is clear that a dense deployment of dropwindsondes across the RMW in each radial leg will be necessary to resolve the pressure gradient with sufficient accuracy to validate whether or not supergradient winds exist at the tropical storm stage generally.*

5. Kinematic Composites

The azimuthal composites of tangential and radial winds for all three stages of Jangmi are shown in Figure 22 in the eye, eyewall, outer core, and ambient regions of the storm. The eye and eyewall regions are estimated using radar, satellite imagery, and dropsonde data. The outer core is defined as in Chapter I, Section C2 (~ twice the RMW to the radius of ~ 17 m s^{-1} total wind speeds). The ambient (i.e., environment) region covers the region outside of the outer core to a distance of approximately 800 km. In all three stages, there is radial inflow present from the surface to an altitude of at least 1 km. The peak azimuthally-averaged tangential wind speeds are observed at an altitude of around 500 m in TS Jangmi, nearly 550 m in Supertyphoon Jangmi and about 650 m in Typhoon Jangmi, which are elevations well within the inner-core dynamical boundary layer. The maximum tangential winds are located at an altitude where the radial inflow is between 2 m s^{-1} and 10 m s^{-1}. These results agree well with the observational results of (Franklin et al. 2003; Powell et al.; 2003; Giammanco et al. 2008) and the numerical-model results of (Kepert 2001; Kepert and Wang 2001), which found also that the maximum wind speeds occurred at a height of around 500 m; however, these authors failed to make the connection between the location of the peak wind and the boundary layer. However, this finding is in conflict with both Emanuel's and Ooyama's theory of spin-up, which posit that the peak tangential wind is located at the top of the boundary layer or just above it, respectively.

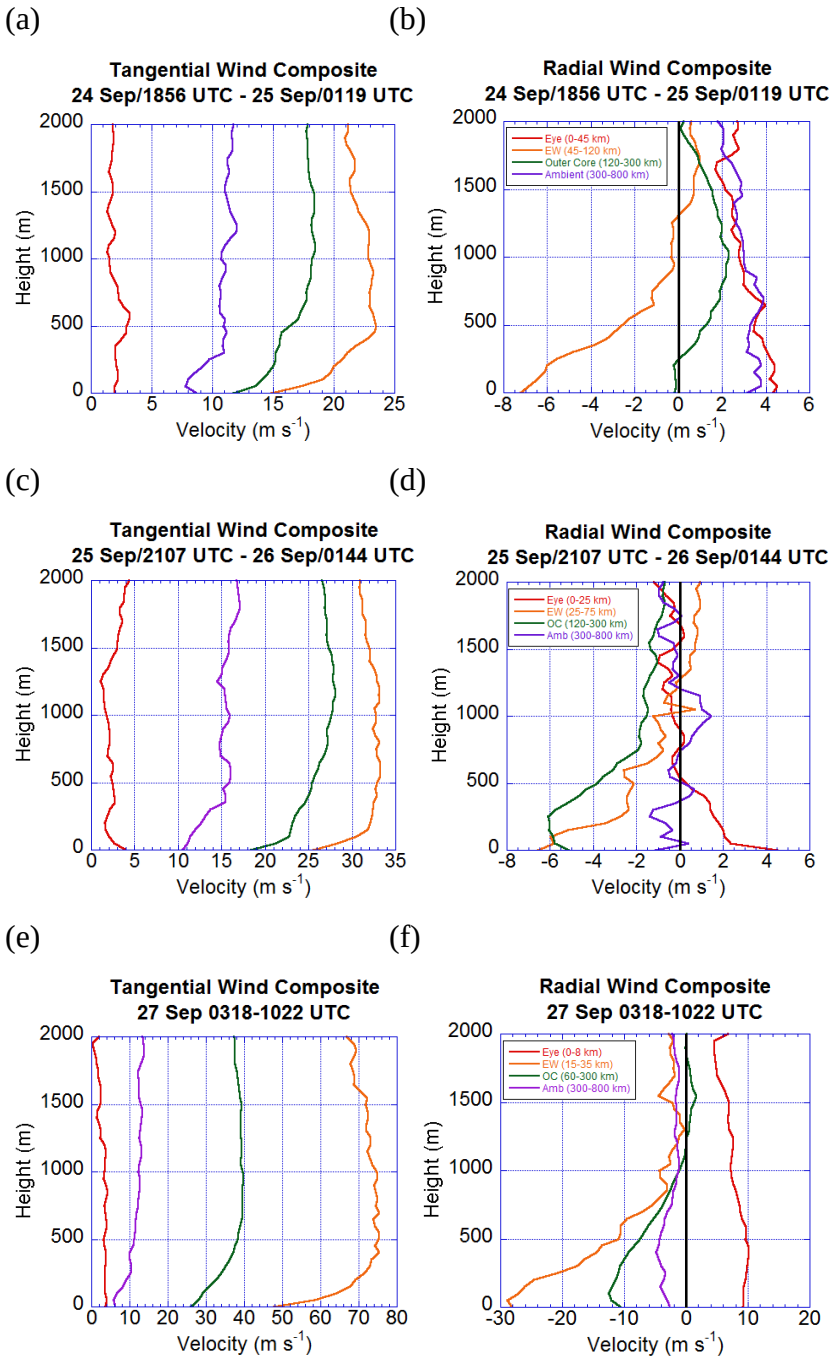

Figure 22. Low-level (0 - 2 km) tangential wind speed (m s^{-1}) in left column and radial wind speed (m s^{-1}) in right column composite soundings for (a,b) TS Jangmi, (c,d) TY Jangmi, and (e,f) STY Jangmi in the eye (red line),eyewall (EW; orange line), outer core (OC; green line), and ambient (Amb; purple line) regions of storm.

6. Thermodynamic vs. Dynamic Boundary Layer

A comparison of the thermodynamic and dynamic boundary layer during the evolution of Jangmi is shown in Figure 23. The composite profiles of tangential wind speed (VT), radial wind speed (VR), virtual potential temperature (VPOT), and potential temperature (PT) are plotted to provide a more in-depth picture of both boundary layers and the location of the peak tangential wind component in relation to them. In addition, the depth of the low-level significant radial inflow layer (≥20% of near-surface value) is shown with the solid black horizontal line labeled "Inflow," and the height of the peak tangential wind speed is depicted with a solid black horizontal line labeled "VT Max." The dynamic boundary-layer top is denoted by the solid black horizontal line labeled "GWB," while the thermodynamic boundary-layer top is depicted by the solid horizontal line labeled "TD."

This comparison reveals that during the intensification of Jangmi, the dynamical boundary layer is located at a much higher altitude than the well-mixed thermodynamic boundary layer. On average, the inner-core boundary layer is approximately 1.4 km above the thermodynamic boundary layer. In addition, on all three days the average maximum tangential wind component resides well within the inner-core dynamical boundary layer. Thus, *it is clear that the spin-up of Jangmi is occurring within the boundary layer in the region near and just inside of the RMW.*

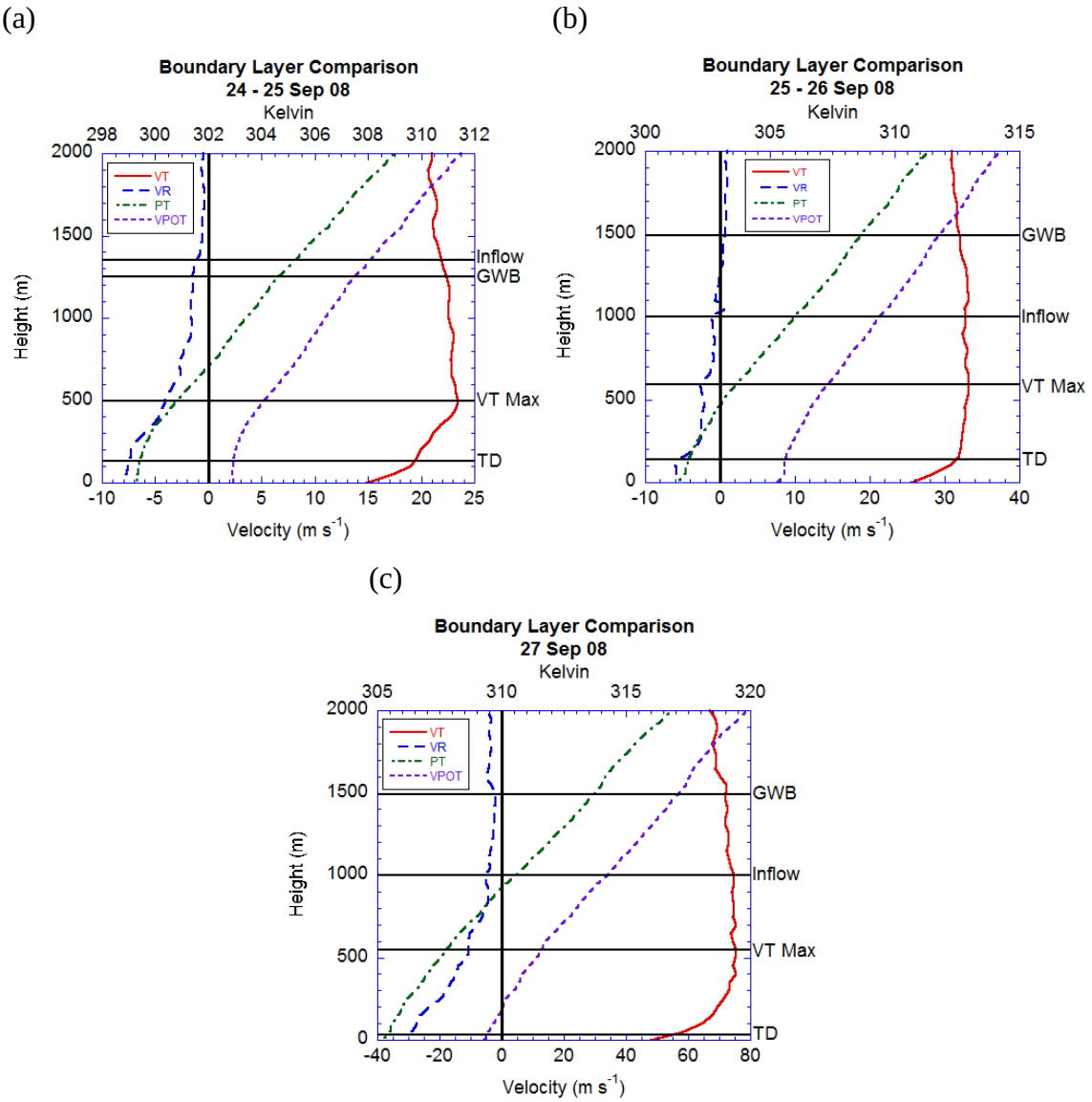

Figure 23. Boundary-layer height comparison for (a) TS Jangmi, (b) TY Jangmi, and (c) STY Jangmi using thermodynamic and dynamic definitions. Dynamic boundary layer (layer of significant gradient wind imbalance) depth depicted by solid horizontal black line labeled "GWB"; layer of significant radial inflow (≥ 20% of near-surface value) shown by solid horizontal black line marked "Inflow"; thermodynamic boundary layer (well-mixed) displayed with solid horizontal black line labeled "TD." The height of maximum tangential wind speed depicted with solid horizontal black line labeled "VT Max." Tangential wind speed composite (solid red line), radial wind speed composite (dashed blue line), potential temperature composite (dotted-dashed green line), and virtual potential temperature (small dashed purple line) are plotted on graph.

7. Individual Eyewall Dropsondes

Since the kinematic composites shown in Figure 22 are based on 28 eyewall dropsondes, it is of interest to study the individual dropsondes released in this region (see Figure 42 in Appendix F; Figure 43 in Appendix G; and Figure 44 in Appendix H). A majority of the radial wind profiles of these sondes during the evolution of Jangmi contain a radial inflow from the surface to between 600 m and 1000 m altitude. The peak tangential wind speed in 26 of the 28 sondes occurred *within* the boundary layer. Furthermore, 23 of the 28 sondes had the maximum tangential wind speed at or below an altitude of 600 m. Indeed, several profiles had peak tangential winds between 100 m and 300 m above the sea surface.

In Supertyphoon Jangmi, three dropsondes were launched about one-minute apart between 0920 and 0922 UTC 27 September over a distance of 9 km in the left-rear quadrant of the inner eyewall (region nearest to eye) to measure the tangential wind speed radial gradient in this region. This "triple-eyewall" sequence consisted of launching dropsondes consecutively at the location of the flight-level maximum wind, the peak surface wind, and then approximately one-minute after the surface peak wind (P. G. Black 2008, personal communication). The triple eyewall soundings indicated that over a distance of ~ 5 km, the peak tangential wind speeds near the surface increased from 54 m s^{-1} in the outer eye to 89 m s^{-1} in the eyewall. The peak tangential wind speed in the outer-eye dropsonde was observed at an extremely low altitude of 74 m (Figure 24). Moreover, the outer-eye dropsonde indicated significant radial inflow of 14 m s^{-1}.

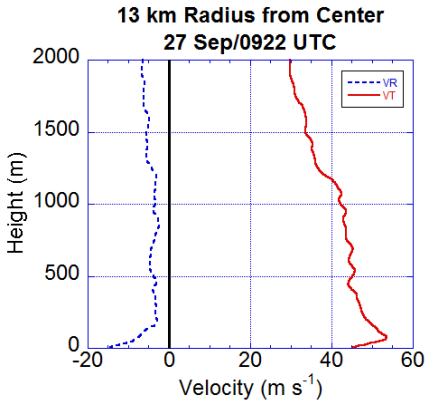

Figure 24. Tangential wind (solid red line) and radial wind (dotted blue line) profile in units of m s^{-1} for the "outer eye" dropsonde released at 0922 UTC 27 September 2008. Note the peak wind at a very low level (~ 74 m) within the layer of strong radial inflow.

In summary, the individual and composite radial and tangential wind profiles in the eyewall of Jangmi show again that *the maximum tangential wind speeds occur largely within the boundary layer*.

B. HURRICANE GEORGES INNER-CORE STRUCTURE: 19–20 SEPTEMBER 1998

The approximately axisymmetric inner-core structure of Georges in the radial and vertical plane was conducted using flight-level data and 27 eye and eyewall dropsondes released from four aircraft (two NOAA WP-3Ds and two USAFR WC-130) flying at varying altitudes. The arc-like dropsonde paths and multiple aircraft radial penetrations in Figure 25a reveal the data coverage between 1706 UTC 19 September and 0816 UTC 20 September. The radial and vertical coverage of the data points (over two-thirds from dropsondes) taken during this time are shown in Figure 25b. There was enough coverage in the inner-core region to provide confidence in the calculated axisymmetric features.

A total of 18 eyewall and nine eye dropsondes were used for the study of Hurricane Georges' inner-core boundary-layer structure. Two eyewall dropsondes from 1718 UTC 19 September and 0801 UTC 20 September included in this study were not used in Kepert's 2006a study of the same storm. It appears that Kepert did not use these two dropsondes because the former had missing data in the middle of the profile, and the

latter was nearly seven hours after the previous eyewall dropsonde launch. While this is a good reason to omit these two dropsondes, they were used here since their profiles were similar to the previous dropsondes, the missing data were only between 1000 m and 1700 m, and the storm was in a near steady-state condition. This steady-state condition (storm at or near peak intensity with approximately axisymmetric structure) was verified by wind and pressure data from dropsondes and satellite imagery during the period of analysis. In addition, an outer-eye dropsonde at 0616 UTC 20 September was used that was not previously analyzed by Kepert(2006a).

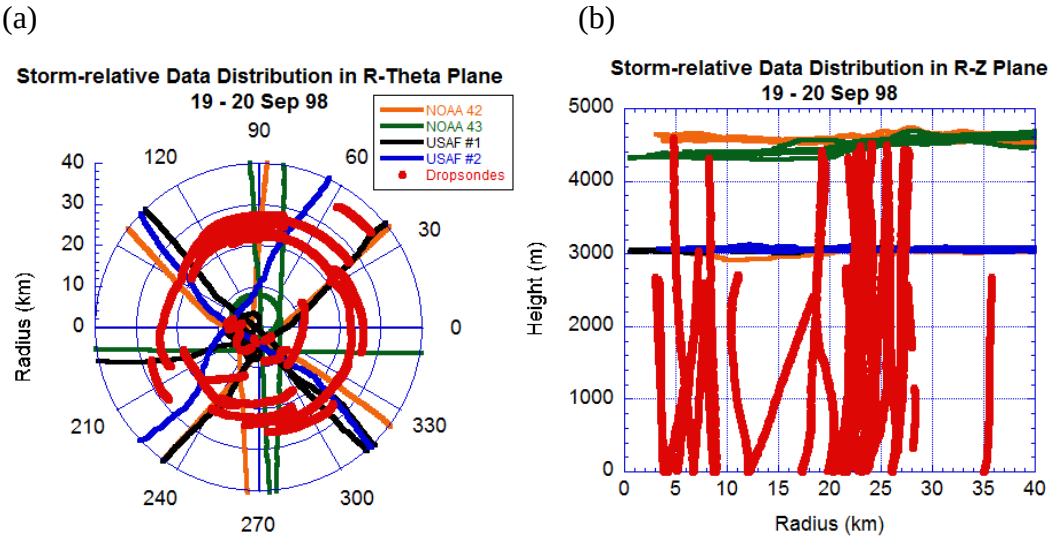

Figure 25. Dropsonde locations, trajectories, aircraft flight tracks relative to Hurricane Georges center from 1706 UTC 19 September to 0801 UTC 20 September 1998. Storm-relative data distribution in (a) radius-azimuthal (R-θ) plane, (b) radius-height (R-Z) plane. NOAA P-3 (42 in orange, 43 in green), and USAFR WC-130 (#1 in black, #2 in blue) flight tracks, and GPS dropsonde trajectories (in red). Dropsondes move cyclonically (counterclockwise) in (a).

The locations of the 18 eyewall dropsondes from Hurricane Georges are depicted in Figure 26a in storm-relative coordinates. The tangential wind speed with respect to radius at an altitude of 750 m is plotted in Figure 26b. This altitude was chosen since it is the approximate location of the azimuthal eyewall average peak tangential wind speed. The RMW at ~ 22 km had a peak tangential wind speed of ~ 84 m s^{-1}. A dropsonde observation in the outer region of the eyewall indicates that the tangential winds may have decreased rapidly outside a radius of around 30 km; however, this is uncertain since

there is a large gap and variability in dropsonde observations. Just beyond a radius of 60 km, the winds maintain a speed of approximately 38 m s^{-1} with two peaks of 45 m s^{-1} at radii of 67 km and 80 km. Moreover, hurricane-force winds extended out to around 100 km, and tropical-storm force winds extended out to around 270 km (not shown).

(a) (b)

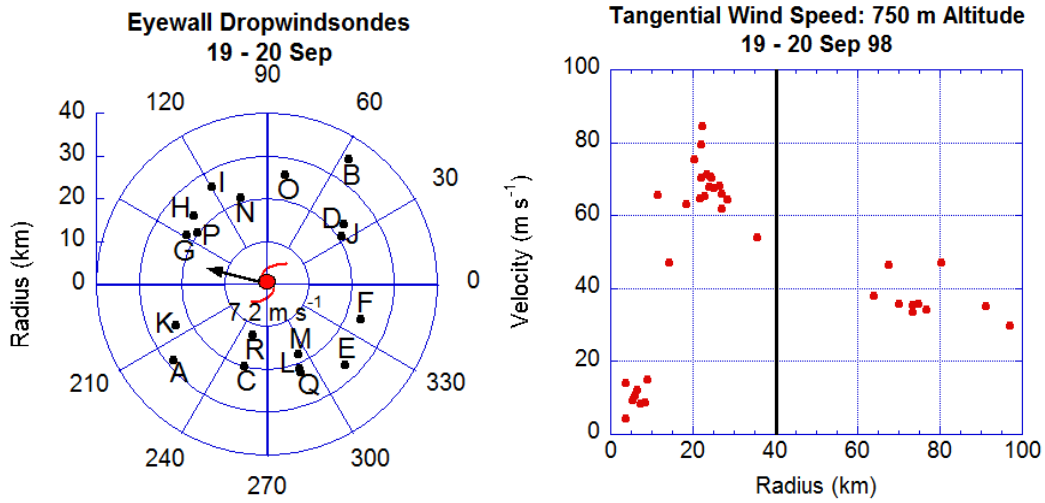

Figure 26. (a) Near-surface radius versus azimuth display of *only eyewall dropsondes* in geographic-oriented coordinates; dropsondes are listed in order of launch via letters (A-R) from 1706 UTC 19 September to 0801 UTC 20 September 1998. (b) Tangential wind velocity (m s^{-1}) versus radius at an altitude of around 750 m out to 100 km from dropsondes (red dots) during missions into Hurricane Georges from 1706 UTC 19 September to 0801 UTC 20 September 1998.. Storm motion shown with black arrow in center of (a). Storm translation speed was 7.2 m s^{-1}. Vertical black line shows start of inner core.

1. Gradient Wind Balance Analysis

A similar investigation as in Jangmi as to whether or not supergradient winds were present during the spin-up of Georges is carried out at six altitudes: 275 m, 500 m, 750 m, 1000 m, 1250 m, and 1500 m. No HDOB flight-level extrapolated sea-level pressure observations were available to compute a second radial pressure gradient.

The pressure curve fits were judged appropriate since the r^2 values were between 0.81 and 0.84 (Figure 26a and Figures 45a,c,e,g,i in Appendix I). However, there is an anomalously high pressure observation near a radius of 12 km from a dropsonde that was

released at 0616 UTC 20 September (not shown) in the right-rear quadrant. This dropsonde had a peak tangential wind speed of 74 m s^{-1} at ~ 350 m. With the exception of this anomalous value, a third-degree polynomial pressure fit provides a reasonable fit to the dropsonde pressure observations that was used to compute the gradient wind speed in Georges at each of the six altitudes.

The gradient wind balance analysis in Georges strongly suggests the prevalence of significant supergradient winds near and just within the RMW at all six altitudes with an average of ~ 28% (Figure 27b and Figures 45b,d,f,h,j in Appendix I). All of the strong supergradient winds of 20% or higher occur near or just within the RMW, while the weak supergradient winds are confined primarily outside the RMW. Subgradient winds are found at all altitudes just beyond the eyewall at ~ 36 km radius. These results are very similar to those found in Supertyphoon Jangmi.

Based on the gradient wind analysis above and the definition of the inner-core boundary layer in Chapter II, Section B5, the boundary-layer depth for Hurricane Georges is estimated to be at least 1500 m. This depth will be used now to study inner-core spin-up using the kinematic composites of radial and tangential wind in the next section.

a) (b)

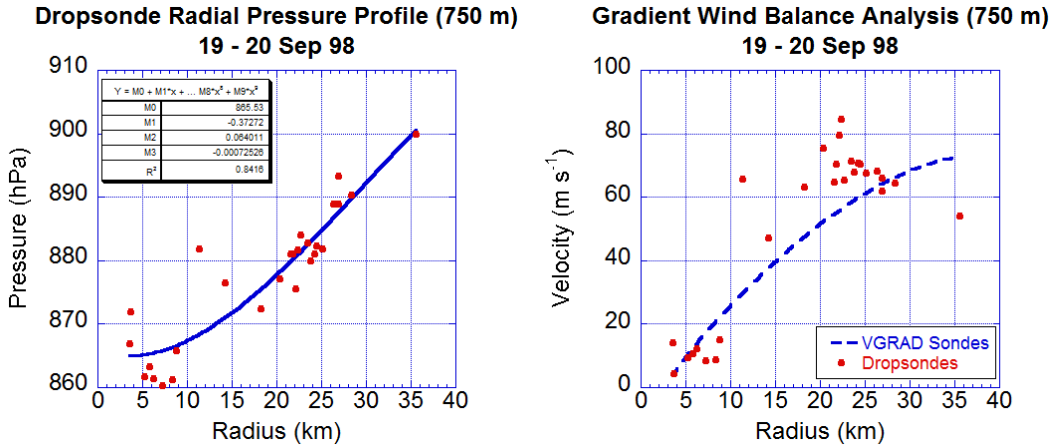

Figure 27. (a) Observed pressure (hPa) at 750 m from dropsondes (solid red circles) and 3rd degree polynomial fit (solid blue line) from 1706 UTC 19 September to 0801 UTC 20 September 1998. Table shows curve fit coefficients and r^2 value. (b) Observed tangential wind in m s^{-1} at 750 m from 1706 UTC 19 September to 0801 UTC 20 September 1998 from dropsondes (solid red circles) with gradient wind based on dropsonde data (dotted blue line).

The supergradient winds in the inner core of Hurricane Georges found here are at odds with the results of Kepert (2006a; hereafter K06a), who found subgradient and weakly supergradient winds in his study. K06a stated that:

> This weak supergradient flow is in contrast to the case considered in KW01, and is due to the particular angular momentum distribution in Georges, with a relatively slow decrease of wind speed outside the inner core and a minimum in the radial gradient of absolute angular momentum immediately outside of the RMW.

In contrast to Georges, Kepert (2006b) did find significant supergradient winds in Hurricane Mitch (1998), which had a much sharper decrease of the tangential winds outside the RMW. The numerical simulations of Kepert and Wang (2001; hereafter KW01) had a tropical cyclone with a "peaked" wind profile similar to Mitch that had a narrow region of significant supergradient flow at the RMW, with little, if any, supergradient winds outside of this region. KW01 argued that the "peaked" profile (their Figure 7) is much more effective at converging angular momentum toward the storm center in contrast to the "flat" profile (their Figure 3). They showed that a storm with a "flat" wind profile, which contained a broader area of angular momentum, led to the

development of a wide region of weaker supergradient winds. Since the gradient wind analysis presented in Sections A1 and B1 of this chapter suggest that significant supergradient winds are present during all three stages of spin-up for Supertyphoon Jangmi and the steady-state condition of Hurricane Georges, it is argued that the "peaked" radial wind profile of tangential winds as noted by KW01 is not a necessary condition for the existence of significant supergradient winds in tropical cyclones.

For the case of Georges, the tangential wind versus radius plot derived from the dropsonde data (see Figure 26b) reveals that the gradual reduction of tangential wind speed with increasing radius occurs between two to three times the RMW (40 – 60 km), after a steep fall-off immediately outside the RMW. These characteristics resemble the "peaked" profile of KW01. Thus, Georges is considered to have had a combination of a "peaked" profile immediately beyond the RMW, and a "flat" profile farther out in the region two to three times the RMW. It seems that Kepert based his interpretation of the tangential wind profile for Georges solely on a model simulation of the boundary-layer flow instead of using the actual dropsonde data, which may have led to a smoothing out of the profile and a misinterpretation of the situation. Additionally, he seems to have overlooked the possibility that a storm could have a combination of a flat and peaked profile and instead focused primarily on the outer core. Kepert's argument that a "peaked" profile is necessary for significant supergradient winds is questionable, since he uses an inertial stability argument based on the profile of M outside of the RMW and *above* the boundary layer to explain the lack of supergradient winds in Georges[2].However, the inertial stability concept *does not* apply to the boundary layer. Within this thin layer, the flow is dominated by the impact of frictional effects, which, outside a given radius guarantee that the agradient force is inward, regardless of the amount of inertial stability (Smith et al. 2011). As a result, due to the effects of friction, there is no inertial resistance to radial displacements within the boundary layer.

As to the representativeness of the tangential wind profile of Georges for major hurricanes, it proves useful to compare the Georges wind profile against the "Major

[2]The idea of inertial stability is usually appropriate for an instance in which a swirling flow in gradient wind balance with zero radial motion is symmetrically disturbed (Rayleigh 1916).

Hurricane" profiles from Mallen et al. (2005, their Figure 11a). These profiles are derived from 5,124 radial legs of flight-level data from 644 missions into 72 storms in the Atlantic and Northeastern Pacific between 1977 and 2001. The profiles for "Pre-hurricane" (their Figure 7) and "Hurricane" stage (their Figure 9) were similar to the "flat" profile of KW01. Since most, if not all, tropical storm and minimal hurricanes lack a "peaked" profile of tangential winds versus radius, this naturally leads to the question of whether or not supergradient winds are observed during the tropical storm or minimal hurricane stage. Given favorable conditions, it is during these stages of the tropical cyclone life cycle that the storm is most likely to be undergoing spin-up given favorable environmental conditions (i.e., SST > 26° C, little vertical wind shear, high ocean heat content, moist mid-levels). The SMN09 model results showed that tropical cyclone inner-core spin-up hinges on enhanced convergence of angular momentum within the boundary layer via the agradient radial force due to surface friction. Their finding suggests that supergradient winds should indeed be present in these earlier and less intense stages.

Finally, the lack of significant supergradient winds in Kepert's work may have been in part a result of him using an empirical, parabolic profile from Willoughby et al. (2006) to derive the gradient wind profile instead of directly using dropsonde observations. Kepert offered the following logic for using this technique:

> The data are relatively few and are unevenly distributed in space, so it was decided to fit the Willoughby et al. (2006) parametric profile (henceforth WDR profile) to the data, rather than analyzing to some grid. The WDR profile was designed specifically to accurately fit wind observations, and has been extensively tested on aircraft data.

In the same paper, Kepert noted that it is possible, but highly doubtful, that the lack of supergradient winds in Georges is a result of his analysis technique. However, he admits that due to the sparse amount of data and uneven distribution in the radial direction, the possibility of errors contributing to an incorrect pressure gradient is not eliminated.

Another possible reason for the absence of supergradient winds in Kepert's analysis for Georges is that he calculated the gradient wind speed curve separately for two different periods of observation (i.e., early and late). The early period refers to ~

1700 – 2100 UTC 19 September, while the late period covers ~ 0000 – 0130 UTC 20 September. After finding significant supergradient winds using a gradient wind balance curve covering both the early and late periods (his Figure 16b), K06a stated:

> The pressure profile clearly fits the observations well, and analysis of the residuals shows that both the 15–40 km and 60–100 km bands are uncorrelated with radius, so the gradients in these bands are accurately estimated… However, it is clear that the pressure near the RMW rose between the early and late periods as the RMW contracted, and that the residuals from each period (considered separately) are correlated with radius, so the fitted curve underestimates the radial pressure gradient in both periods, and the apparent supergradient flow near the RMW is spurious. Thus, it is necessary to consider the periods separately.

The separate calculations for the early and late periods resulted in a higher gradient wind speed curve and much weaker supergradient winds.

Kepert's finding of significant supergradient winds using a blend of the early and late period data (his Figure 16b) is similar to the gradient wind balance results in Georges shown in Figure 27b and Figures 45b,d,f,h,j in Appendix I. A comparison of Kepert's radial pressure profile at 500 m (his Figure 16a) with Figure 45c in Appendix I reveals a similar radial pressure gradient, with Kepert's being slightly higher. However, the pressure observations fit the polynomial curve in Figure 26b well. Finally, during this entire observation period, Georges was in an approximate steady-state. On the basis of the foregoing considerations, it is reasonable to combine the dropsonde observations from the two periods to derive the gradient wind curve.

In summary, the lack of supergradient winds found in Kepert's study of Georges is due to his use of a Willoughby et al. (2006) parabolic profile to derive the gradient wind profile instead of directly using dropsonde observations. Another factor was that he computed the gradient wind curve for two separate periods of dropsonde observations during Georges' near steady-state condition. Additionally, it was shown that the "peaked" radial wind profile of tangential winds as noted by KW01 is not a necessary condition for the existence of supergradient winds in tropical cyclones. Finally, it was argued that Kepert incorrectly explained an absence of supergradient winds in Georges

using an inertial stability argument based on the profile of absolute angular momentum outside of the RMW and *above* the boundary layer.

2. Kinematic Composites

The azimuthal composites of the low-level ($0 < z < 2$ km) radial and tangential winds in the eye ($0 < r < 10$ km), eyewall ($15 < r < 40$ km), the outer core ($60 < r < 300$ km), and the storm environment ($300 < r < 800$ km) of Hurricane Georges are displayed in Figures 28a,b. The peak radial inflow of 27 m s^{-1} was between an altitude of 50 m and 100 m. The inflow decreased rapidly to 4 m s^{-1} at a height of approximately 800 m, and then decreases more slowly to around 3 m s^{-1} near a height of 950 m before approaching zero just above 1000 m altitude (Figure 28b). The vertical profile of radial wind in the region of Georges' eyewall is nearly identical to that of Hurricane Isabel in M06b (Figure 29b).

(a) (b)

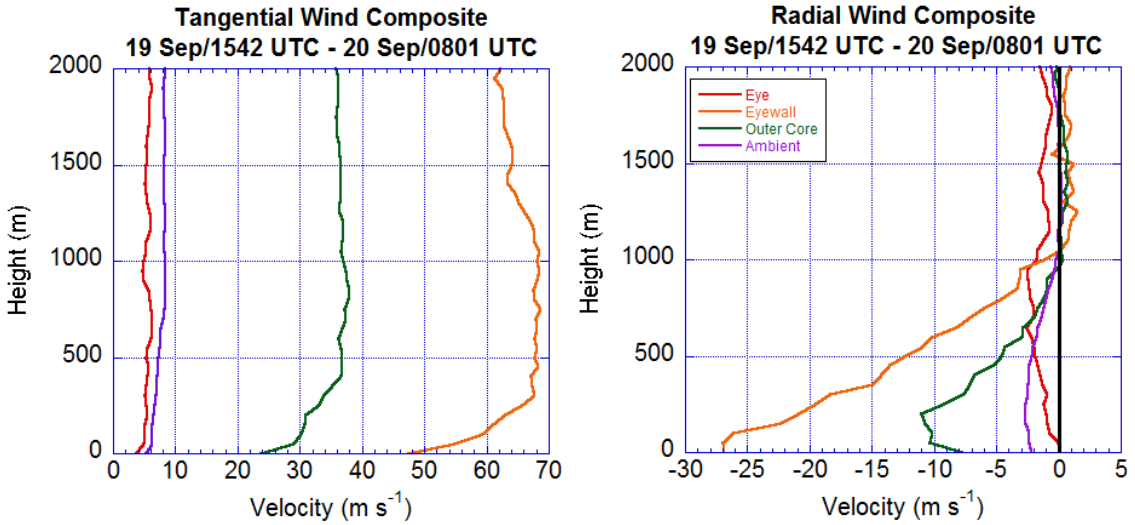

Figure 28. Low-level (0 - 2 km) composite of (a) tangential wind and (b) radial wind from dropsonde observations for eye (0 - 10 km radius, solid red line), approximate eyewall (15 – 40 km radius, solid orange line), outer core (60 – 300 km radius, solid green line), and ambient (300 – 800 km radius, solid purple line) from 1542 UTC 19 Sep- 0801 UTC 20 Sep 1998. The winds are in units of m s^{-1}.

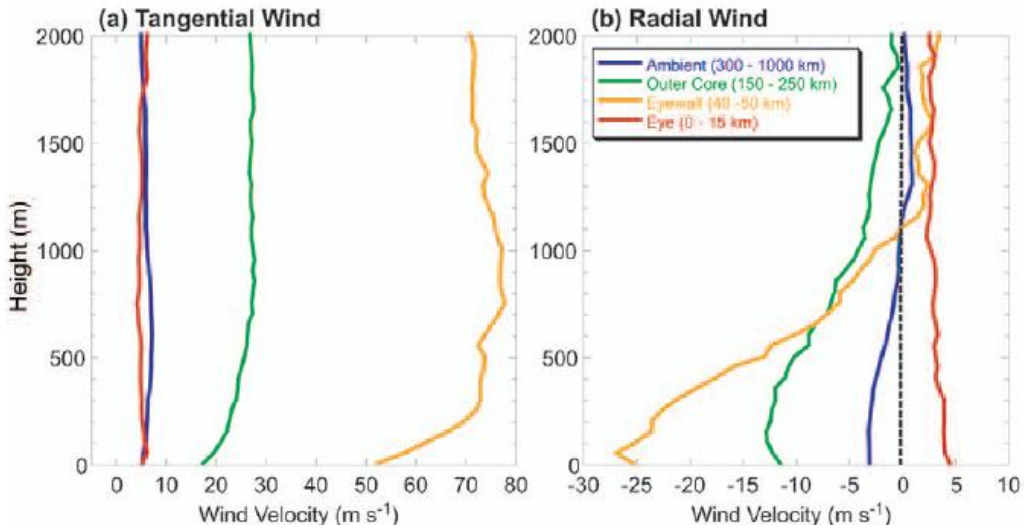

Figure 29. Low-level (0 - 2 km) composite sounding of (a) tangential wind and (b) radial wind from dropsonde observations for the eye (0 - 15 km radius, solid red line), approximate eyewall (40 – 50 km radius, solid orange line), outer core (150 – 250 km radius, solid green line), and ambient (250 – 800 km radius, solid blue line) for Hurricane Isabel during 1600 - 2300 UTC 13 Sep 1998. Winds are plotted in units of m s^{-1}. From M06b Figures 4a,b.

The maximum azimuthally-averaged tangential wind speed of 69 m s^{-1} in Figure 28a is located around 750 m above the surface, which is well within the dynamical boundary layer defined at the end of Section B1. Tangential wind speeds of approximately 67 m s^{-1} - 68 m s^{-1} extend deep into the strong inflow layer stretching between 300 m to 1200 m. Similarly, the results of M06b show that the peak azimuthally-averaged tangential wind speed of 76 m s^{-1} in Hurricane Isabel occurred at a height of around 725 m (Figure 29a). The tangential wind speeds in Isabel of ~72 m s^{-1} between 300 and 1200 m altitude are close to the peak observed at 725 m altitude. However, M06b did not discuss the impact of their results concerning spin-up in the boundary layer. The kinematic composites shown in Figures 28a,b indicate *that the maximum tangential wind speed occurs within the boundary layer of Hurricane Georges near and just within the RMW.*

3. Thermodynamic Vs. Dynamic Boundary Layer

A comparison of the thermodynamic and dynamic boundary layer in Hurricane Georges is shown in Figure 30. This comparison reveals that the inner-core boundary

layer is much larger (~ 1500 m) than the well-mixed thermodynamic boundary layer (~ 125 m). Furthermore, the radial inflow layer has a depth of 950 m. These results are consistent with those found in Supertyphoon Jangmi.

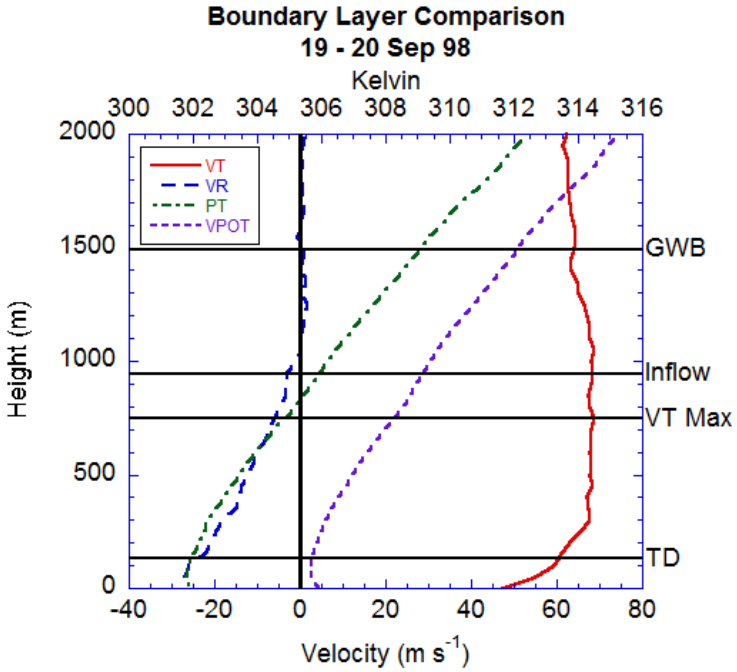

Figure 30. Boundary layer height comparison for Hurricane Georges using thermodynamic and dynamic definitions. Dynamical boundary layer (layer of significant gradient wind imbalance) depth depicted by solid horizontal black line labeled "GWB"; layer of significant radial inflow (≥ 20% of near-surface value) shown by solid horizontal black line marked "Inflow"; thermodynamic boundary layer (well-mixed) displayed with solid horizontal black line labeled "TD." The height of maximum tangential wind speed depicted with solid horizontal black line labeled "VT Max." Tangential wind speed composite (solid red line), radial wind speed composite (dashed blue line), potential temperature composite (dotted-dashed green line), and virtual potential temperature (small dashed purple line) are plotted on graph.

4. Individual Eyewall Dropsondes

Vertical profiles of storm-relative radial and tangential wind speed for the 18 dropsondes released in the eyewall region are shown in Figure 46 in Appendix J. Of these, only one did not have a significant amount of radial inflow (> 5 m s^{-1}) up to at least 600 m. The peak tangential wind speed in all these dropsondes occurred *within* the boundary layer. Furthermore, 10 of the dropsondes had the maximum tangential wind

speed at or below an altitude of 500 m. Two dropsondes labeled "N" and "D" had peak tangential wind speeds at altitudes of 343 m and 300 m, respectively. All of the dropsondes had the peak storm-relative tangential wind speeds at or below 1000 m altitude. Therefore, the individual tangential wind profiles for each of the dropsondes released in the eyewall of Hurricane Georges show clearly that *the maximum tangential wind speeds occurred within the boundary layer.*

Since these analyses of the tangential and radial wind profiles in the eyewall of Georges are virtually indistinguishable from those of K06a (his Figures 7 and 8), it is a validation of the correctness of this analysis methodology to calculate the kinematic properties.

C. SUMMARY OF KEY FINDINGS

The inner-core dropsondes for quasi-steady state Hurricane Georges and rapidly intensifying Supertyphoon Jangmi strongly suggests that tropical cyclone spin-up occurs within the dynamical boundary layer and supports for the first time the notion that significant supergradient winds are prevalent near and just within the RMW during intensification. Although the results for TS Jangmi are not strongly conclusive, the observations do offer support of the new spin-up theory that supergradient winds are present near and just within the RMW during intensification.

According to SMN09, this spin-up process consists of increased convergence of absolute angular momentum within the inner-core boundary layer, which helps converge rings of air parcels farther and faster inward toward the vortex center. Although absolute angular momentum is not materially conserved in the boundary layer, high tangential wind speeds can be achieved if the radial inflow is large enough to bring the air parcels to small radii with minimal loss of angular momentum. This spin-up mechanism is tied fundamentally to the dynamics of the boundary layer, where the flow is not in gradient wind balance.

The next chapter will perform an analysis of deep convection during the spin-up of Hurricane Georges and Supertyphoon Jangmi using the definitions and techniques described in Chapter III, Section H.

PAGE LEFT INTENTIONALLY BLANK

V. ASYMMETRIC VIEW OF TROPICAL CYCLONE SPIN-UP

A. BACKGROUND

Recent research by Montgomery et al. (2006a) and Wissmeier and Smith (2011) has noted that low-level vorticity stretching by growing convection increases the ambient rotation by more than one order of magnitude and that the vorticity remains for a long time after the initial updraft has decayed. The predicted vorticity levels are comparable with those observed in recent research on tropical depressions. One of the main findings in Wissmeier and Smith (2011) was that even moderate convection could lead to a larger amplification of the ambient vorticity than the deep convection. Thus, one should focus not only on the deep convection, but consider also the less intense convection in the aggregate.

A preponderance of deep convective cells (> 14 km altitude) with infrared cloud-top temperatures of ≤-65°C was observed during the spin-up of both Supertyphoon Jangmi and Hurricane Georges. A brief investigation of this convective activity is carried out below to enable a quantitative assessment of the characteristics of some updrafts in TS Jangmi using results from the ELDORA mesoscale analysis of cells that were underneath extremely low cloud-top temperatures of ≤-65°C. This analysis will be used to test Hypothesis #2: *Rotating deep convective cells occur frequently during spin-up of Supertyphoon Jangmi and Hurricane Georges, which confirms recent theoretical studies that rotating deep convective cells are predominant during intensification.* The following observations will be used to test H2: (i) one or more instances of rotating deep convection is captured by ELDORA data underneath areas of overshooting tops and/or sufficiently low cloud-top temperatures (≤ -65°C);and (ii) similar convective activity is witnessed in infrared satellite imagery throughout the spin-up phase. Thus, this analysis of convection in association with the ELDORA results in TS Jangmi and recent theoretical work of NSM08, Shin and Smith (2008), and BMSP09 will allow an inference to be made on whether or not rotating deep convection is present underneath extremely cold cloud-top temperatures during the spin-up of Jangmi and Georges. Although previous work has

long suggested the importance of deep convection to tropical cyclone spin-up, this analysis views it for the first time in light of the new spin-up theory.

B. ANALYSIS OF DEEP CONVECTION

1. Supertyphoon Jangmi

The evolution of deep convective cells during the spin-up of Jangmi is shown using satellite imagery in Figures 31 and 32 during the tropical storm stage. Between 2030 UTC 24 September and 0257 UTC 25 September, two major convective bursts commenced at 2030 UTC 24 September (Panels 1-7 in Figure 31 and Panels 1-5 in Figure 32) and 2330 UTC 24 September (Panels 8-12 in Figure 31 and Panels 6-12 in Figure 32). These bursts consisted of development of cells and their associated anvil clouds near the center of TS Jangmi with extremely low cloud-top temperatures of $< -85°C$. Throughout this period, the cells and anvil clouds continuously spread in coverage and merged into one large cloud region of extremely cold cloud tops covering a horizontal area of around 46,000 km^2, which was then advected by the tangential circulation of the developing storm. This type of convective activity was observed throughout the rest of Jangmi's spin-up into a supertyphoon (see Figures 47a,b in Appendix K).

A timely CLOUDSAT pass at 1709 UTC 25 September sampled a cell in the southern quadrant of Jangmi (Figure 33) that extended to an altitude of nearly 17 km. The vigor of the convection was confirmed by the appearance of a central dense overcast (CDO) covering the eye of Typhoon Jangmi during a reconnaissance mission late on 25 September (Sanger 2008b).

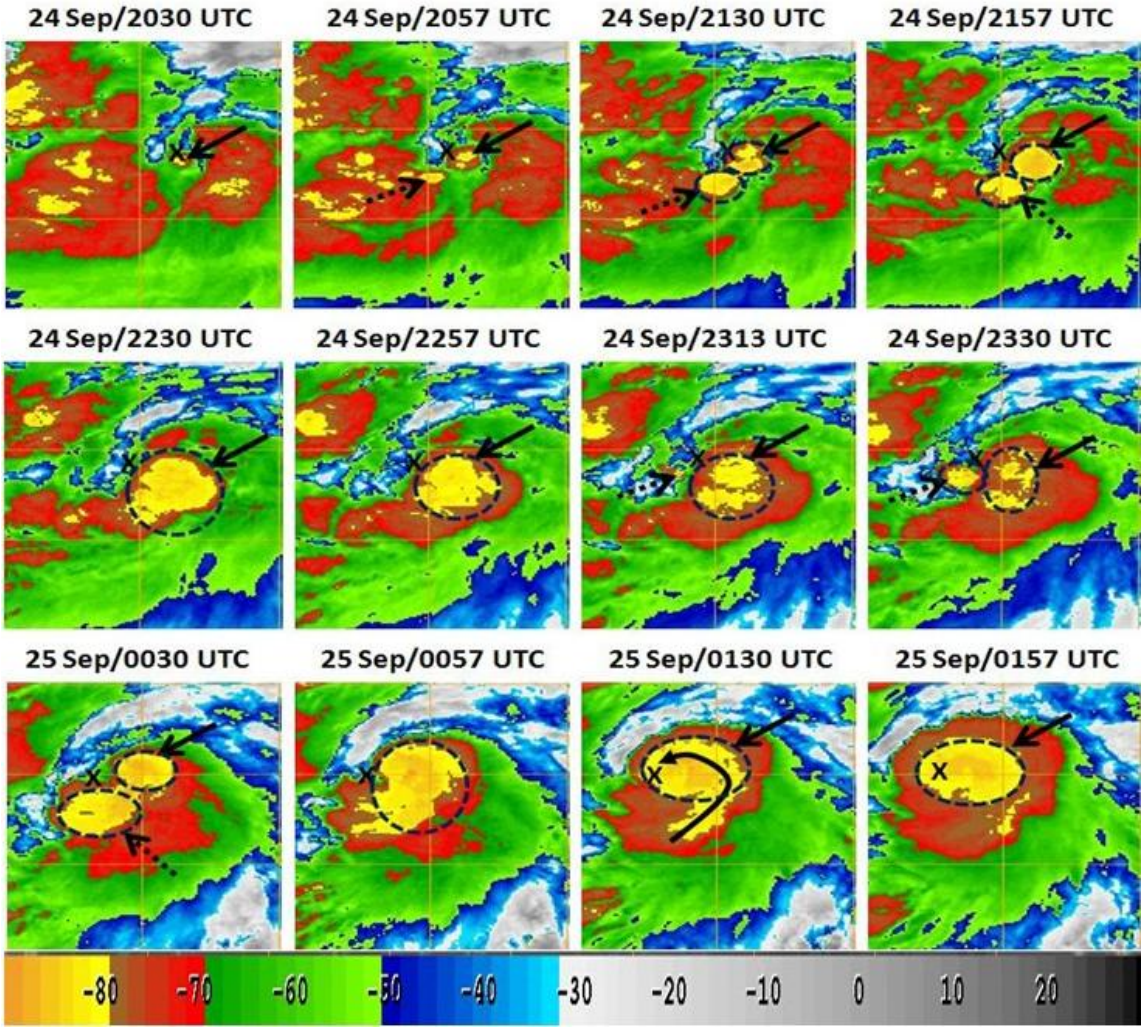

Figure 31. Series of 1-km MTSAT infrared imagery of deep convective clouds in TS Jangmi from 2030 UTC 24 September – 0157 UTC 25 September 2008. Dashed blue circles indicate deep convection and its approximate areal extent and shape. TS Jangmi center based on the 10-minute storm track file (see Chapter III, Section E for description) is shown with black "**X**." Note the increase in horizontal coverage in both areas of deep convective clouds, possible cloud merger in 0057 UTC 25 Sep panel, and inward spiral of clouds in second to last panel at 0130 UTC 25 Sep. The color bar at bottom of plot associates cloud-top temperatures with various colors. The coldest cloud-top temperatures are shown with shades of red and yellow (-70°C to -90°C). Imagery courtesy of Naval Research Laboratory, Monterey, CA.

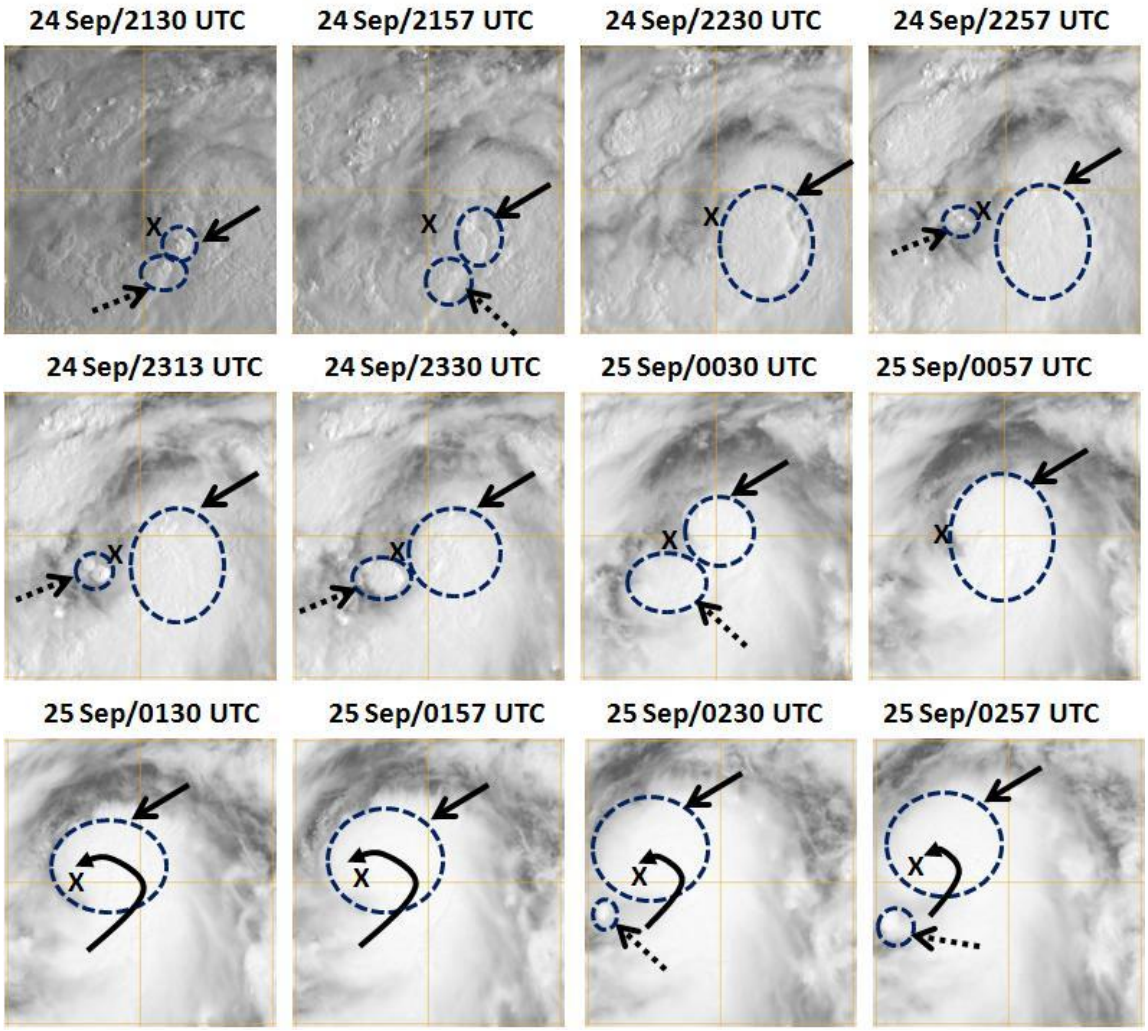

Figure 32. Series of 1-km MTSAT visible imagery depicting deep convective clouds in TS Jangmi from 2130 UTC 24 September – 0257 UTC 25 September 2008. Dashed blue circles indicate areas of deep convection and its approximate areal extent, shape, and overshooting tops. TS Jangmi center based on the 10-minute storm track file (see Chapter III, Section E for description) is shown with black "**X**." Note the increase in horizontal coverage of deep convective clouds, possible cloud merger in 0057 UTC 25 Sep panel, and inward spiral of clouds in the last four panels (0130 – 0257 UTC 25 Sep). Imagery courtesy of Naval Research Laboratory, Monterey, CA.

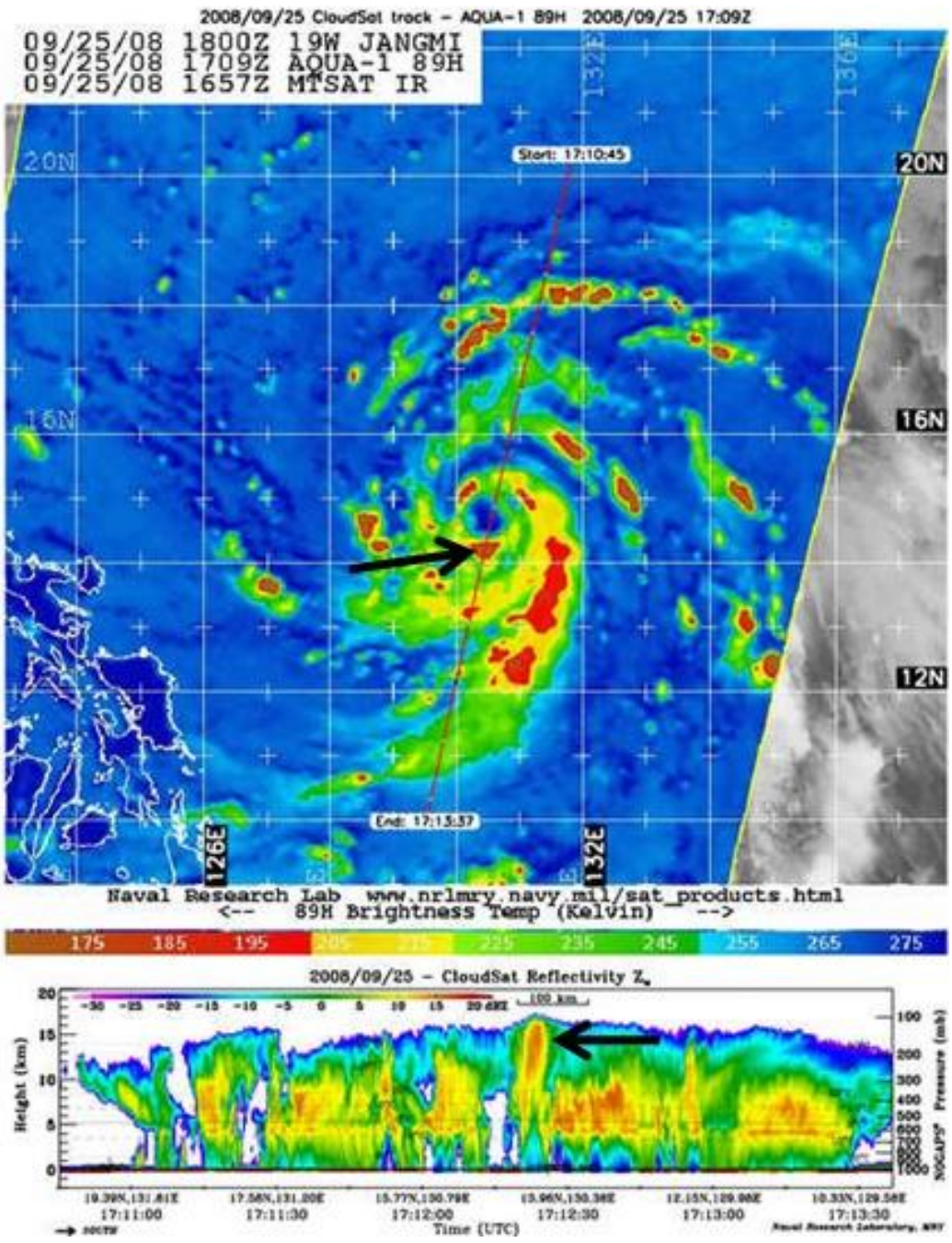

Figure 33. CLOUDSAT reflectivity (bottom) through Typhoon Jangmi during pass from north to south from 1711 – 1713 UTC 25 September 2008 with associated AQUA microwave satellite image at 1709 UTC 25 September 2008. Note the deep convection in the southern eyewall extending up to 17 km altitude. The color bar in between the reflectivity and satellite image associates cloud-top temperatures in Degrees Kelvin (K) with various colors. The lowest cloud-top temperatures are shown with shades of red and orange (200K to 170K). (Images courtesy of Colorado State University/NESDIS/CIRA, Fort Collins, CO).

2. Hurricane Georges

Throughout the spin-up of Hurricane Georges, the deep convective activity was similar to that observed in Supertyphoon Jangmi (see Figure 34 below and Figure 48 in Appendix L).

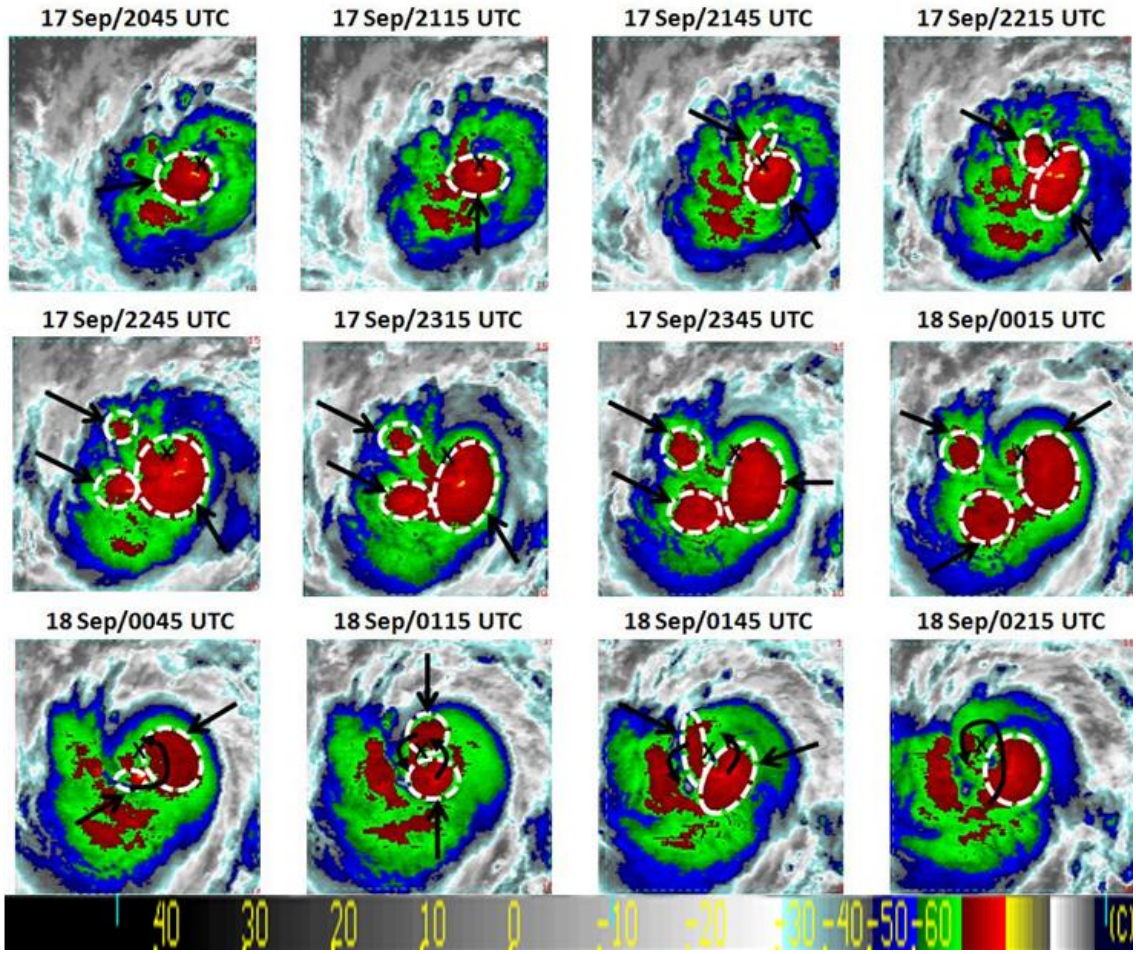

Figure 34. Series of NOAA GOES-8 4 km infrared imagery deep convective clouds in Hurricane Georges from 2045 UTC 17 September – 0215 UTC 18 September 1998. Dashed white circles indicate deep convection and its approximate areal extent and shape. Georges' center is based on the 10-minute storm track file (see Chapter III, Section E for description) is shown with black "**X**." Note that two cells begin rotating counterclockwise around the storm center at 2215 UTC 17 September 1998 and begin to spiral inward. The color bar at bottom of plot associates cloud-top temperatures with various colors. The lowest cloud-top temperatures are shown with shades of red and yellow (-70°C to -90°C). Imagery is courtesy of John Knaff of NOAA/NESDIS/CIRA, Fort Collins, CO

In summary, analysis of the deep convective activity in both Georges and Jangmi using high-resolution satellite imagery revealed frequent deep convective bursts with associated anvil clouds having cloud-top temperatures ≤ -65°C. The anvil clouds from these convective events spread to cover large horizontal areas, moved counterclockwise around the relatively cloud-free eye, and underwent merger. In both storms, convective cells/anvils were predominant during the entire spin-up of the vortex from a tropical storm to a strong Category 4 and Category 5 tropical cyclone, suggesting that they may be playing a major role in the intensification process.

To aid the interpretation of the deep convection discussed above, the results of a mesoscale analysis of ELDORA data collected in TS Jangmi will be explored in the next section. However, a brief overview of the ELDORA radar is conducted first to ensure accurate assessment of the data.

C. ELDORA RADAR OBSERVATIONS IN TROPICAL STORM JANGMI

1. Overview

The ELDORA radar onboard the NRL P-3 provided an unprecedented documentation of deep convection in TS Jangmi on 24 September 2008. The ELDORA domain is overlaid with the 2313 UTC 24 September MTSAT infrared imagery (Figure 35). The ELDORA analysis during 2310 – 2320 UTC 24 September was during a period in which the NRL P-3 traversed the southern portion of the rectangular domain, where extremely low cloud-top temperatures of < -75°C were observed in the 2313 UTC 24 September MTSAT infrared imagery. An area of deep convective clouds is analyzed with the ELDORA radar data from a plan view at 1.5 km altitude and 8 km altitude and along a vertical cross-section shown by the solid purple line in Figure 35. The goal of this radar analysis is to investigate whether the convection located underneath the extremely cold infrared imagery cloud tops of TS Jangmi during 2310 – 2320 UTC 24 September has rotation.

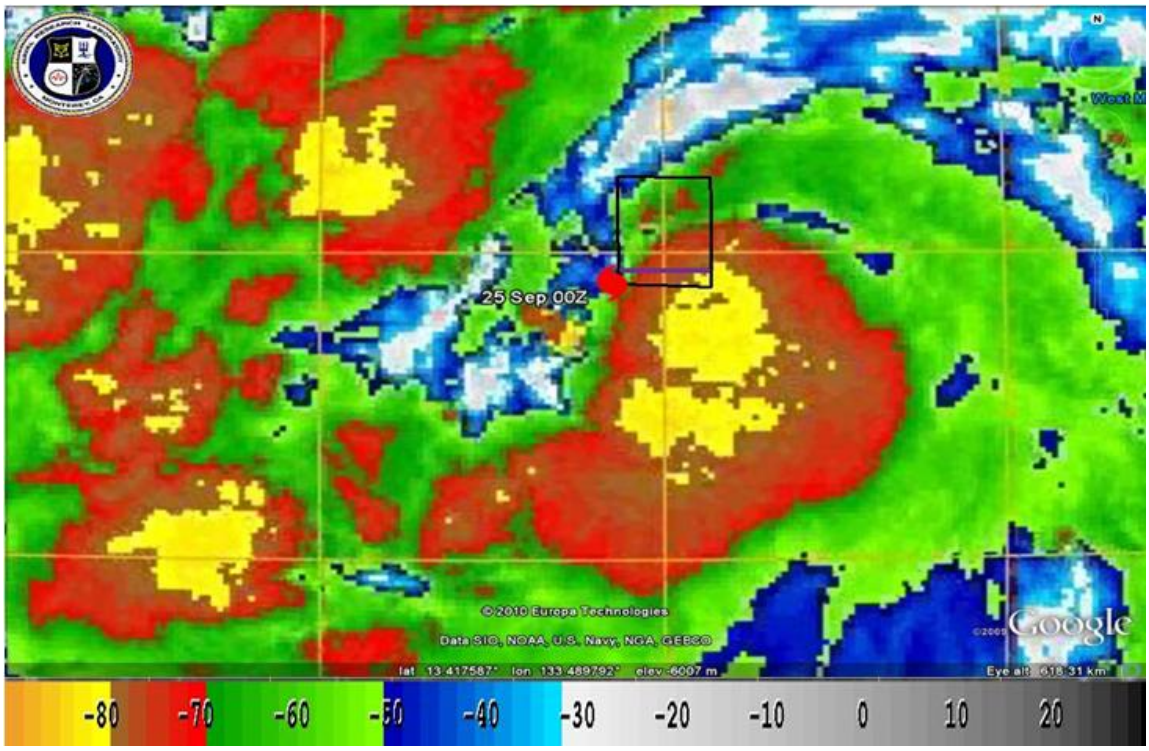

Figure 35. 1 km MTSAT infrared imagery at 2313 UTC 24 September 2008 during NRL P-3 ELDORA mission into Tropical Storm Jangmi. The 0000 UTC 25 Sep storm position based on the 10-minute storm track file is shown with red tropical cyclone symbol. The ELDORA data domain is shown with the black rectangle. The location of the cross-section shown later in Figure 38 is depicted by solid purple line. The color bar at bottom of plot associates cloud-top temperatures with various colors. The lowest cloud-top temperatures are shown with shades of red and yellow (-70°C to -90°C).

2. Data Description

The ELDORA data were corrected first for navigational and positioning errors and edited to remove the ocean surface echoes, noise, and other suspect radar data (Oye et al. 1995; Bosart et al. 2002). Next, the three-dimensional dual-Doppler winds and precipitation fields were calculated on an isotropic 500 m grid using a variational synthesis technique (Reasor et al. 2009). These radar observations are unique in both their location in the western North Pacific Ocean and in the high resolution of the convection at the meso-gamma scale (2 km – 20 km) during the incipient spin-up of a tropical storm into a typhoon.

3. Mesoscale Analysis

The analysis of the 1.5 km altitude radar data from the southern half of the rectangular region in Figure 36 reveals convection arrayed in spiral bands around the storm center (Figure 37a). Earth-relative winds in Figure 37b indicate strong southerly to southeasterly flow of 35 m s^{-1} to 40 m s^{-1} located in the outermost spiral band. The innermost spiral band has lower wind speeds between 12 m s^{-1} and 27 m s^{-1}. The vertical vorticity and vertical velocity in Figure 37c reveal three regions of co-located positive relative vorticity and vertical updrafts that are associated with convective cells in the southern portion of the storm. In this region, large relative vorticity on the order of 2×10^{-3} s^{-1} and vertical velocities between 4 m s^{-1} and 5 m s^{-1} are analyzed. Both of these regions are also in areas of significant low-level convergence on the order of 2×10^{-3} s^{-1} (Figure 36d). A few other areas of co-located, enhanced relative vorticity, convergence, and vertical velocity with values of 2×10^{-3} s^{-1}, 2×10^{-3} s^{-1}, and 2 m s^{-1}, respectively, are analyzed in the northern half of the outer spiral band.

In the outermost spiral band in Figures 36c,d, there are multiple updraft and downdraft dipoles, as well as positive and negative relative vorticity dipoles. The most dominate dipole pattern is observed in the lower right portion of Figure 36c,d. Due to these dipoles of vertical velocity and relative vorticity, there may be some offset in spin-up occurring in the outermost spiral band. In contrast, the innermost spiral band contains only couplets of updrafts and positive relative vorticity. As a result of these different patterns of vertical velocity and relative vorticity, the innermost and outermost spiral bands may be contributing different levels of spin-up or spin-down to the primary circulation. Further work needs to be accomplished in this area, but is beyond the scope of this research.

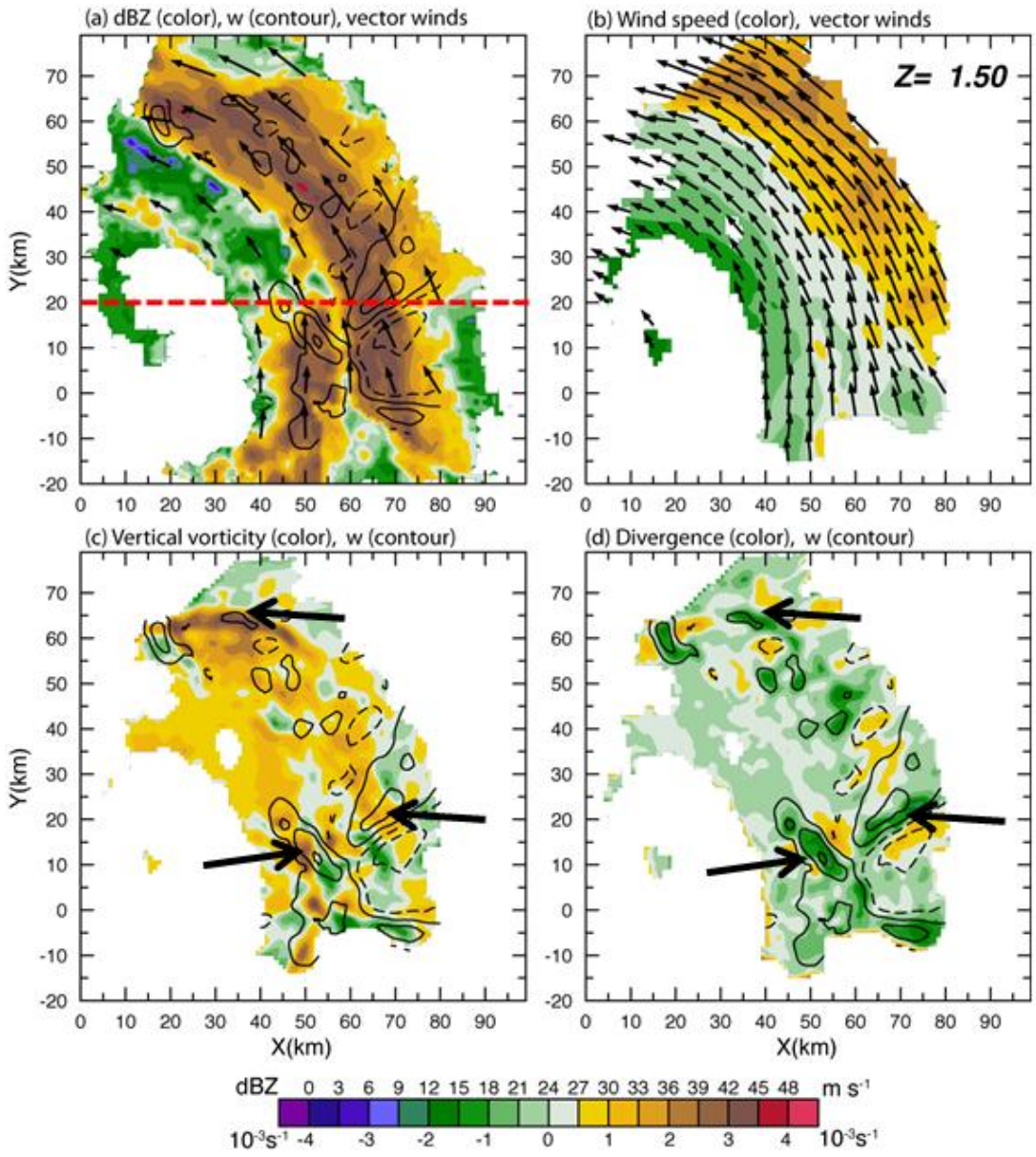

Figure 36. ELDORA analysis from 2310 -2320 UTC 24 September 2008. Panel (a) shows horizontal plan view of radar reflectivity (color, dBZ), wind vectors, and vertical velocity (contour, 2 m s^{-1} increments; solid contours are positive) at 1.5 km altitude. The red dashed line indicates location of the vertical slice to be examined later in Figure 38. Panel (b) depicts wind vectors and speed (color contoured in m s^{-1}) in the earth-relative frame at 1.5 km altitude. Panel (c) shows horizontal plan view of relative vertical vorticity (color, 10^{-3} s^{-1}) and vertical velocity (contour, 2 m s^{-1} increments; solid contours are positive) at 1.5 km altitude. Panel (d) shows divergence (color, 10^{-3} s^{-1}) and vertical velocity (contour, 2 m s^{-1} increments; solid contours are positive) at 1.5 km altitude. Arrows show regions of cyclonic vorticity, convergence, and updrafts.

The analysis of the 8.0 km altitude ELDORA radar data from the southern half of the boxed region in Figure 35 reveals reflectivity values between 18 dBZ to around 30 dBZ (Figure 37a) at and below y = 20 km and between x = 63 km and x = 75 km. Earth-relative winds in Figure 37b indicate southerly to southeasterly flow of 21 m s^{-1}- 27 m s^{-1} in the outermost spiral band. The innermost spiral band contains lower wind speeds between 2 m s^{-1} and 15 m s^{-1}. Near the center of the outermost spiral band, enhanced vertical vorticity values of 2.0×10^{-3} s^{-1} are co-located with strong updrafts vertical velocities of over 9 m s^{-1} and divergence of approximately 3.0×10^{-3} s^{-1} (Figures 37c,d). There is also a smaller region of elevated levels of co-located positive relative vorticity on the order of 1.0×10^{-3} s^{-1} and upward vertical velocities of 1 – 3 m s^{-1}.

The ELDORA radar analysis at both 1.5 km and 8.0 km altitude shows that underneath this region of extremely cold infrared cloud tops there are multiple rotating deep convective cells. To investigate this further, a vertical cross-section of the strongest updraft is taken at y = 20 km (denoted by the dashed red line in Figures 36a and 37a).

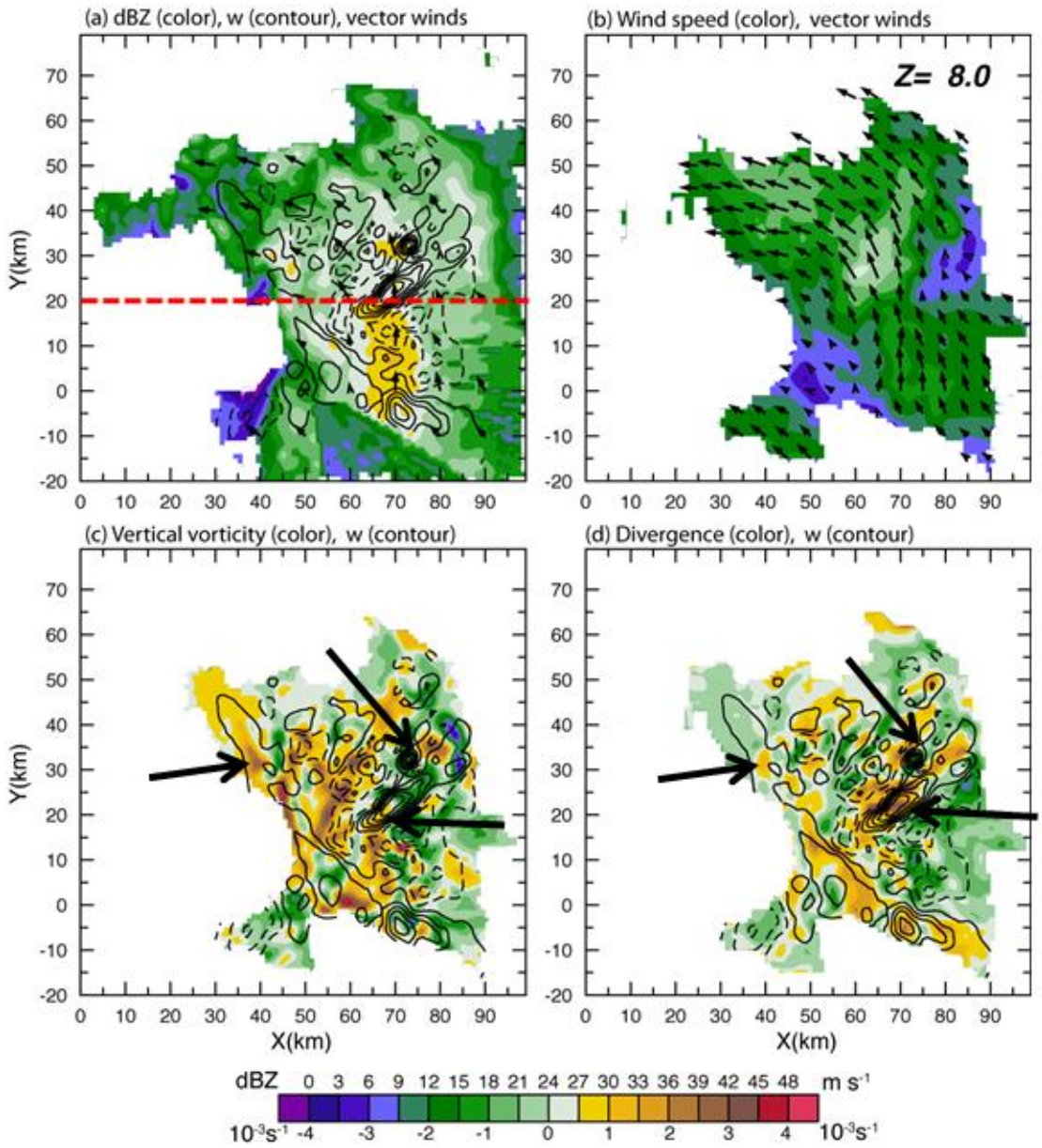

Figure 37. ELDORA analysis from 2310 -2320 UTC 24 September 2008. Panel (a) shows horizontal plan view of radar reflectivity (color, dBZ), wind vectors, and vertical velocity (contour, 2 m s^{-1} increments; solid contours are positive) at 8 km altitude. The red dashed line indicates location of the vertical slice to be examined later in Figure 38. Panel (b) depicts wind vectors and speed (color contoured in m s^{-1}) in the earth-relative frame at 8.0 km altitude. Panel (c) shows horizontal plan view of relative vertical vorticity (color, 10^{-3} s^{-1}) and vertical velocity (contour, 2 m s^{-1} increments; solid contours are positive) at 8.0 km altitude. Panel (d) shows divergence (color, 10^{-3} s^{-1}) and vertical velocity (contour, 2 m s^{-1} increments; solid contours are positive) at 8 km altitude. Arrows show regions of cyclonic vorticity, divergence, and updrafts.

The vertical cross-section in Figure 38a reveals the existence of strong, upright radar reflectivities greater than 45 dBZs that extend to an altitude of around 6 km with a horizontal extent of about 12 km. In addition, radar reflectivities of ~ 15 dBZ stretch to an altitude of more than 15 km. Strong upward vertical velocities on the order of 4 m s^{-1}-9 m s^{-1} are analyzed in the moderate to strong radar reflectivities rising to around 11 km altitude.

In Figure 38c, a coupling of strong, upright vertical vorticity and a 12 km wide vertical updraft is analyzed from an altitude of 1.5 km up to 13 km. Two relative vorticity peaks of greater than 4×10^{-3} s^{-1} at heights of 3 km and 11 km are co-located with ~ 3 – 4 m s^{-1} vertical velocities. There is a maximum vertical velocity of 9 m s^{-1} in between the two vertical vorticity peaks, at an altitude of 8 km that is co-located with vertical relative vorticity of approximately 0.5×10^{-3} s^{-1}. Large horizontal convergence values between 2.0×10^{-3} s^{-1} and 3.5×10^{-3} s^{-1} are analyzed below 2 km altitude and between 4 km and 6 km altitude.

In summary, the ELDORA radar analysis indicates multiple areas of rotating deep convection were present near the vortex center of TS Jangmi between 2310 UTC and 2320 UTC 24 September 2008, just hours before intensification to a typhoon. In one instance, there was a coupling of strong upright vertical vorticity with a 12 km wide vertical updraft along with strong low-level convergence.

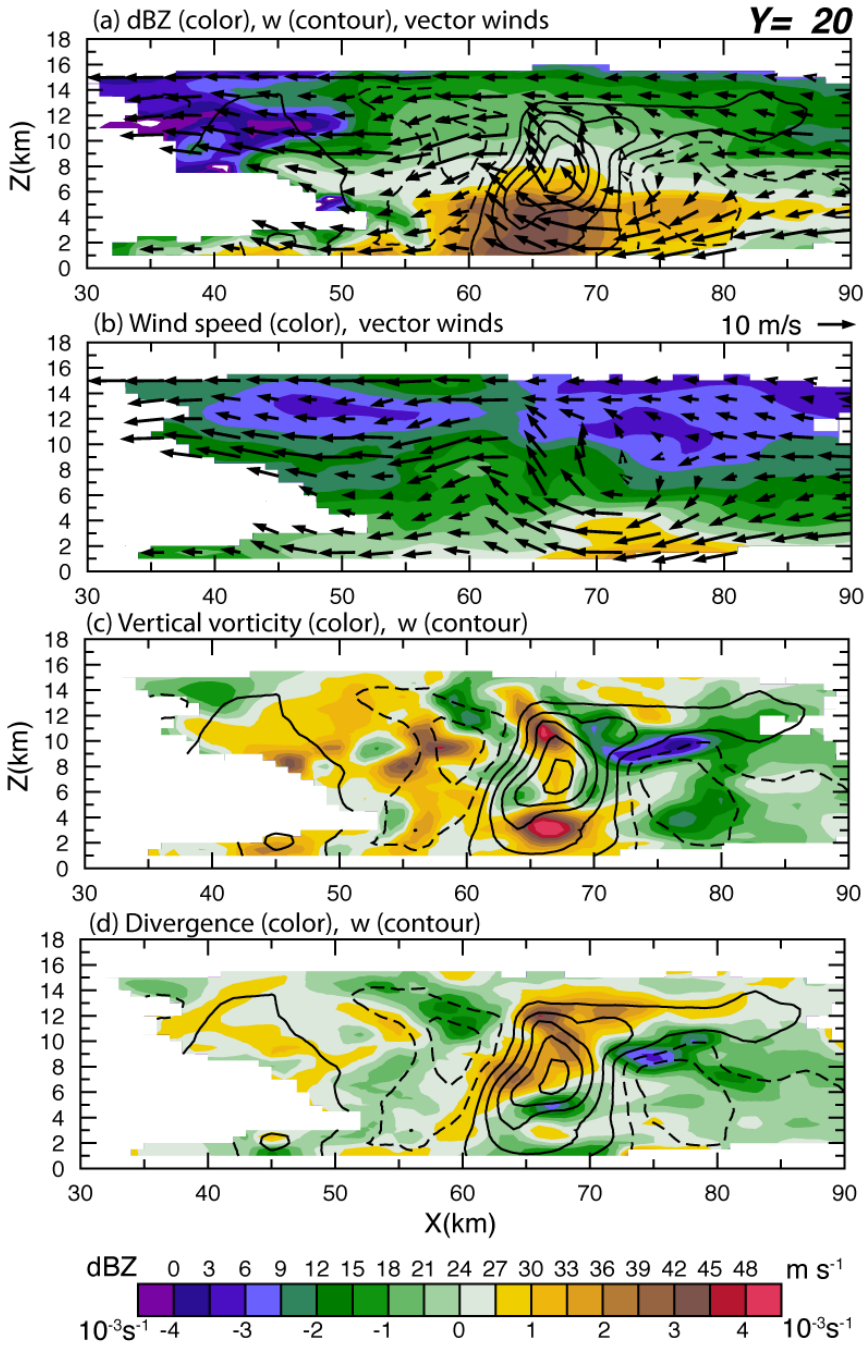

Figure 38. ELDORA vertical-zonal cross-section analysis from 2310-2320 UTC 24 September 2008. Panel (a) depicts reflectivity (color), wind vectors in the vertical-zonal plane, and vertical velocity (contours, 2 m s^{-1} increments; solid contours are positive). Panel (b) shows earth-relative wind velocity in m s^{-1} (color), and wind vectors in the X-Z plane. Panel (c) depicts vertical relative vorticity (color) and vertical velocity in m s^{-1} (contours, 2 m s^{-1} increments; solid contours are positive). Panel (d) depicts divergence (color, 10^{-3} s^{-1}) and vertical velocity (contour, 2 m s^{-1} increments).

4. Implications

The rotating deep convection found in TS Jangmi is similar to that in the recent pioneering numerical modeling studies of Hendricks et al. (2004), M06a, NSM08 and Shin and Smith (2008), which showed the importance of these rotating updrafts to spin-up. Moreover, these findings of rotating deep convective cells in TS Jangmi are consistent also with previous studies of various asymmetric features of tropical cyclones using airborne Doppler radar and dropsonde data (Marks and Houze 1984; Reasor et al. 2005; Reasor et al. 2009; Houze et al. 2009; Bell and Montgomery 2010; hereafter BM10; Raymond and Carrillo 2011). All of these studies noted that deep convective cells may contribute to spin-up of the vortex.

In a recent study, BM10 analyzed ELDORA radar observations from a TCS08 mission in pre-Tropical Depression Hagupit to identify "vorticity-rich, buoyant convective plumes" close to the developing low-level circulation. They documented an intense, tilted updraft with a peak vertical velocity of around 25 m s^{-1} at 12 km altitude (their Figure 2c) associated with the leading edge of a convective line that had large values of low-to mid-level convergence. They noted that this convective structure had a low-level, positive vertical vorticity core that extended to a height of 6 km, with maximum values of more than 8×10^{-3} s^{-1} at an altitude of 4 km. These ELDORA observations validated the presence of vortical, deep convective structures in a pre-depression disturbance in the tropics. BM10 noted that the co-location of strong vertical vorticity and convergence in the boundary layer indicates stretching of the pre-existing low-level cyclonic vorticity, in agreement with the amplification pathway in the idealized numerical simulations of NSM08. Additionally, they hypothesized that continuous convective bursts similar to those documented in their work were mainly responsible for the development of Hagupit as the storm traveled westward in the western North Pacific.

In a study of the vorticity budget during the spin-up of Typhoon Nuri (2008), Raymond and Carrillo (2011) suggested that the change from scattered, ordinary convection to a more limited number of strong cells eventually led to the development of the tropical cyclone eyewall in Nuri.

As a result of the mesoscale radar analysis in Jangmi and the previous studies mentioned above, it is inferred that rotating deep convective structures are present underneath the extremely cold infrared imagery cloud tops during the spin-up of both Supertyphoon Jangmi and Hurricane Georges.

VI. SUMMARY AND CONCLUSIONS

An observational study of tropical cyclone spin-up (i.e., intensification) in Supertyphoon Jangmi and Hurricane Georges was conducted to help determine the most appropriate theory of intensification.

To ensure a proper interpretation of the observations, a review of the three major tropical cyclone spin-up theories was performed first. The review summarized the Ooyama (1969) conventional view of spin up, the WISHE theory (Emanuel 1989; 1995; 1997), and the axisymmetric and asymmetric perspectives of a newly proposed spin-up theory involving rotating deep moist convection (NSM08; MNSP09; SMN09: BSMP09). A review of the boundary layer and its role in tropical cyclone spin-up was presented next. Due to the inability of any definition to portray accurately the complex inner-core boundary-layer separation process, a practical dynamical definition was developed for the purposes of this observational study of tropical cyclone spin-up. Specifically, the definition of the inner-core tropical cyclone boundary layer was adapted from SMN09 as the layer containing significant gradient wind imbalance ($\geq$ 10%), typically at least 500 m to 1 km in depth, which arises primarily from frictional effects.

Using NCAR GPS dropsondes released during routine reconnaissance missions and the TCS-08 field campaign, the individual and composite vertical profiles of the kinematic data were constructed to examine the inner-core boundary layer region. The analysis revealed that both the peak and maximum axisymmetric mean tangential wind speed occurred largely within the boundary layer of approximate steady-state Hurricane Georges and of all three stages of Supertyphoon Jangmi. Based on observations from Jangmi that the peak and maximum axisymmetric mean tangential wind speed occurred within the boundary layer during both spin-up and steady-state, and the SMN09 theoretical and modeling study showing similar results, it stands to reason that the maximum tangential wind was located within the boundary layer of Georges during spin-up also. Taken together, these results support the new intensification theory, which predicts, *inter alia*, that the peak mean tangential wind speed during spin-up occurs within the boundary layer.

An assessment of gradient wind balance was conducted at altitudes of 275 m, 500 m, 750 m, 1000 m, 1250 m, and 1500 m using dropsondes launched within the inner core of Hurricane Georges and all three stages of Supertyphoon Jangmi. The analyses suggest the presence of measurable supergradient winds in the boundary layer near and just within the RMW in all three stages of Jangmi's evolution and Georges' near steady-state. The largest supergradient winds occurred just inside the RMW during the peak intensity of both storms. The possibility of the existence and spatial structure of supergradient winds near and within the RMW supports the argument advanced in SMV08, SMN09, and Smith and Montgomery (2010) that unbalanced boundary-layer dynamics in the inner-core region are an important component in the determination of the maximum axisymmetric mean radial and tangential flow speeds that can be attained in real storms. Subgradient winds are observed also outside of the RMW and inside the eye region for both storms.

These analyses appear to document observations that support the new theory that axisymmetric supergradient winds exist in the boundary layer near and just within the RMW of an intensifying tropical cyclone. However, as a result of data limitations from asymmetries, irregular placement of dropsondes in both time and space, storm intensification, changes in storm translation speed, and the compositing technique, a strongly conclusive statement for Tropical Storm Jangmi is not possible. Upon considering all of the caveats involved with the axisymmetric gradient wind calculations, it is clear that a dense deployment of dropwindsondes across the RMW in each radial leg will be necessary to resolve the pressure gradient with sufficient accuracy to validate whether or not axisymmetric supergradient winds exist at the tropical storm stage generally.

To gain a more complete perspective of the asymmetric processes implicated in the new spin-up theory, an analysis of deep convection and their associated anvil clouds was carried out for Georges and Jangmi using high-resolution satellite imagery. In addition, ELDORA observations were analyzed during the tropical storm stage of Jangmi. The analyses of the ELDORA observations together with the analysis of satellite imagery during the evolution of Supertyphoon Jangmi and Hurricane Georges imply the

general presence of rotating deep convective cells during the spin-up of both storms and supports a portion of the new theory that predicts the presence and collective importance of these structures during spin-up. This conclusion is consistent also with basic fluid dynamical principles. Although previous work has long suggested the importance of deep convection to tropical cyclone spin-up, this analysis provided a quantitative assessment of the characteristics of some of the rotating updrafts in a tropical storm in the deep tropics nearing typhoon strength and suggests that cold cloud top temperatures can serve as a proxy for rotating deep convection in a rotating environment.

The existence of rotating deep convection in the inner-core region of an intensifying storm indicates the presence of local buoyancy. This local buoyancy is available to drive ascent that in turn stretches the pre-existing relative vorticity, thereby increasing rapidly the local vorticity well beyond that of the environment on a time scale of a few hours. Based on these analyses, it was argued that rotating deep convective cells were active during the spin-up of Georges and all three stages of Jangmi. These results are consistent with the NSM08 model findings of prevalent rotating deep convective clouds near the center during rapid intensification. It is hypothesized that rotating deep convection was the primary mechanism of tropical cyclone spin-up in both storms (i.e., increased convergence of absolute angular momentum within the lower troposphere and amplification of pre-existing vorticity via vortex tube stretching). Further study of multiple storms using ELDORA for longer periods of time during spin-up is required to analyze impacts of rotating deep convection on the primary circulation to confirm or falsify this assertion. The use of ELDORA Doppler radar data and/or NOAA P-3 Doppler radar in conjunction with routine reconnaissance missions is essential for documenting the evolution of vorticity, vertical velocity, and convergence in and near these areas of deep convection and quantifying their impact on the vortex-scale thermodynamics and dynamics.

The observational results presented herein support a portion of the new theory on tropical cyclone intensification that inner-core spin-up occurs within the boundary layer and rotating deep convection is predominant throughout spin-up. These findings may spur basic improvements of tropical cyclone intensity forecasting models. If the tropical

cyclone intensification process is correctly represented in both theory and models, forecasters at the NHC and JTWC will have improved tools for making more reliable 24-h – 72-h intensity forecasts. Improved forecasts are essential for protecting the lives of military and civilian personnel and their family members living in tropical cyclone prone areas along the U.S. Gulf Coast and Atlantic Coast and in the western North Pacific Ocean. Better forecasts are key also to maximizing the safety of multi-million dollar military aircraft based in other tropical cyclone prone areas such as Andersen Air Base, Guam and U.S. Navy ships transiting the western Pacific, Gulf of Mexico, and Atlantic Ocean basins.

APPENDIX A: NCAR GPS DROPSONDES

The Global Positioning System (GPS) dropsonde provides pressure, temperature, and relative humidity (PTH), and horizontal wind speed at 2 Hz temporal resolution (0.5 s^{-1}) while descending at a rate between 12 m s^{-1} $ms^{-1}$and 15 m s^{-1} ms^{-1}in the lower troposphere.

A. ACCURACY

Hock and Franklin (1999) estimated that the dropsonde has vertical resolution of about 5 m with typical PTH errors below 1.0 hPa, 0.2°C, and 5%, respectively, with the exception of sensor wetting situations as outlined in Eastin et al. (2005). The wind speed errors are less than 0.5 m s^{-1}. One exception to these error estimates may occur in regions of strong vertical motions (> 15 m s^{-1}) located in the eyewall region of a tropical cyclone. The vertical velocity can be deduced from the dropsonde by removing the estimated terminal fall speed of the dropsonde as a function of pressure. This method has an estimated error of 0.5 - 1.0 m $s^{-1}ms^{-1}ms^{-1}$ for mesoscale vertical motions in hurricanes (Franklin et al. 2003, their Figure 2 and Table 1). NCAR/EOL and NOAA/HRD calculated the vertical velocity for all dropsonde observation points in Supertyphoon Jangmi and Hurricane Georges, respectively.

B. LIMITATIONS

There are a few limitations to the dropsonde when it is launched into the eyewall region of a tropical cyclone. For instance, dropsondes released in the eyewall of a tropical cyclone can travel a large distance in the azimuthal direction as they fall and rotate counter-clockwise around the storm center (Franklin et al. 2003). The usual downwind rotation in the eyewall of a mature tropical cyclone during the approximate four-minute dropsonde fall time from an altitude of 700 hPa is 10° – 30°. In addition, the dropsonde can be displaced inward significantly due to the presence of strong radial wind velocities (> 10 m s^{-1}). Consequently, the dropsonde does not yield a true vertical profile, especially in the eyewall region where radial and tangential velocities tend have large amplitudes.

Another limitation of these dropsondes is that inside of the eyewall many of the wind speed sensors fail in the last 100 m of flight (Franklin et al. 2003), which was a problem in many of the Hurricane Georges' dropsondes. However, very few of the eyewall dropsondes in Supertyphoon Jangmi failed near the surface.

C. QUALITY CONTROL

Quality control of the entire set of 200 dropsondes in Georges and Jangmi to remove noise and other instrument errors by using the NCAR Atmospheric Sounding Processing Environment (ASPEN) software or the NOAA/HRD Editsonde software during post-processing. For Georges, all of the dropsondes were generously post-processed by NOAA/HRD using the Editsonde program. In the case of Jangmi, the entire set of dropsondes was post-processed using the ASPEN software. In addition to these two quality control programs, a manual investigation of each dropsonde was accomplished to eliminate any bad data points that were missed by the quality control software.

Although the post-processing removes the major relative humidity errors, possible sensor wetting and/or molecular contamination may result in an uncertainty of 2 - 4 K in θ_e (Eastin et al. 2002). These sensor-wetting problems, which cause evaporation and drying, are most common in the eyewall and may cause a low bias of θ_e. This sensor uncertainty for θ_e is significant, since the θ_e signal that is important to this research is ~ 5 - 10 K. However, the composite θ_e results for Georges and Jangmi did not reveal any potential dry bias problems. Furthermore, a manual check of the 27 eyewall dropsondes in Jangmi revealed only four data points with a dry bias due to sensor wetting. These four spurious data points were removed from the analysis.

Additionally, quality control issues occur occasionally in the extreme wind region of the eyewall. The ASPEN quality control algorithms do not correctly process the updraft data when the upward air motion is greater than the terminal fall speed of the dropsonde (~ 12 m s^{-1} near the surface). This situation is known also as an "upsonde," since the dropsonde is traveling upward. For the upsonde case, ASPEN simply removes the data within the strong updrafts, while Editsonde keeps it. A manual check of each

eyewall dropsonde revealed that there were no significant upsonde cases in both Georges and Jangmi.

After performing the quality control check, there were 92 dropsondes available for the observational study of steady-state maintenance in Hurricane Georges. Of these dropsondes, 79 were located in the inner-core and outer-core regions. The remaining 13 dropsondes were launched from the NOAA GIV aircraft in the region 250 – 800 km radius from center.

For Supertyphoon Jangmi, the quality control check resulted in the availability of 109 dropsondes for the observational study of spin-up between 24 and 27 September 2008. Out of these dropsondes, 95 were released in the inner-core and outer-core regions of Jangmi. The remaining 14 dropsondes were launched in the ambient region (300 – 800 km radius from center) or outer environment region (> 800 km radius from center) of the storm.

THIS PAGE LEFT INTENTIONALLY BLANK

APPENDIX B: ELDORA METHODOLOGY

A. DESIGN AND SCANNING STRATEGY

The ELDORA airborne radar has been used over the past 15 years to collect high-resolution in situ measurements of Doppler reflectivity and velocity in a wide variety of convective environments. The ELDORA is a 3.2-cm X-band wavelength radar with a 1.4-m diameter antenna, 1.8° beamwidth, 38.7 dB gain, 35-40 kW peak power, 144° s^{-1} scan rate, and around -35 dB sidelobes. A dual beam, helical scanning configuration is exploited to effectively scan the entire volume surrounding the aircraft and obtain the two (fore and aft) velocity components required for the three-dimensional wind field calculation (Testud 1995). A greater than 30° angle between the two beams is necessary to ensure collection of accurate, high-resolution velocities. The radar rotates about an axis that is parallel to the longitudinal axis of the aircraft, with the beams tilted ~18.5° fore and aft of a plane normal to the aircraft axis. This scanning strategy is shown in Hildebrand et al. (1995, their Figure 2). As a result of this geometric strategy, the two radar beams yield continuous sampling on both sides of the plane as it flies along.

B. DATA ANALYSIS PROCESS

During the TCS-08 field experiment, the ELDORA provided ~ 500 m along-track resolution with an unambiguous range of ~ 60 km in convection (M.M. Bell 2009, personal communication). The focus of radar data collection for this research took place between 2310 -2320 UTC 24 September 2008 during several legs in Tropical Storm Jangmi.

The raw radar data for Tropical Storm Jangmi were corrected using the method outlined in Testud (1995) for inertial navigation system (INS) errors and problems due to misrepresentation of the Earth's surface due to large-amplitude surface gravity waves. During the flight into Jangmi, the aft radar underestimated the radar reflectivity by up to 7 dBZ. The INS uncertainties include those in: (i) horizontal velocity, (ii) drift angle, (iii) aircraft vertical velocity, (iv) pitch angle, (v) tilt angle, (vi) roll/spin angle, and (vii) mounting errors. The surface of the Earth causes errors also since it is tilted, not

stationary, and moves at varying speeds. The data corrections result in the removal of ground-echo noise, clutter, radar side lobes, and velocity unfolding. After corrections are made, the data are interpolated onto a Cartesian grid mesh and multiple, gridded data files are synthesized to obtain a three-dimensional wind field and other derived quantities. The three-dimensional dual-Doppler winds and precipitation fields were calculated on an isotropic 500 m grid using a variational synthesis technique. This method solves the radial velocity equations and the mass continuity equation simultaneously. Finally, a three-step low-pass filter ($< 8\ \Delta x$) was performed to eliminate noise in the output fields.

APPENDIX C: TROPICAL STORM JANGMI GRADIENT WIND BALANCE ANALYSIS

The TS Jangmi gradient wind balance results for the remaining five altitudes (275 m, 750 m, 1000 m, 1250 m, and 1500 m) from the discussion in Chapter IV, Section A3 are shown below in Figure 39 a-j.

(a)

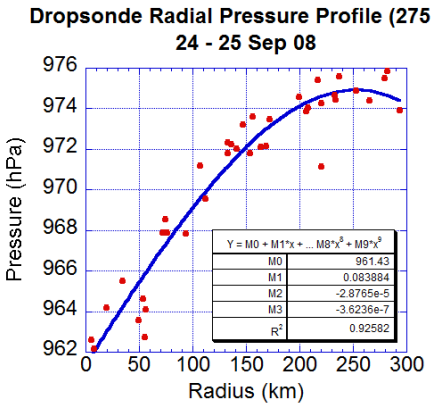

(b)

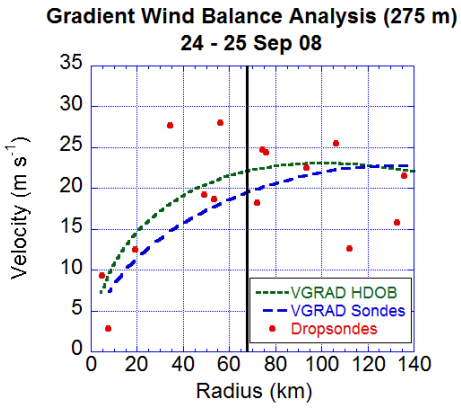

(c)

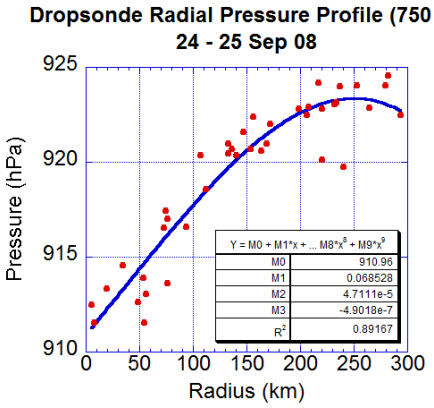

(d)

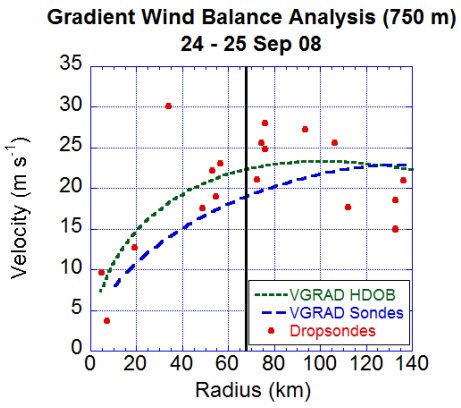

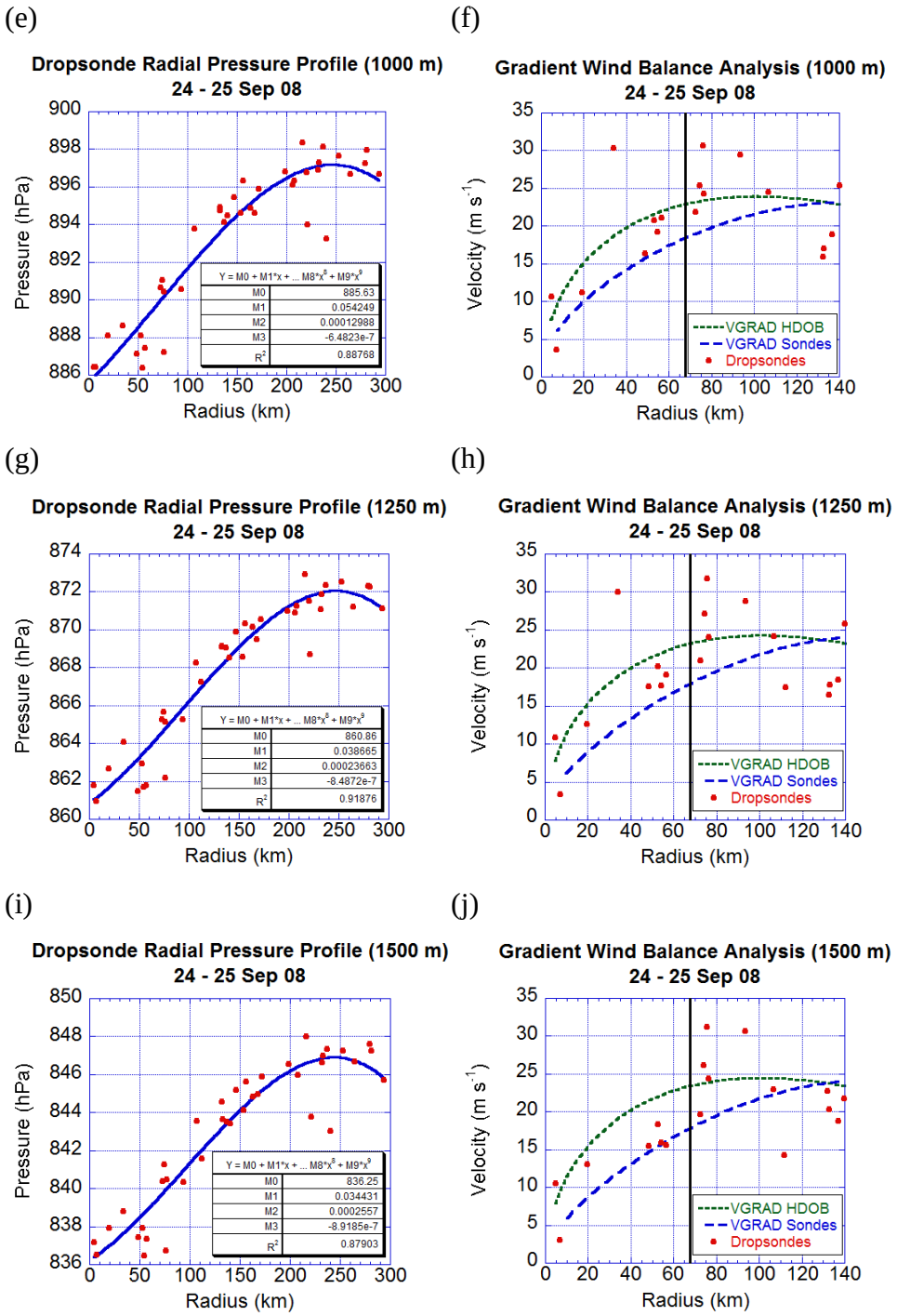

Figure 39. Tropical Storm Jangmi observed pressure (hPa) from dropsondes (solid red circles) and 3rd degree polynomial fit (solid blue line) at (a) 275 m, (c) 750 m, (e) 1000 m, (g) 1250 m, and (i) 1500 m. Table shows curve fit coefficients and r^2 value. Tangential winds in m s^{-1} at (b) 275 m, (d) 750 m, (f) 1000 m, (h) 1250 m, and (j) 1500 m from dropsondes (solid red circles) and gradient winds from HDOB data (short-dashed green curve) and dropsonde data (long-dashed blue line). The solid black vertical lines in (b,d,f,h,j) denote the mean RMW.

APPENDIX D: TYPHOON JANGMI GRADIENT WIND BALANCE ANALYSIS

The Typhoon Jangmi gradient wind balance results for the remaining five altitudes (275 m, 500 m, 1000 m, 1250 m, and 1500 m) from the discussion in Chapter IV, Section A3 are shown below in Figure 40 a-j.

(a)

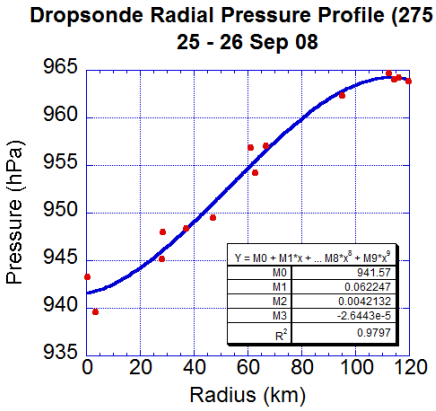

(b)

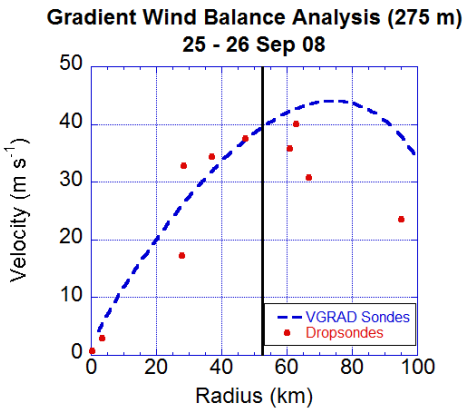

(c)

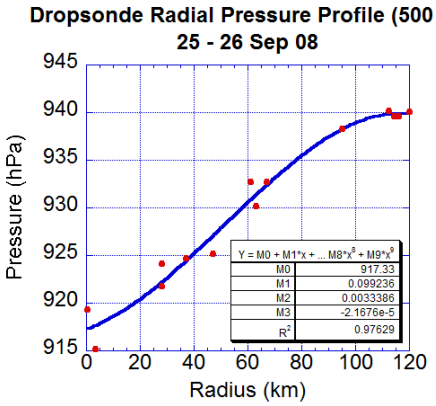

(d)

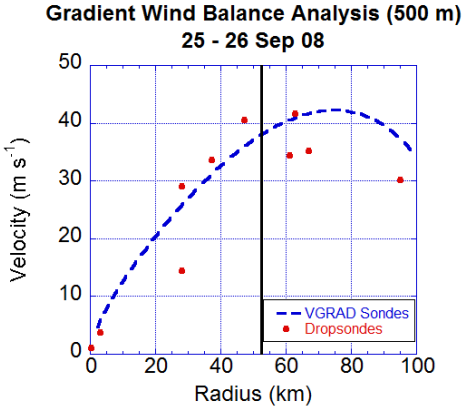

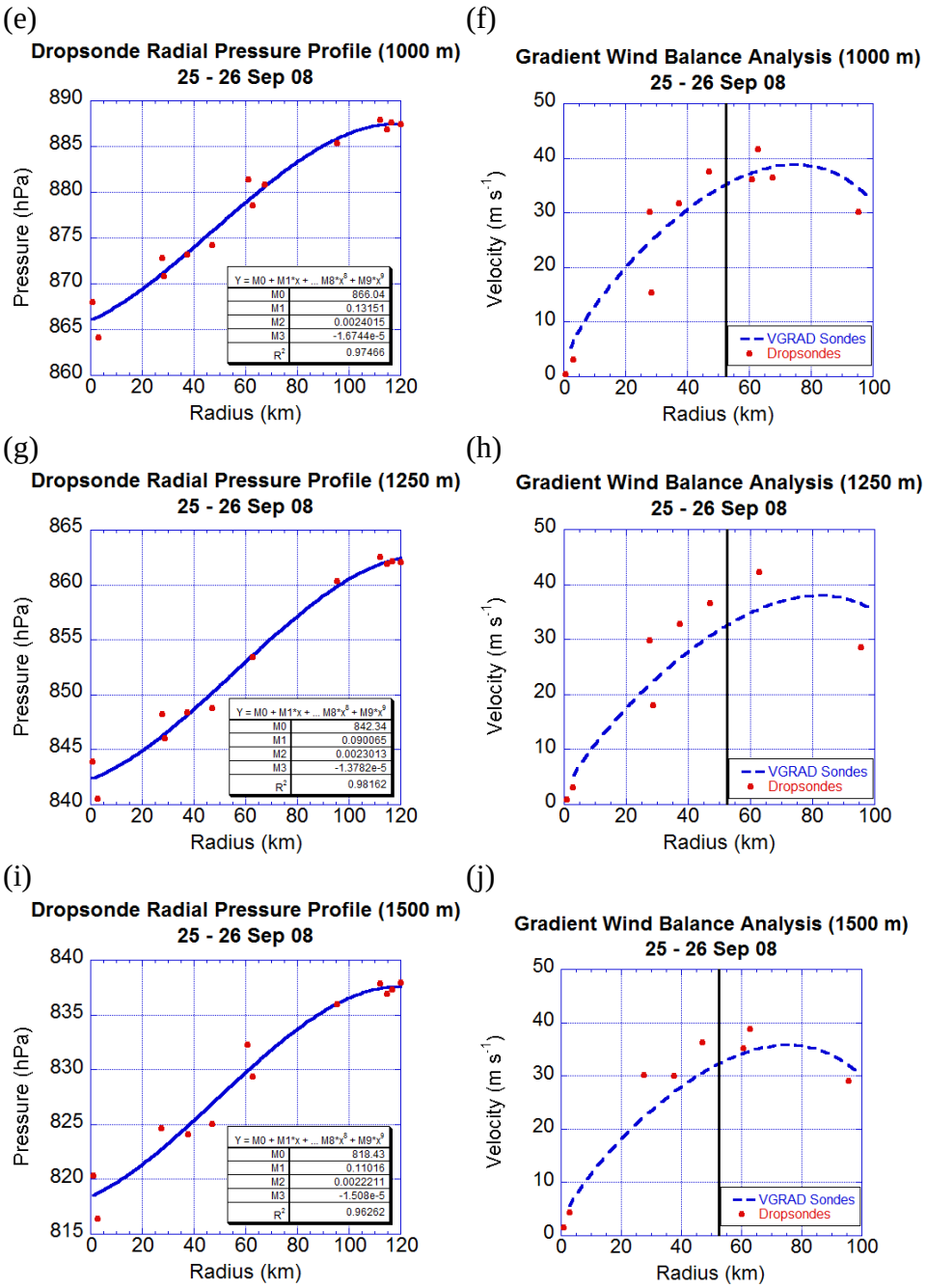

Figure 40. Typhoon Jangmi observed pressure (hPa) from dropsondes (solid red circles) and 3rd degree polynomial fit (solid blue line) at (a) 275 m, (c) 500 m, (e) 1000 m, (g) 1250 m, and (i) 1500 m. Table shows curve fit coefficients and r^2 value. Tangential winds in m s^{-1} at (b) 275 m, (d) 750 m, (f) 1000 m, (h) 1250 m, and (j) 1500 m from dropsondes (solid red circles) and gradient winds from HDOB data (short-dashed green curve) and dropsonde data (long-dashed blue line). The solid black vertical lines in (b,d,f,h,j) denote the mean RMW.

APPENDIX E: SUPERTYPHOON JANGMI GRADIENT WIND BALANCE ANALYSIS

The Supertyphoon Jangmi gradient wind balance results for the remaining five altitudes (275 m, 750 m, 1000 m, 1250 m, and 1500 m) from the discussion in Chapter IV, Section A3 are shown below in Figure 41 a-j.

(a)

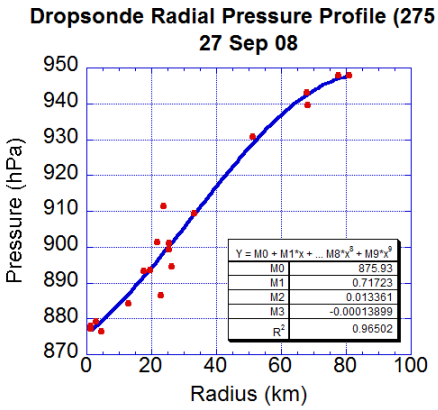

(b)

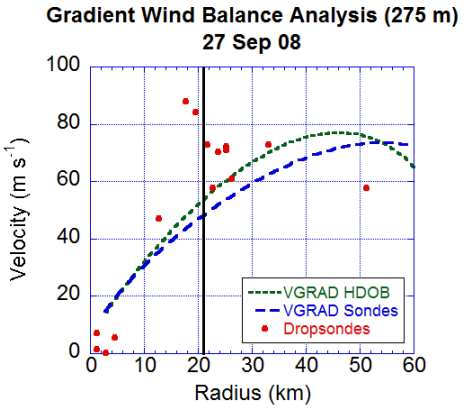

(c)

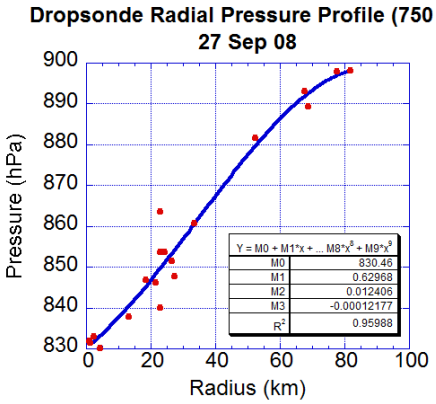

(d)

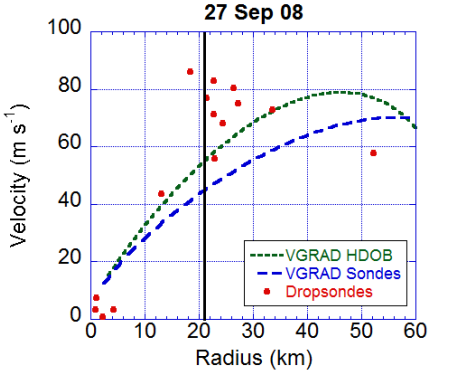

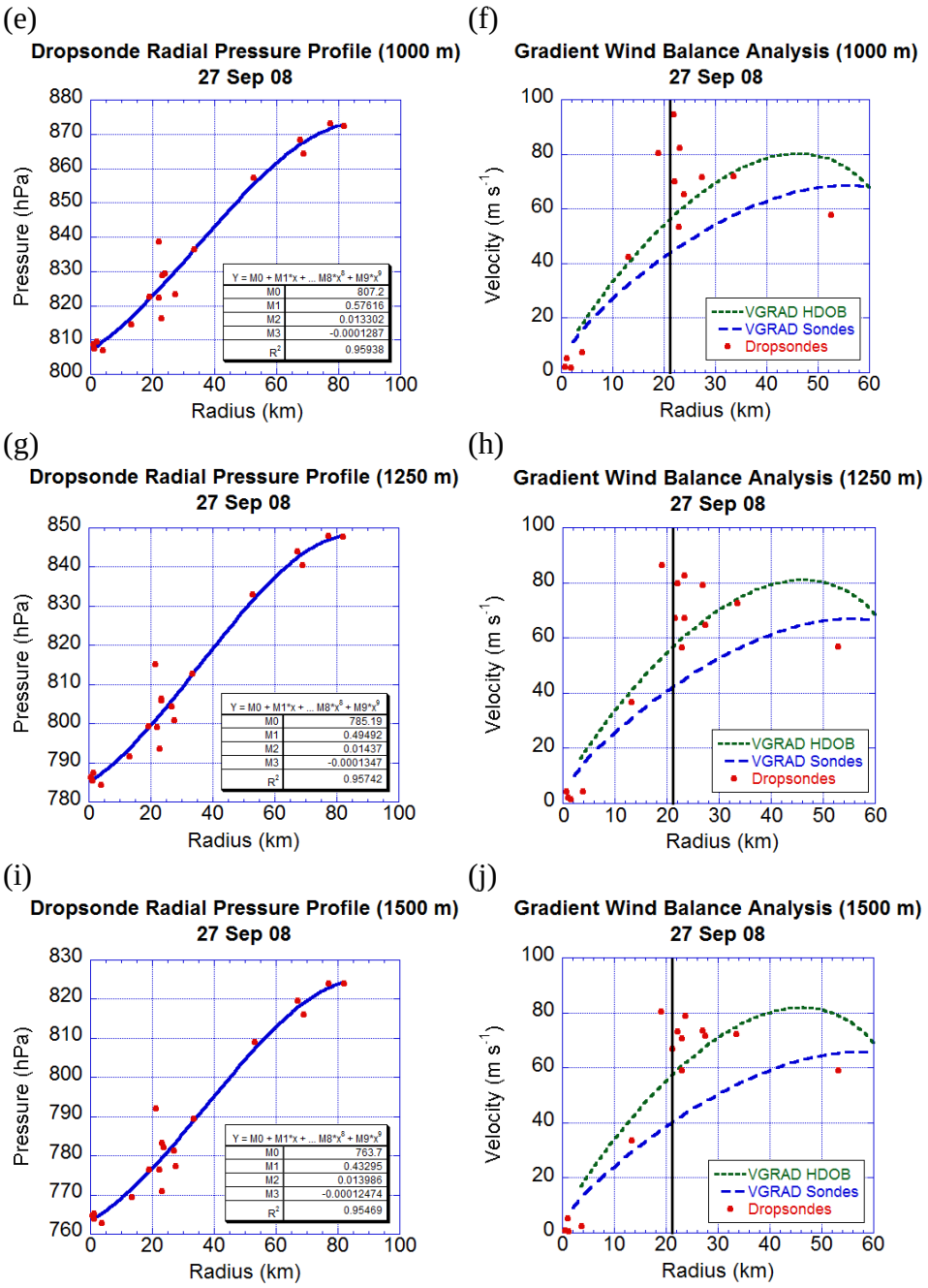

Figure 41. Supertyphoon Jangmi observed pressure (hPa) from dropsondes (solid red circles) and 3rd degree polynomial fit (solid blue line) at (a) 275 m, (c) 750 m, (e) 1000 m, (g) 1250 m, and (i) 1500 m. Table shows curve fit coefficients and r^2 value. Tangential winds in m s^{-1} at (b) 275 m, (d) 750 m, (f) 1000 m, (h) 1250 m, and (j) 1500 m from dropsondes (solid red circles) and gradient winds from HDOB data (short-dashed green curve) and dropsonde data (long-dashed blue line). The solid black vertical lines in (b,d,f,h,j) denote the mean RMW.

APPENDIX F: TS JANGMI EYEWALL DROPSONDES

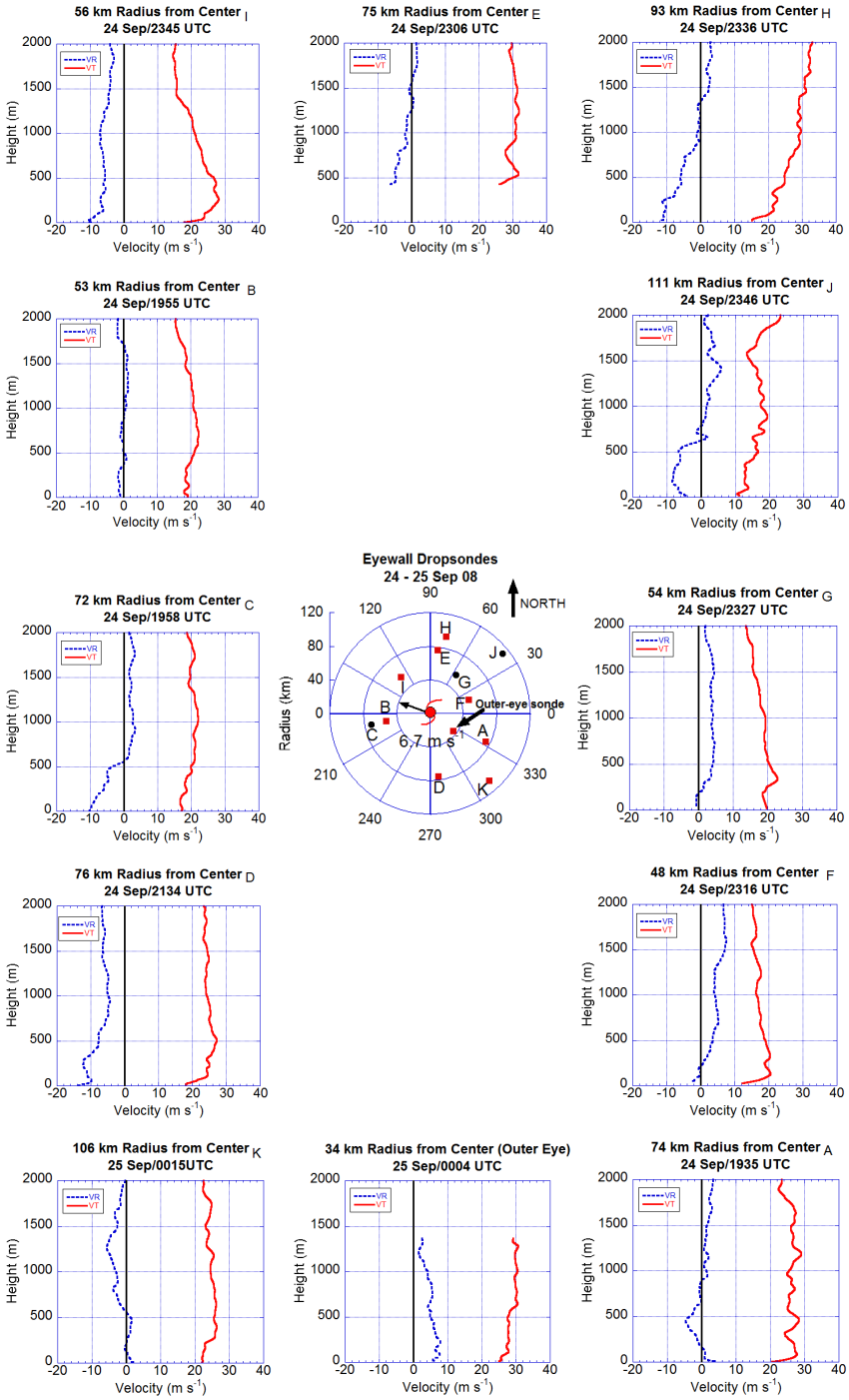

Figure 42. TS Jangmi tangential (solid red line) and radial winds (dotted blue line) profiles in m s^{-1} for eyewall sondes from 24 – 25 Sep 2008. Dropsonde locations shown in geographic-oriented *R-θ* plot in middle labeled with letters (A - K) according to order of launch placed relative to the storm center.

THIS PAGE INTENTIONALLY LEFT BLANK

APPENDIX G: TYPHOON JANGMI EYEWALL DROPSONDES

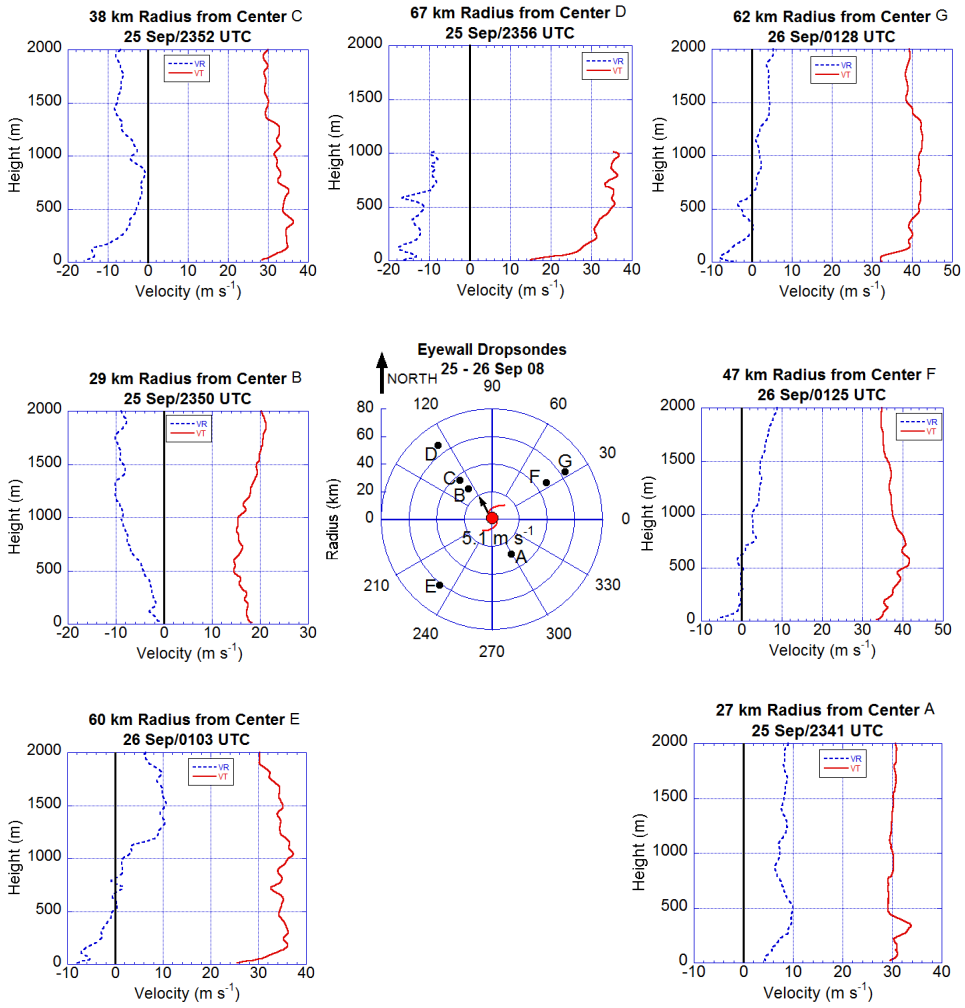

Figure 43. Typhoon Jangmi tangential winds (solid red line) and radial winds (dotted blue line) profiles in units of m s^{-1} for all eyewall dropwindsondes from 25 – 26 Sep 2008. Dropsonde locations shown in geographic-oriented R-θ plot in middle of page are labeled with letters (A - G) according to order of launch and placed in approximate location relative to the storm center. The dropsonde altitudes are all at or near the surface.

THIS PAGE LEFT INTENTIONALLY BLANK

APPENDIX H: SUPERTYPHOON JANGMI EYEWALL DROPSONDES

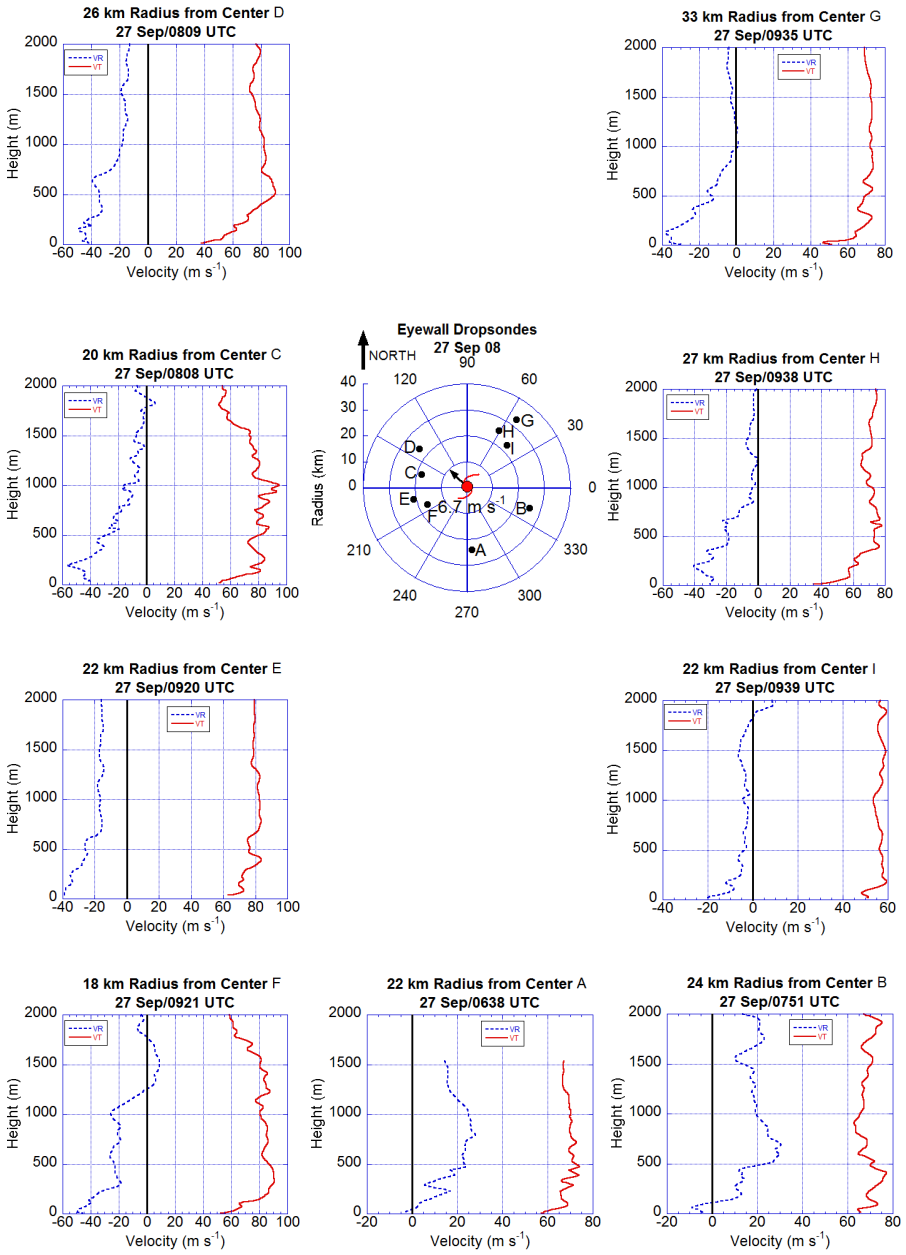

Figure 44. Supertyphoon Jangmi tangential winds (solid red line) and radial winds (dotted blue line) profiles in m s^{-1} for all eyewall dropwindsondes on 27 September 2008. Dropsonde locations shown in geographic-oriented R-θ plot in middle of page are labeled with letters (A - I) according to order of launch and placed in approximate location relative to the storm center. The dropsonde altitudes are all at or near the surface.

THIS PAGE LEFT INTENTIONALLY BLANK

APPENDIX I: HURRICANE GEORGES GRADIENT WIND BALANCE ANALYSIS

The gradient wind balance results for the remaining five altitudes (275 m, 500 m, 1000 m, 1250 m, and 1500 m) from the discussion in Chapter IV, Section B1 are shown below in Figure 39 a-j.

(a) (b)

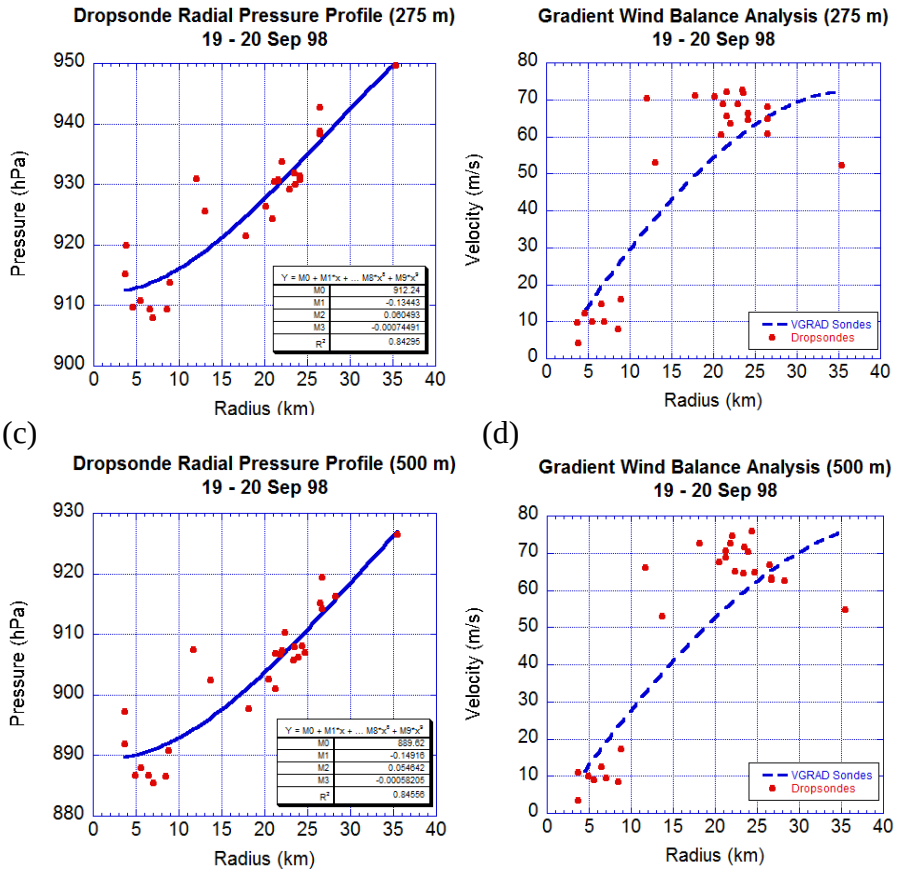

(c) (d)

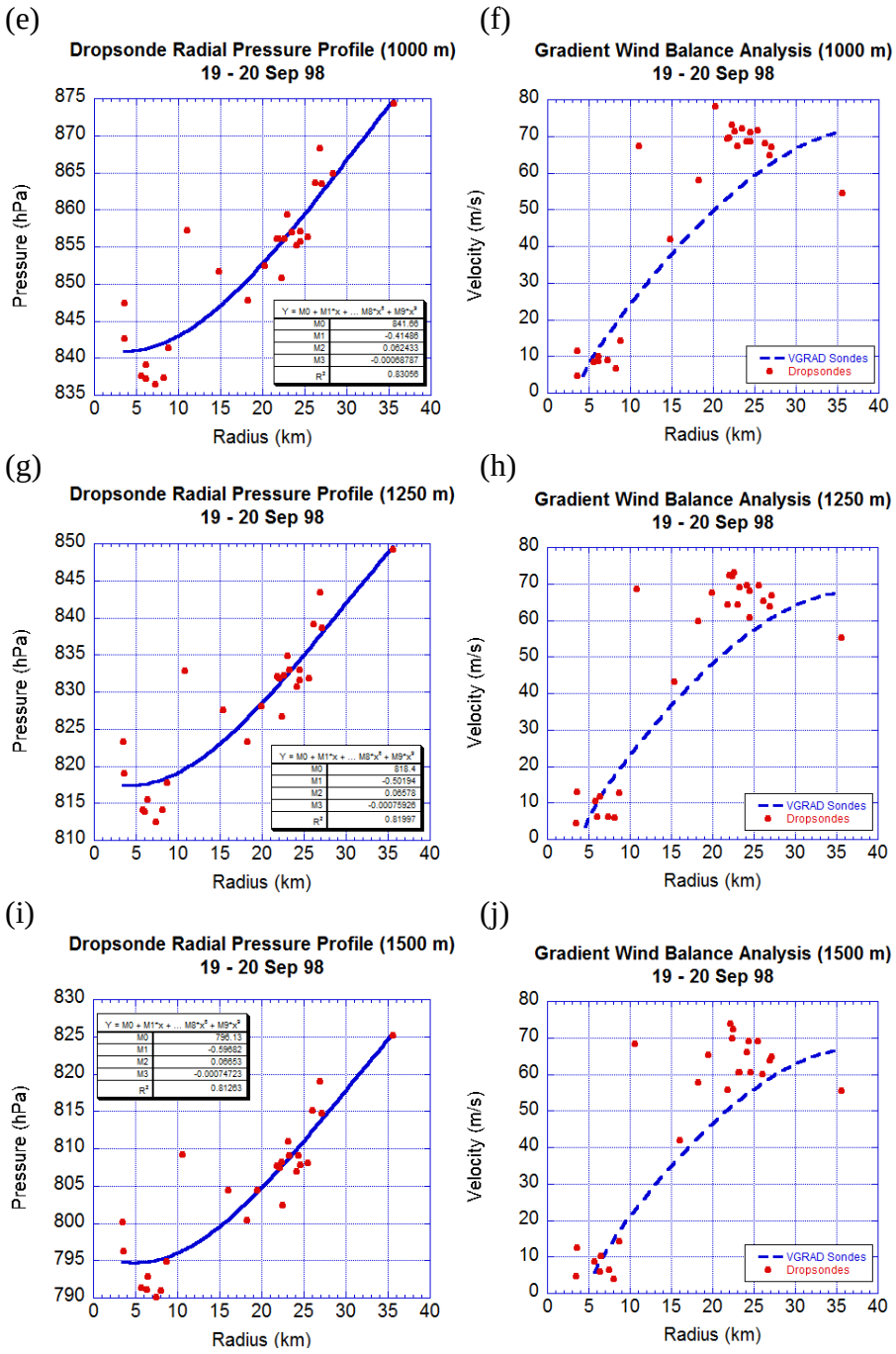

Figure 45. Observed pressure (hPa) from dropsondes (solid red circles) and 3rd degree polynomial fit (solid blue line) at (a) 275 m, (c) 500 m, (e) 1000 m, (g) 1250 m, (i) 1500 m. Table shows curve fit coefficients and r^2 value. Observed tangential winds in m s^{-1} at (b) 275 m, (d) 500 m,(f) 1000 m, (h) 1250 m, (j) 1500 m from dropsondes (solid red circles) and gradient winds based on dropsonde data (dotted blue line).

APPENDIX J: GEORGES EYEWALL DROPSONDES

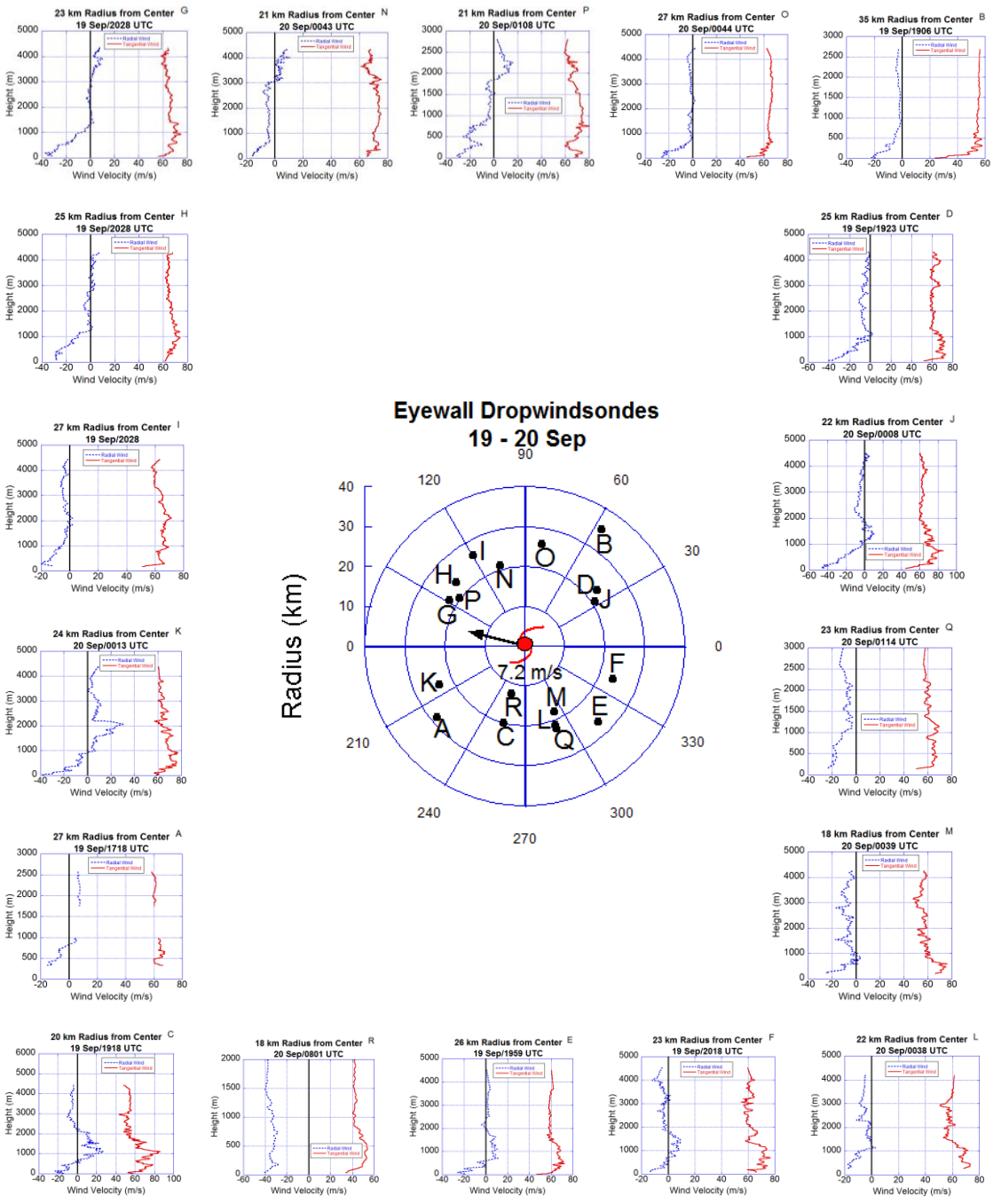

Figure 46. Hurricane Georges tangential (solid red line) and radial (dotted blue line) wind profiles of eyewall dropsondes from 19 – 20 Sep 1998. Dropsonde locations shown in geographic-oriented *R*-θ plot in middle. Dropsondes listed in order of launch via letters (A - R). Sondes placed in approximate location relative to the storm center (red tropical storm symbol). Solid black line shows zero line.

THIS PAGE INTENTIONALLY LEFT BLANK

APPENDIX K: DEEP CONVECTION IN SUPERTYPHOON JANGMI

(a)

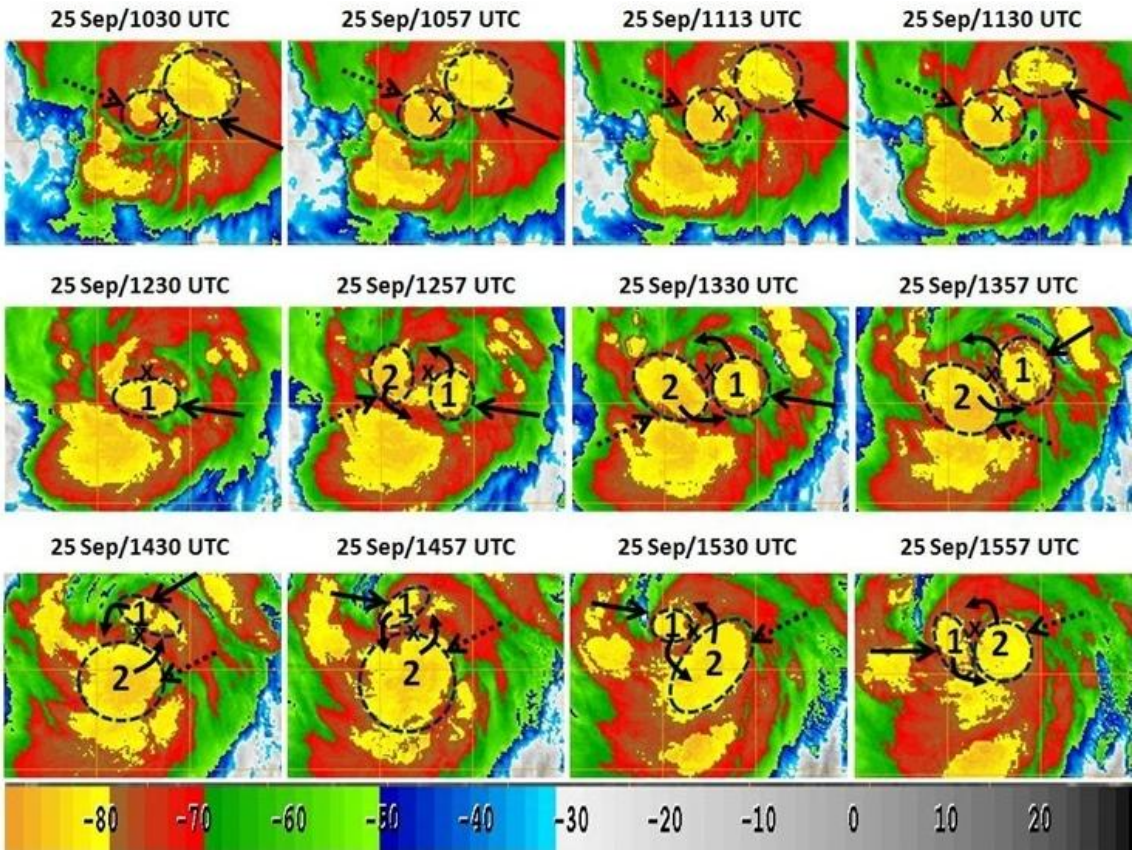

(b)

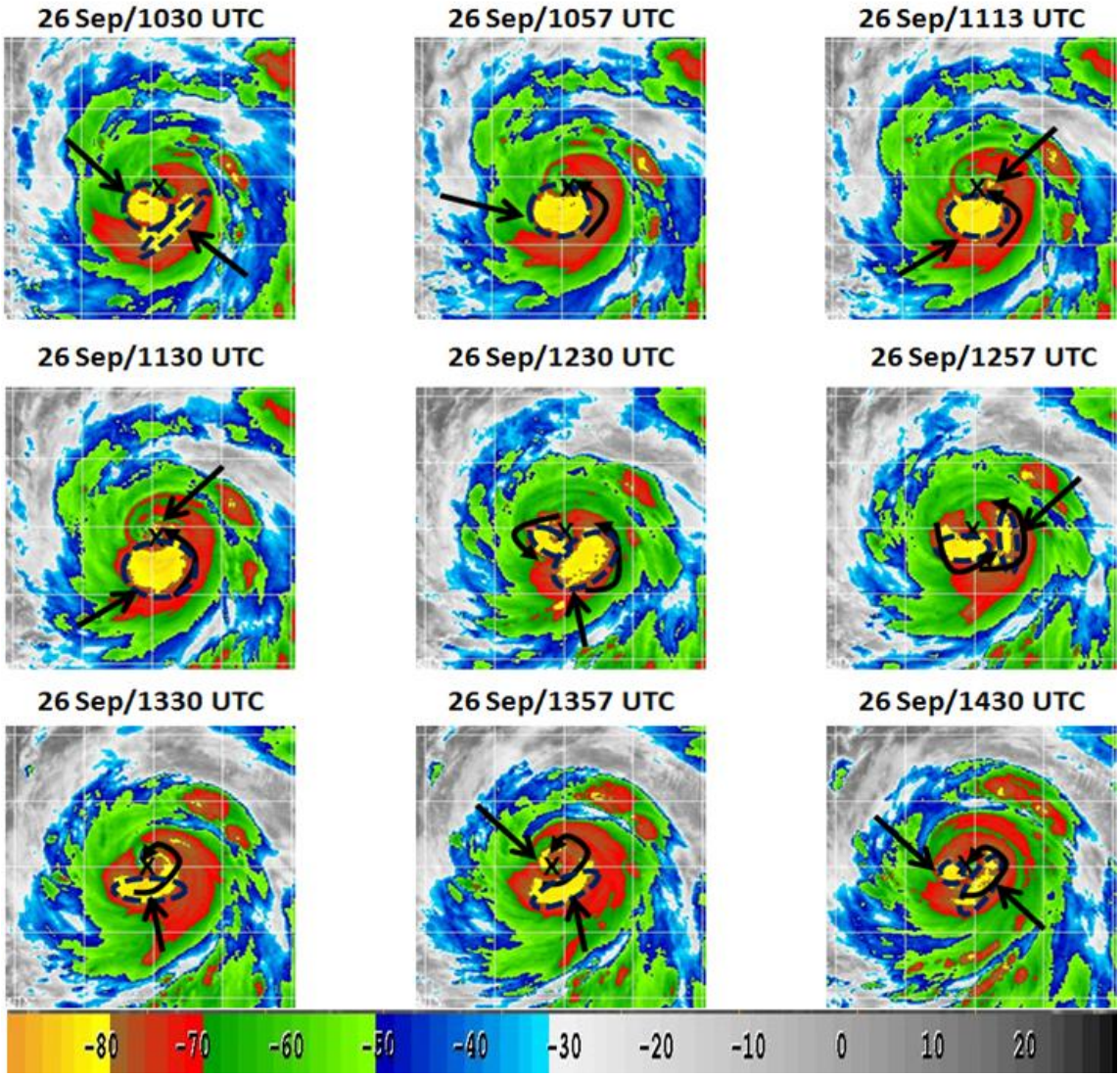

Figure 47. Series of 1-km MTSAT infrared imagery depicting deep convective clouds in Typhoon Jangmi from (a) 1030 UTC – 1557 UTC 25 September 2008 and (b) 1030 UTC – 1430 UTC 26 September 2008. Dashed blue circles indicate deep convection and its approximate areal extent and shape. Storm center shown with black "**X**." Note that cells #1 and #2 in (a) begin rotating counterclockwise at 0257 UTC 25 September as they spiral inward toward the center and rotate over ¾ of a revolution. The color bar at bottom of plot associates cloud-top temperatures with various colors. The lowest cloud-top temperatures are shown with shades of red and yellow (-70°C to -90°C). Imagery courtesy of Naval Research Laboratory, Monterey, CA.

APPENDIX L: DEEP CONVECTION IN HURRICANE GEORGES

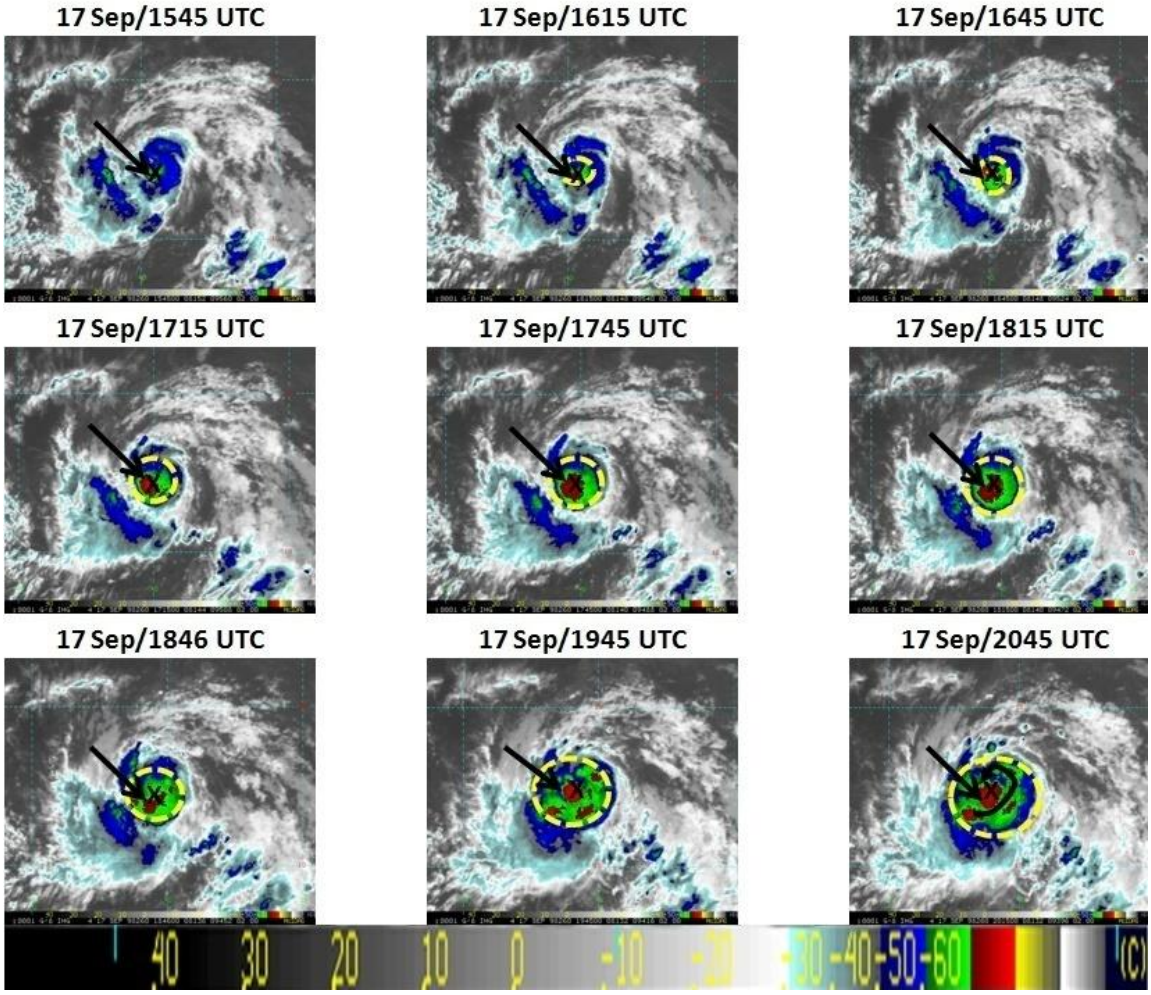

Figure 48. Series of NOAA GOES-8 4 km infrared imagery deep convective clouds in Hurricane Georges from 1545 UTC – 2045 UTC 17 September. Dashed yellow circles indicate deep convection and its approximate areal extent and shape. NHC best-track storm center shown with black "**X**." Note in the last panel at 17 Sep 2045 UTC the inward spiral of the deep clouds. The color bar at bottom of plot associates cloud-top temperatures with various colors. The coldest cloud-top temperatures are shown with shades of red and yellow (-70°C to -90°C). Imagery is courtesy of John Knaff of NOAA/NESDIS/CIRA, Fort Collins, CO.

THIS PAGE LEFT INTENTIONALLY BLANK

APPENDIX M: STUDY OF ASYMMETRY IN TS JANGMI

The standard deviation analysis of the HDOB extrapolated sea-level pressure that is discussed in Chapter IV Section A2b is shown below in Table 3. Prior to showing the standard deviation (σ) and variance (σ^2) analysis of the extrapolated SLP below, the mathematical definitions are provided below for the reader:

$$\sigma = \sqrt{\frac{\sum\left(x-\bar{x}\right)^2}{n-1}},$$

where x = individual observation, $\bar{x}$ = mean of all the observations, and n = total # of observations.

$$\sigma^2 = \frac{\sum\left(x-\bar{x}\right)^2}{n-1}$$

Table 3. Results of the standard deviation and variance computations for the quadrant curve fits of extrapolated SLP from the HDOB flight-level data in TS Jangmi:

QUADRANT	STANDARD DEVIATION.	VARIANCE
ESE	3.7 hPa	13.4 hPa^2
WSW	3.6 hPa	12.9 hPa^2
SSE	4.8 hPa	23.3hPa^2
NE	5.1 hPa	25.9 hPa^2
NW	5.2 hPa	27.3 hPa^2
SE	4.3 hPa	18.6 hPa^2
ALL	4.6 hPa	20.8 hPa^2

The quadrant-by quadrant analysis of the gradient wind speed is carried out using the HDOB extrapolated sea-level pressure (Figures 49a,c,e,g,i,k) to obtain the required pressure for computing the gradient wind curves in Figures 49 b,d,f,h,j,l below). These results are discussed in Chapter IV, Section A3.

The quadrant-by quadrant analysis of the geopotential height, extrapolated sea-level pressure, and flight-level tangential wind speed is shown below in Figures 50a-f, Figures 51a-f, and Figures 52a-f, respectively. These results are discussed in Chapter IV, Section A2b.

(a)

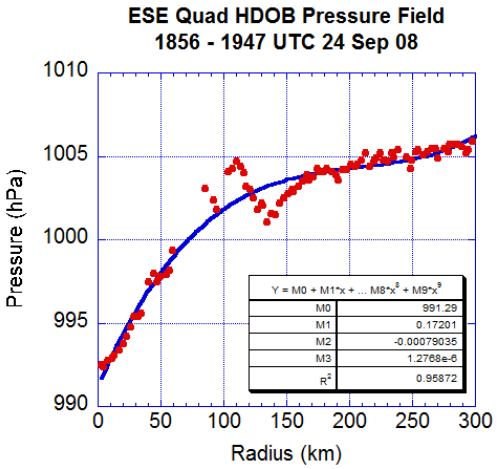

(b)

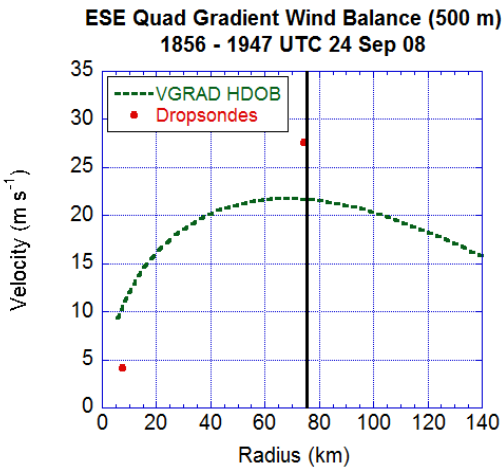

(c)

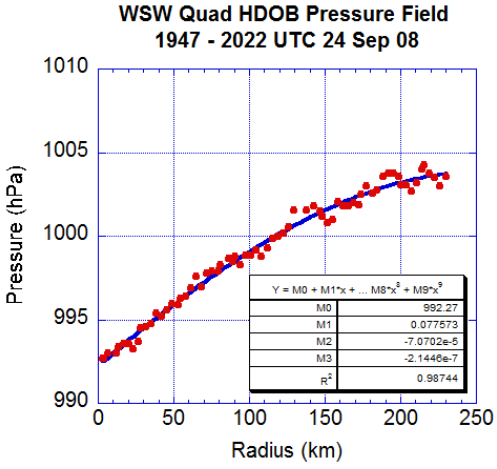

(d)

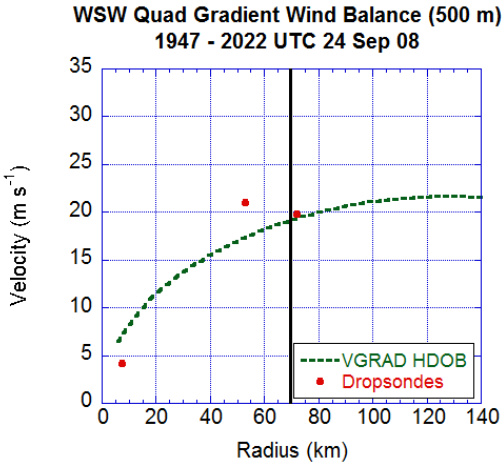

(e)

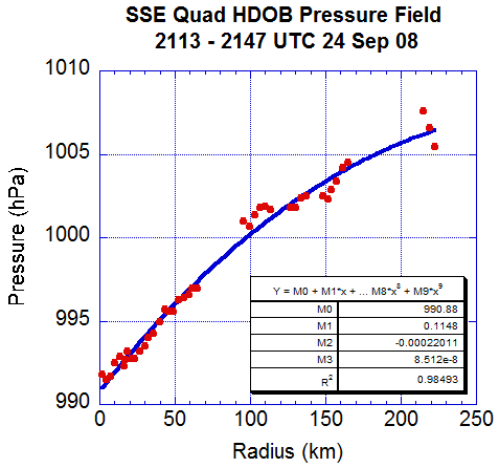
SSE Quad HDOB Pressure Field
2113 - 2147 UTC 24 Sep 08
Pressure (hPa)
Radius (km)
Y = M0 + M1*x + ... M8*x^8 + M9*x^9
M0 990.88
M1 0.1148
M2 -0.00022011
M3 8.512e-8
R^2 0.98493

(f)

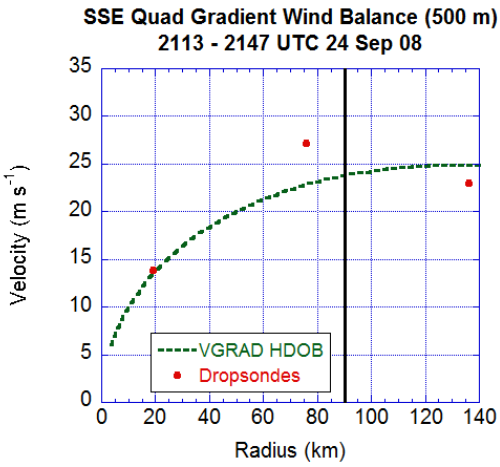
SSE Quad Gradient Wind Balance (500 m)
2113 - 2147 UTC 24 Sep 08
Velocity (m s-1)
Radius (km)
VGRAD HDOB
Dropsondes

(g)

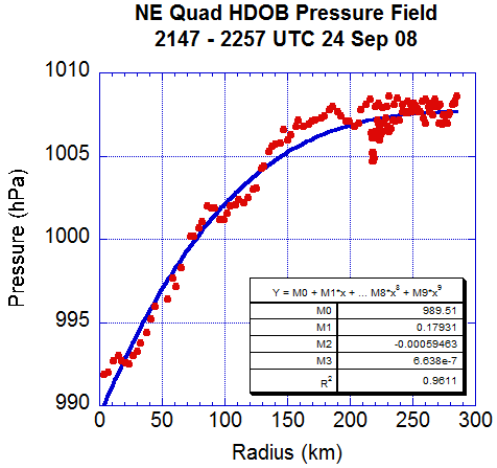
NE Quad HDOB Pressure Field
2147 - 2257 UTC 24 Sep 08
Pressure (hPa)
Radius (km)
Y = M0 + M1*x + ... M8*x^8 + M9*x^9
M0 989.51
M1 0.17931
M2 -0.00059463
M3 6.638e-7
R^2 0.9611

(h)

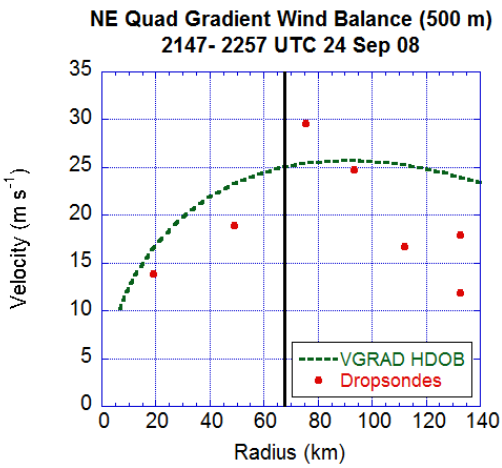
NE Quad Gradient Wind Balance (500 m)
2147- 2257 UTC 24 Sep 08
Velocity (m s-1)
Radius (km)
VGRAD HDOB
Dropsondes

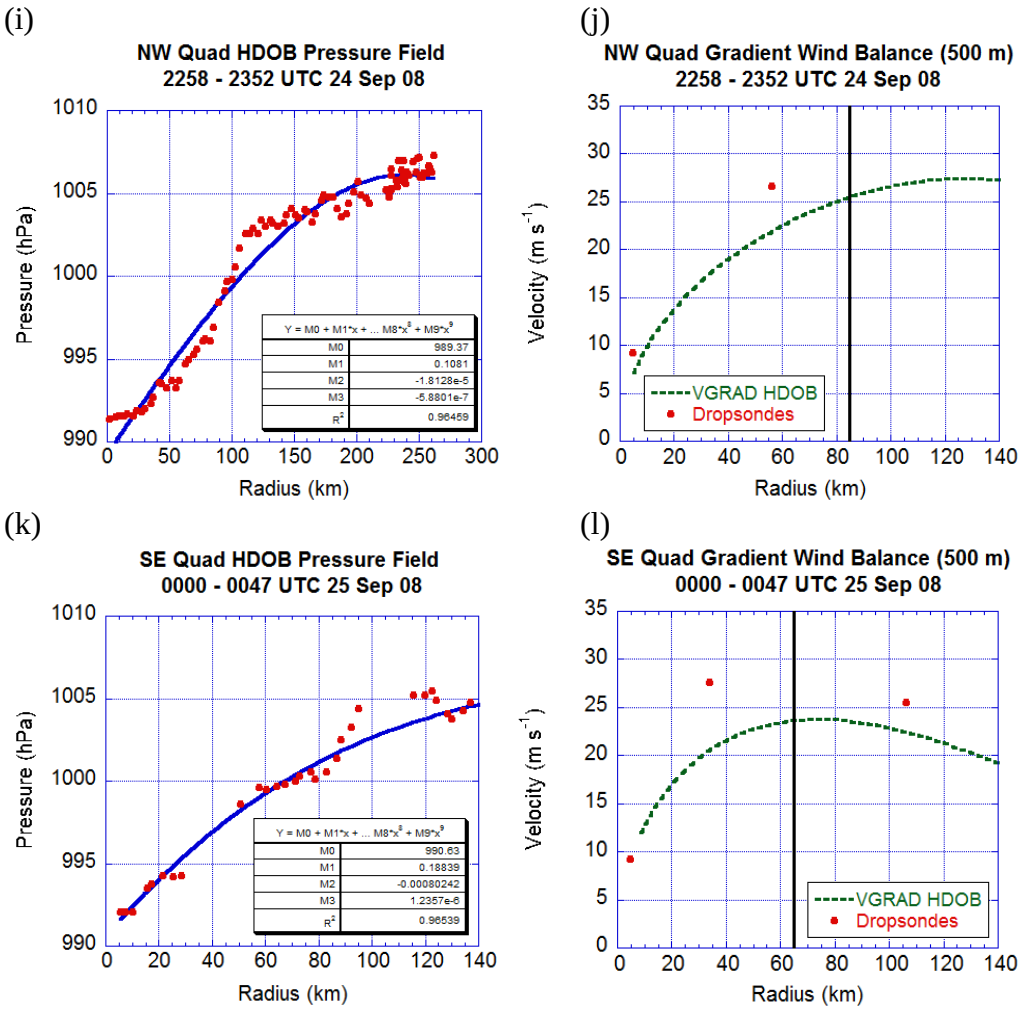

Figure 49. Observed extrapolated SLP (hPa) from HDOB flight-level data (solid red circles) and 3rd degree polynomial fit (solid blue curve) for TS Jangmi using the WC82 centers for (a) ESE Quadrant; (c) WSW Quadrant; (e) SSE Quadrant; (g) NE Quadrant; (i) NW Quadrant; and (k) SE Quadrant. Tables in lower right of (a, c, e, g, i, and k) shows curve fit coefficients and r^2 values. Tangential wind speed in m s^{-1} at 500 m altitude for TS Jangmi from dropsondes (solid red circles) and gradient wind speed in m s^{-1} derived from flight-level HDOB data (short-dashed green curve for (b) ESE Quadrant; (d) WSW Quadrant; (f) SSE Quadrant; (h) NE Quadrant; (j) NW Quadrant; and (l) SE Quadrant. The solid black vertical line denotes the RMW for each quadrant based on the SFMR flight-level data. For more detailed discussion see Chapter IV, Section A3a.

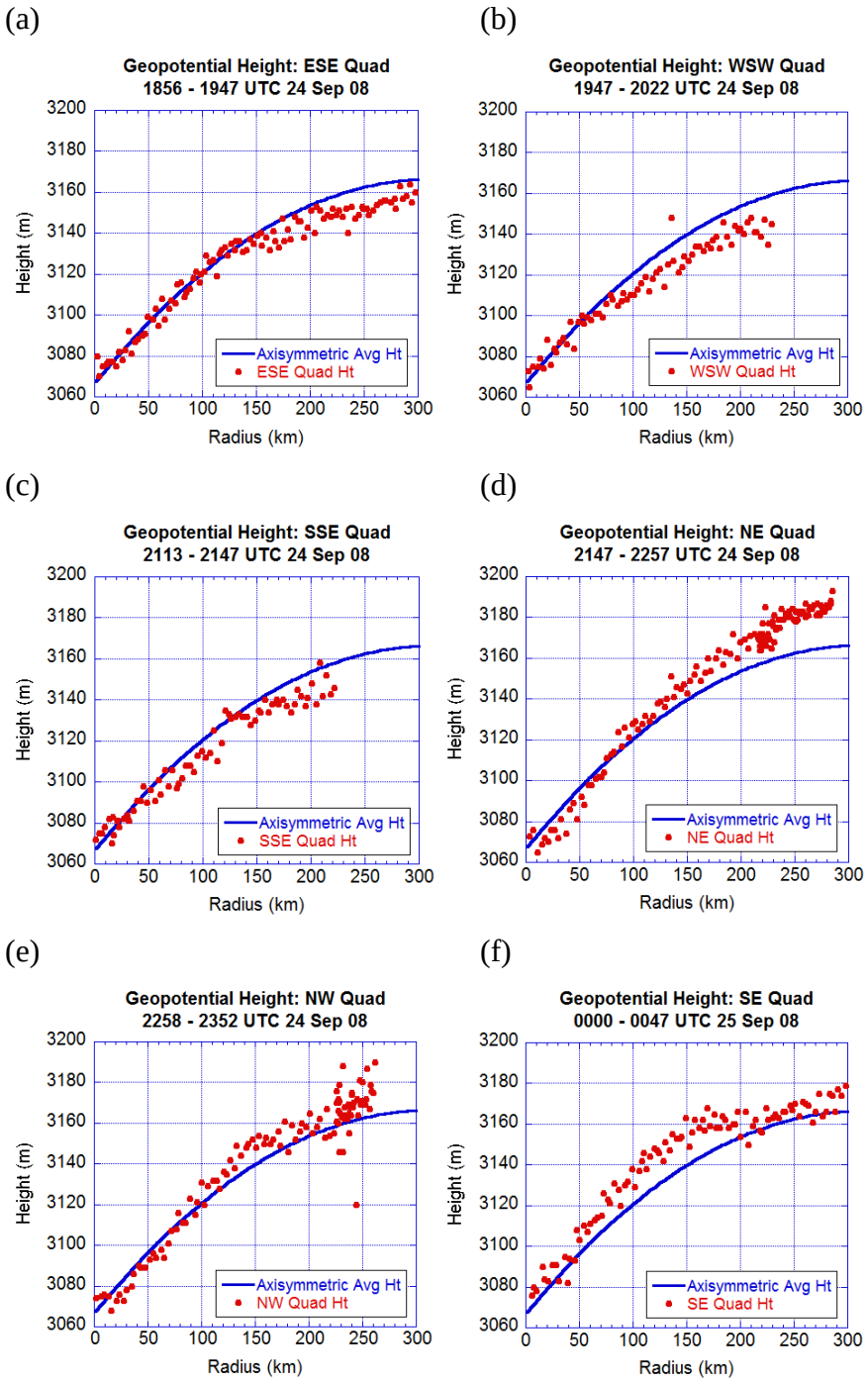

Figure 50. TS Jangmi flight-level geopotential height (red dots) and axisymmetric geopotential height (m) estimated by 3rd-order polynomial (solid blue line) from 1947 UTC 24 Sep to 0047 UTC 25 Sep for (a) ESE quadrant; (b) WSW quadrant; (c) SSE quadrant; (d) NE quadrant; (e) NW quadrant; and (f) SE quadrant.

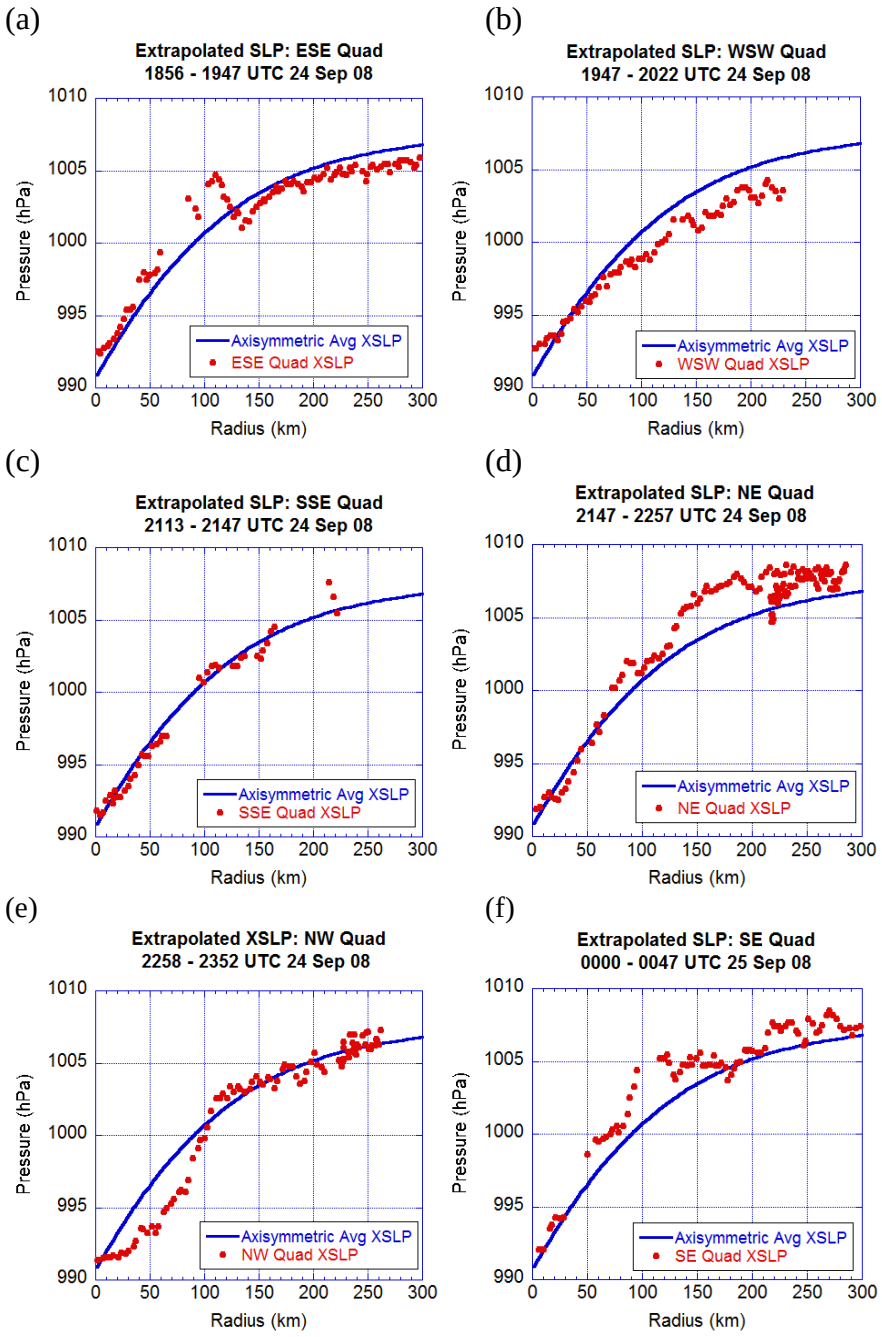

Figure 51. TS Jangmi WC-130J flight-level extrapolated sea-level pressure (red dots) and axisymmetric extrapolated sea-level pressure (hPa) estimated by a 3rd-order polynomial (solid blue line) from 1856 UTC 24 Sep to 0047 UTC 25 Sep using the WC82 centers for (a) ESE quadrant; (b) WSW quadrant; (c) SSE quadrant; (d) NE quadrant; (e) NW quadrant; and (f) SE quadrant.

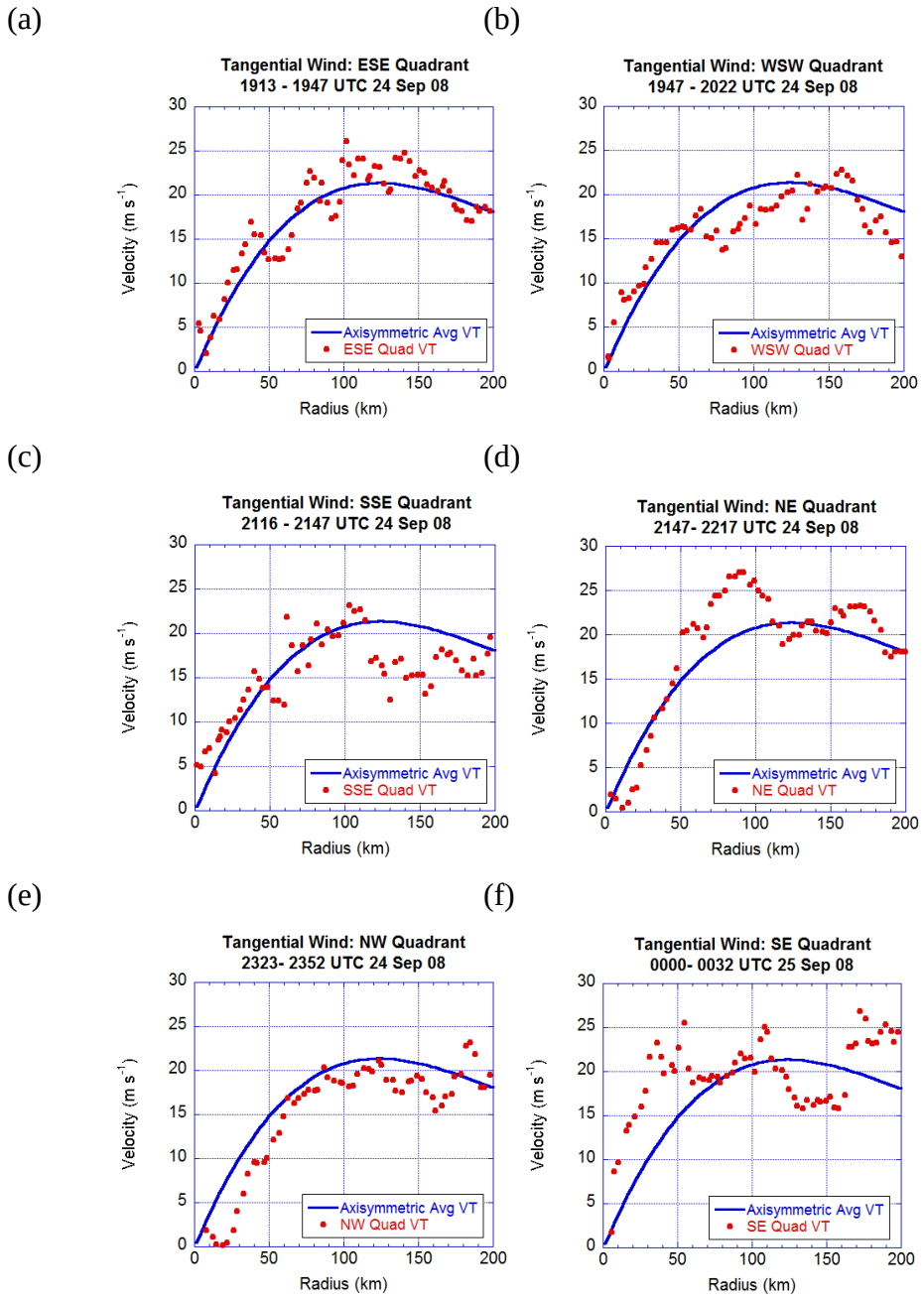

Figure 52. TS Jangmi storm-relative flight-level tangential wind speed in m s^{-1} (red dots) and axisymmetric tangential wind for all quadrants estimated by 3rd-order polynomial (solid blue line) from 2359 UTC 24 Sep to 0045 UTC 25 Sep for (a) ESE quadrant; (b) SW quadrant; (c) NE quadrant; (d) NW quadrant; and (e) SE quadrant. (f) 3rd-order polynomial curve fits of flight-level storm-relative tangential wind by quadrant (orange-SW, green-SE, purple-NE, red-NW, black-ESE) and axisymmetric value (blue).

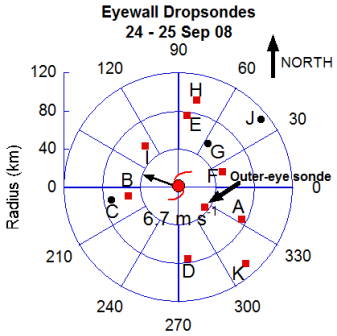

(a) Sonde A: 1933 UTC 24 Sep (b) Sonde A: 1935 UTC 24 Sep

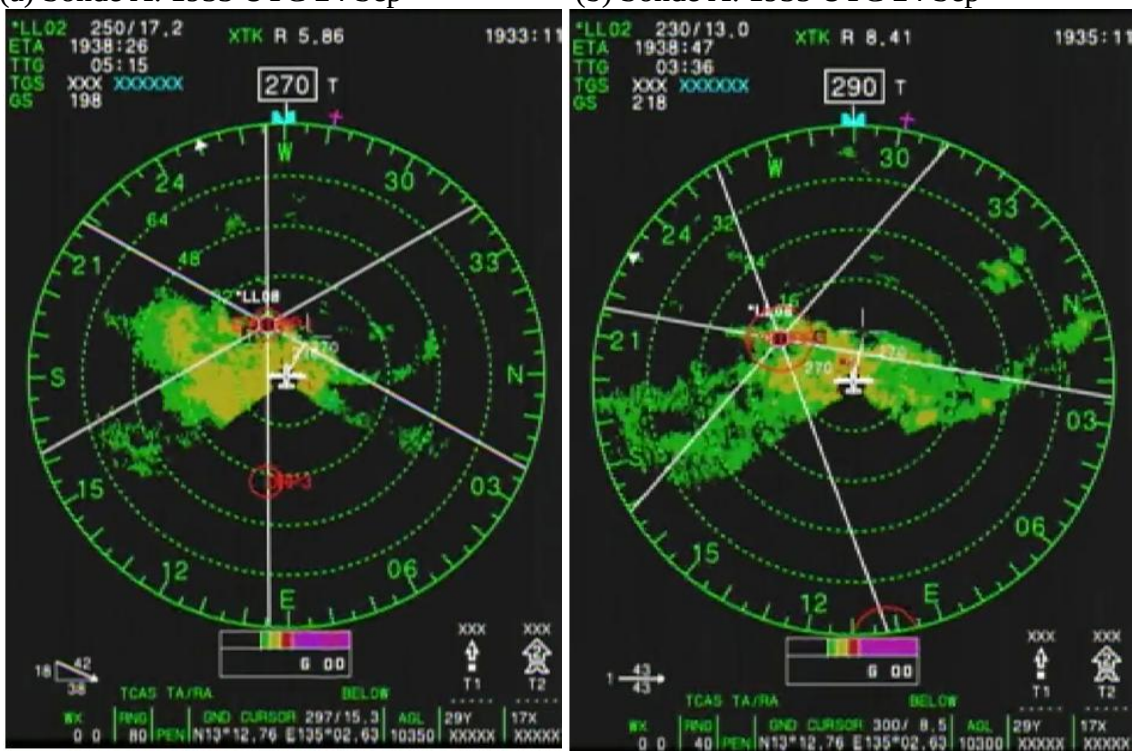

Figure 53. WC-130J aircraft radar imagery for TS Jangmi at (a) 1933 UTC 24 Sep, 2 minutes before Dropsonde A splashed down at the ocean surface; and at (b) 1935 UTC 24 Sep, at the time of the splashdown of Dropsonde A. The exact location of the aircraft is shown with a white plane symbol. Dropsonde A is roughly located near the white aircraft symbol. The storm-relative position of Dropsonde A is shown in the plot at top center as in Figure 15a. There is an area of deep convection located near Dropsonde A shown in (b) just in front and to the left of the aircraft nose. The spacing between the range rings is 8 n mi. The following colors equate to the following radar reflectivity values: Green - > 25 dBZ; Yellow - > 35 dBZ; Red - > 45 dBZ; and Purple - > 55 dBZ.

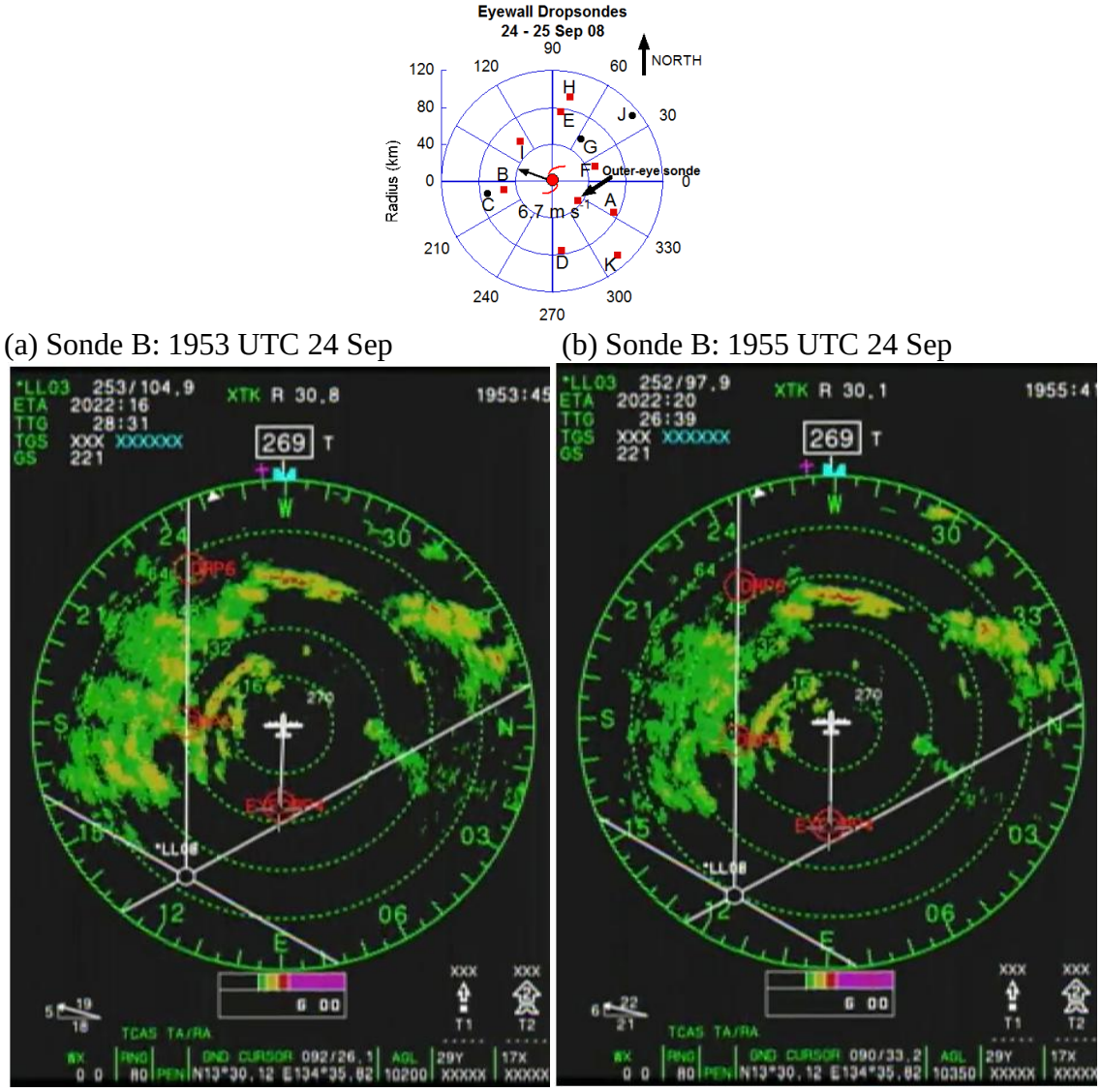

Figure 54. WC-130J aircraft radar imagery for TS Jangmi at (a) 1953 UTC 24 Sep, 2 minutes before Dropsonde B splashed down at the ocean surface; and at (b) 1955 UTC 24 Sep, at the time of the splashdown of Dropsonde B. The exact location of the aircraft is shown with a white plane symbol. Dropsonde B is roughly located near the white aircraft symbol. The storm-relative position of Dropsonde B is shown in the plot at top center as in Figure 15a. There is a lack of convection near the dropsonde in both radar images. The spacing between the range rings is 16 n mi. The following colors equate to the following radar reflectivity values: Green - > 25 dBZ; Yellow - > 35 dBZ; Red - > 45 dBZ; and Purple - > 55 dBZ.

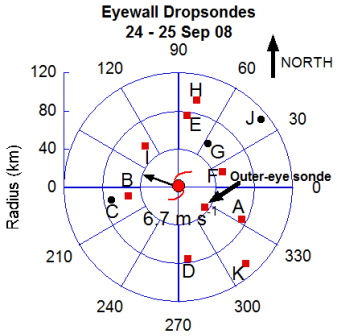

(a) Sonde D: 2132 UTC 24 Sep (b) Sonde D: 2134 UTC 24 Sep

Figure 55. WC-130J aircraft radar imagery for TS Jangmi at (a) 2132 UTC 24 Sep, 2 minutes before Dropsonde D splashed down at the ocean surface; and at (b) 2134 UTC 24 Sep, at the time of the splashdown of Dropsonde D. The exact location of the aircraft is shown with a white plane symbol. Dropsonde D is roughly located near the white aircraft symbol. The storm-relative position of Dropsonde D is shown in the plot at top center as in Figure 15a. The dropsonde is located in an area of stratiform precipitation in both radar images. The spacing between the range rings is 16 n mi. The following colors equate to the following radar reflectivity values: Green - > 25 dBZ; Yellow - > 35 dBZ; Red - > 45 dBZ; and Purple - > 55 dBZ.

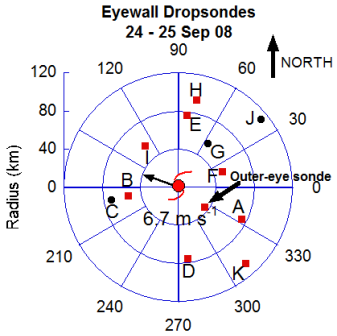

(a) Sonde E: 2303 UTC 24 Sep (b) Sonde E: 2306 UTC 24 Sep

Figure 56. WC-130J aircraft radar imagery for TS Jangmi at (a) 2303 UTC 24 Sep, ~ 2 minutes before Dropsonde E splashed down at the ocean surface; and at (b) 2306 UTC 24 Sep, at the time of the splashdown of Dropsonde E. The exact location of the aircraft is shown with a white plane symbol. Dropsonde E is roughly located near the white aircraft symbol. The storm-relative position of Dropsonde E is shown in the plot at top center as in Figure 15a. There is only an area of weak convection near dropsonde in both radar images. The spacing between the range rings is 32 n mi. The following colors equate to the following radar reflectivity values: Green - > 25 dBZ; Yellow - > 35 dBZ; Red - > 45 dBZ; and Purple - > 55 dBZ.

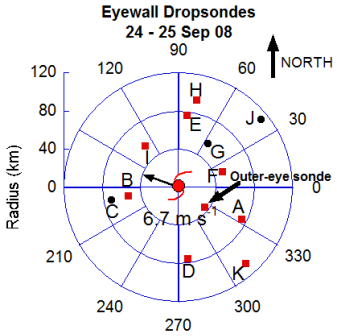

(a) Sonde F: 2315 UTC 24 Sep (b) Sonde F: 2316 UTC 24 Sep

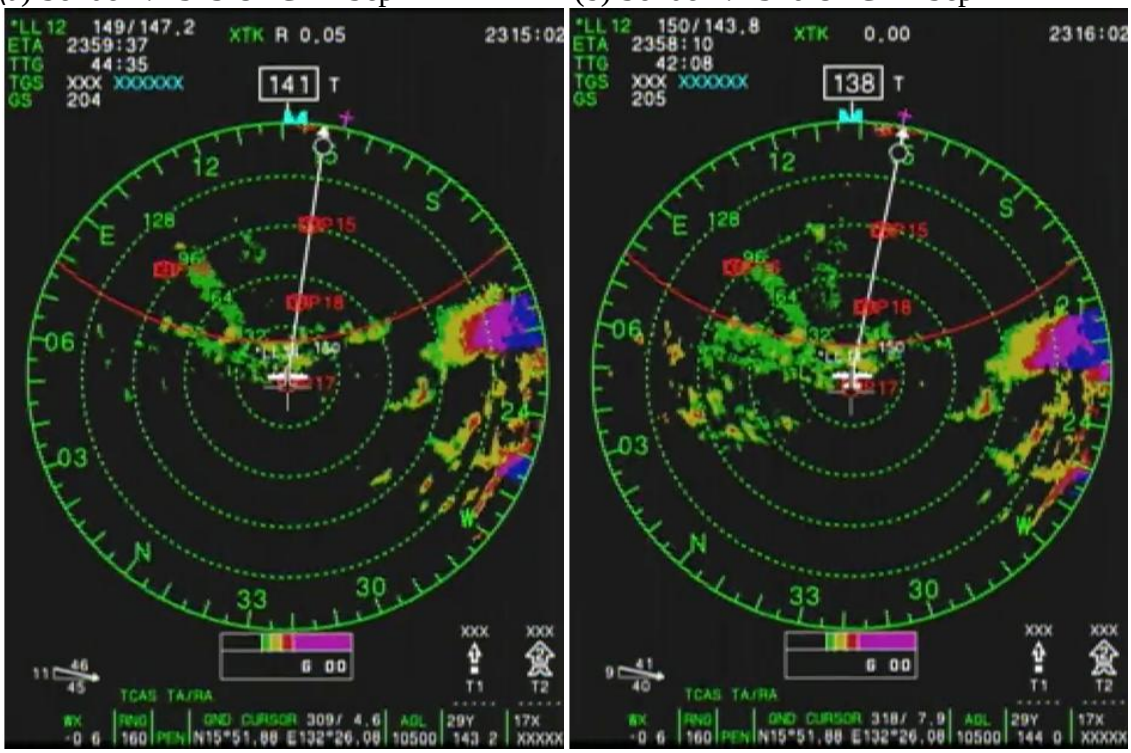

Figure 57. WC-130J aircraft radar imagery for TS Jangmi at (a) 2315 UTC 24 Sep, 1 minute before Dropsonde F splashed down at the ocean surface; and at (b) 2316 UTC 24 Sep, at the time of the splashdown of Dropsonde F. The exact location of the aircraft is shown with a white plane symbol. Dropsonde F is roughly located roughly near the white aircraft symbol. The storm-relative position of Dropsonde F is shown in the plot at top center as in Figure 15a. There is only an area of weak convection near dropsonde in both radar images. The spacing between the range rings is 32 n mi. The following colors equate to the following radar reflectivity values: Green - > 25 dBZ; Yellow - > 35 dBZ; Red - > 45 dBZ; and Purple - > 55 dBZ.

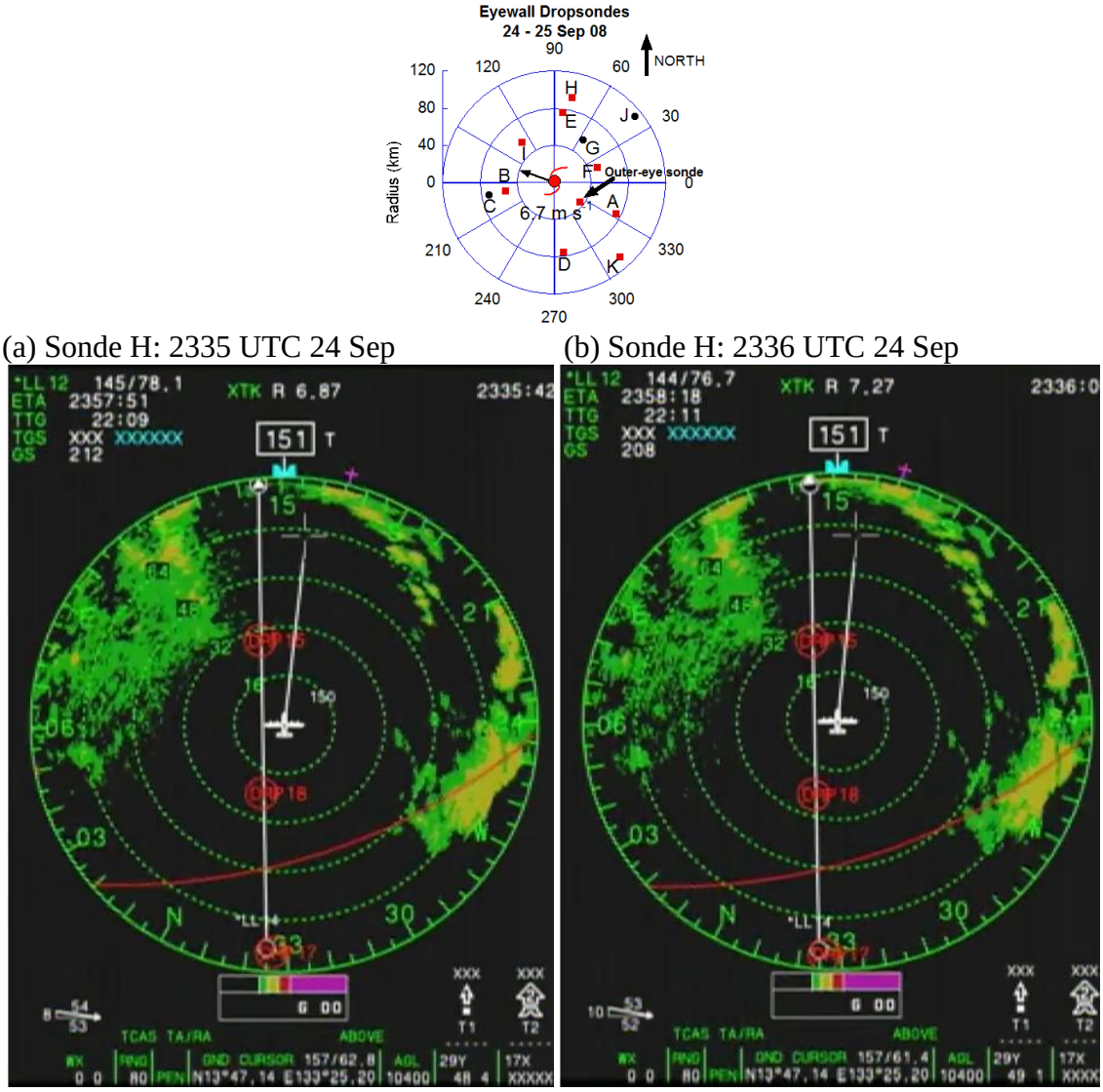

Figure 58. WC-130J aircraft radar imagery for TS Jangmi at (a) 2335 UTC 24 Sep, 18 seconds before Dropsonde H splashed down at the ocean surface; and at (b) 2336 UTC 24 Sep, at the time of the splashdown of Dropsonde H. The exact location of the aircraft is shown with a white plane symbol. Dropsonde H is roughly located near the white aircraft symbol. The storm-relative position of Dropsonde H is shown in the plot at top center as in Figure 15a. There is a complete lack of convection in both radar images. The spacing between the range rings is 16 n mi. The following colors equate to the following radar reflectivity values: Green - > 25 dBZ; Yellow - > 35 dBZ; Red - > 45 dBZ; and Purple - > 55 dBZ.

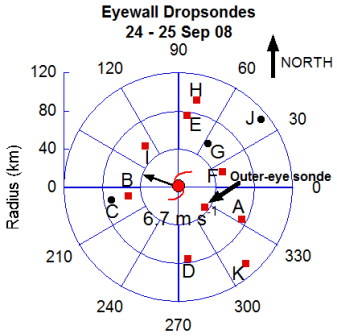

(a) Sonde I: 2343 UTC 24 Sep (b) Sonde I: 2345 UTC 24 Sep

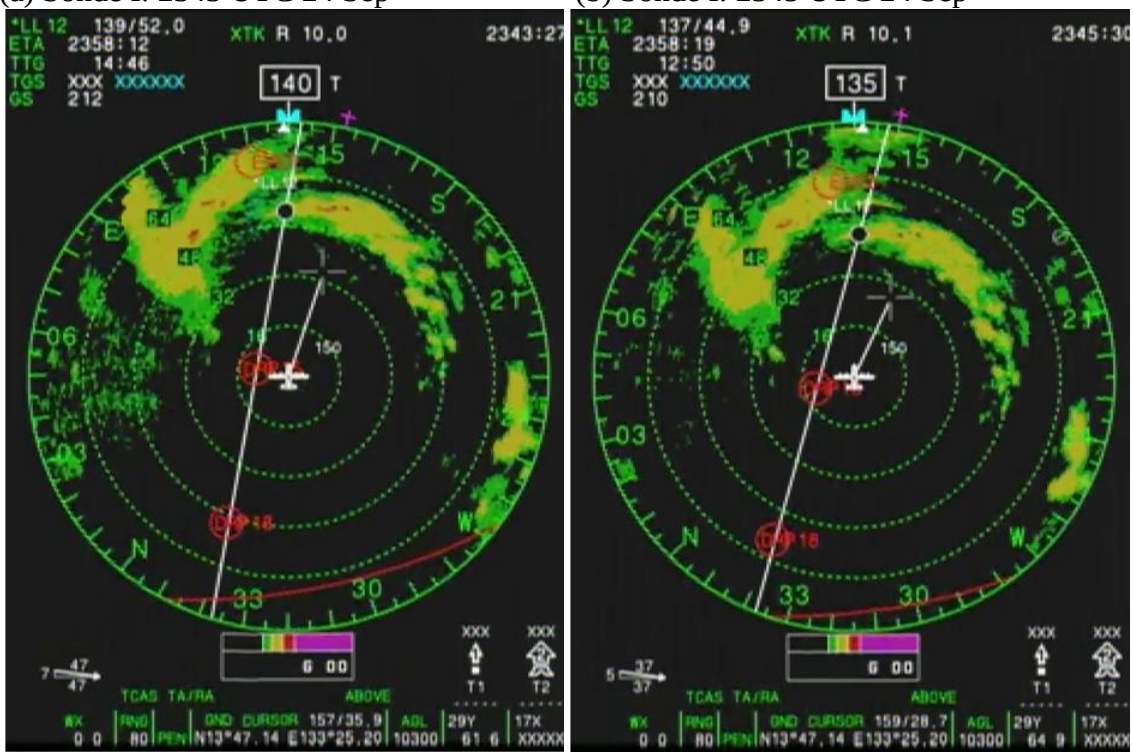

Figure 59. WC-130J aircraft radar imagery for TS Jangmi at (a) 2343 UTC 24 Sep, ~ two minutes before Dropsonde I splashed down at the ocean surface; and at (b) 2345 UTC 24 Sep, at the time of the splashdown of Dropsonde I. The exact location of the aircraft is shown with a white plane symbol. Dropsonde I is roughly located near the white aircraft symbol. The storm-relative position of Dropsonde I is shown in the plot at top center as in Figure 15a. There is a complete lack of convection in both radar images. The spacing between the range rings is 16 n mi. The following colors equate to the following radar reflectivity values: Green - > 25 dBZ; Yellow - > 35 dBZ; Red - > 45 dBZ; and Purple - > 55 dBZ.

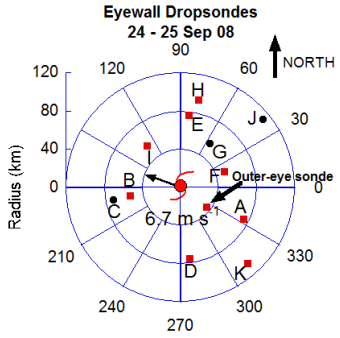

(a) Outer-Eye Sonde: 0002 UTC 25 Sep (b) Outer-Eye Sonde: 0004 UTC 25 Sep

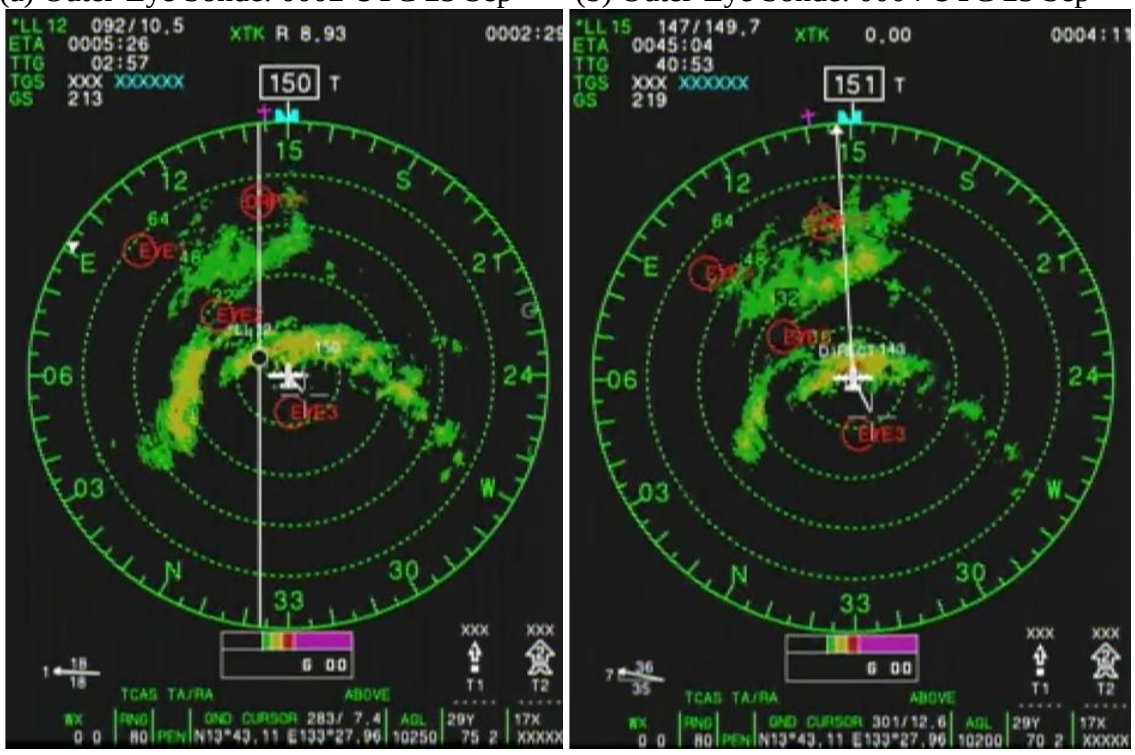

Figure 60. WC-130J aircraft radar imagery for TS Jangmi at (a) 0002 UTC 25 Sep, ~ two minutes before the outer-eye dropsonde splashed down at the ocean surface; and at (b) 0004 UTC 25 Sep, at the time of the splashdown of the outer-eye dropsonde. The exact location of the aircraft is shown with a white plane symbol. The outer-eye dropsonde is roughly located near the white aircraft symbol. The storm-relative position of the outer-eye dropsonde is shown in the plot at top center as in Figure 15a. There is an area of deep convection close to the sonde in (b). The spacing between the range rings is 16 n mi. The following colors equate to the following radar reflectivity values: Green - > 25 dBZ; Yellow - > 35 dBZ; Red - > 45 dBZ; and Purple - > 55 dBZ.

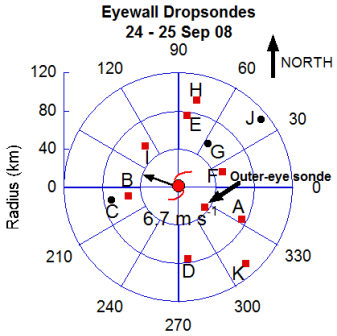

(a) Sonde K: 0013 UTC 25 Sep (b) Sonde K: 0015 UTC 25 Sep

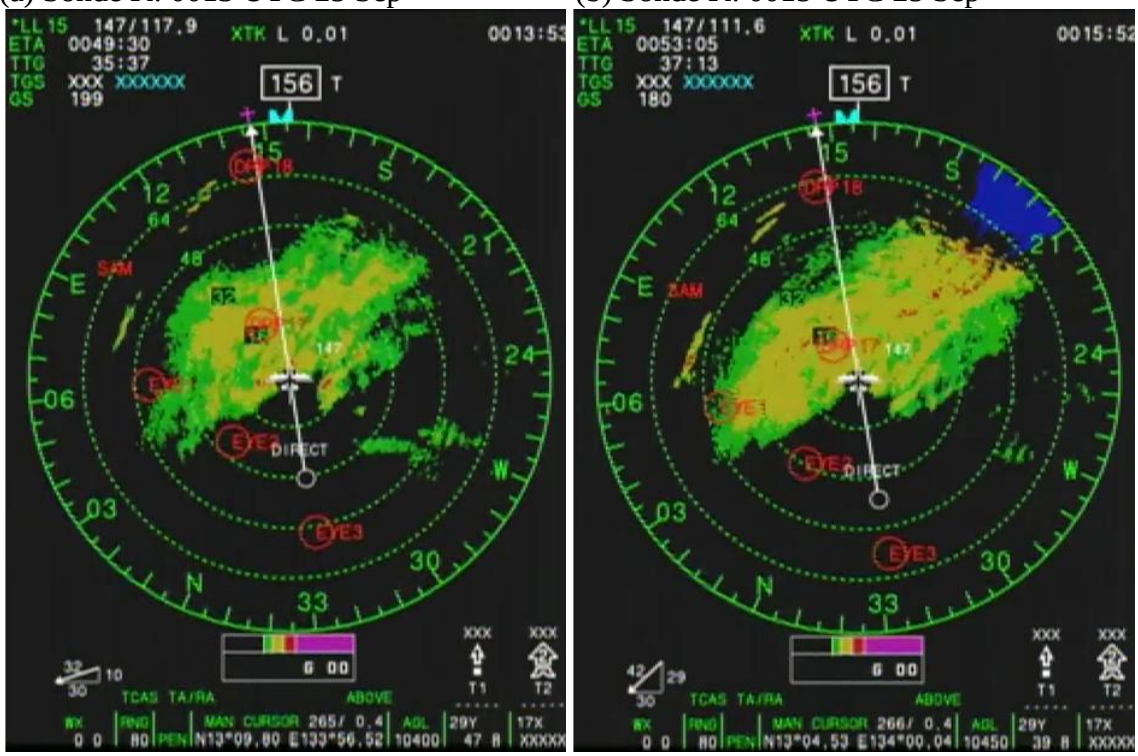

Figure 61. WC-130J aircraft radar imagery for TS Jangmi at (a) 0013 UTC 25 Sep, ~ two minutes before Dropsonde K splashed down at the ocean surface; and at (b) 0015 UTC 25 Sep, at the time of the splashdown of Dropsonde K. The exact location of the aircraft is shown with a white plane symbol. Dropsonde K is roughly located near the white aircraft symbol. The storm-relative position of the Dropsonde K is shown in the plot at top center as in Figure 15a. The dropsonde is located in an area of primarily stratiform precipitation in both radar images. The spacing between the range rings is 16 n mi. The following colors equate to the following radar reflectivity values: Green - > 25 dBZ; Yellow - > 35 dBZ; Red - > 45 dBZ; and Purple - > 55 dBZ.

LIST OF REFERENCES

Ahrens, C. D., 2007: *Meteorology Today: An Introduction to Weather, Climate, and the Environment.* 8th ed. Thomson Brooks/Cole, 537 pp.

Anthes, R. A., and S. W. Chang, 1978: Response of the hurricane boundary layer to changes of sea surface temperature in a numerical model. *J. Atmos. Sci.,* **35**, 1240–1255.

Batchelor, G. K., 1967: *An introduction to fluid dynamics.* Cambridge Univ. Press, 615 pp.

Bell, M. M., and M. T. Montgomery, 2008: Observed structure, evolution, and potential intensity of Category 5 Hurricane Isabel (2003) from 12 to 14 September. *Mon. Wea. Rev.,* **136**, 2023–2046.

_____,and M. T. Montgomery, 2010: Sheared deep vortical convection in pre-depression Hagupit during TCS08**,** *Geophys. Res. Lett.,* **37,** *L06802, doi:10.1029/2009GL042313.*

Black, P. G., 2004: An overview of CBLAST flights into Hurricanes Fabian and Isabel (2003). Preprints, 26th Conf. on Hurricanes and Tropical Meteorology, Miami, FL, Amer. Meteor. Soc., 1A.1.

_____, and Coauthors, 2007: Air–sea exchange in hurricanes: Synthesis of observations from the coupled boundary layer air–sea transfer experiment. *Bull. Amer. Meteor. Soc.*, **88**, 357–374.

Bolton, D., 1980: The computation of equivalent potential temperature. *Mon. Wea. Rev.,* **108**, 1046–1053.

Bosart, B. L., W. C. Lee, and R. M. Wakimoto (2002): Procedures to improve the accuracy of airborne doppler radar data. *J. Atmos. Oceanic Technol.,* **19,** 322–339.

Braun, S. A., 2002: A cloud-resolving simulation of Hurricane Bob (1991): Storm structure and eyewall buoyancy. *Mon. Wea. Rev.*, **130**, 1573–1592.

Bui, H. H., R. K. Smith, M. T. Montgomery, and J. Peng, 2009: Balanced and unbalanced aspects of tropical cyclone intensification. *Quart. J. Roy. Meteor. Soc.,* **135,** 1715–1731.

Chu, J. H., A. Levine, S. Daida, D. Schiber, E. Fukada, and C. R. Sampson, 2009: JTWC western north Pacific best track data. (Available online at http://www.usno.navy.mil/NOOC/nmfc-ph/RSS/jtwc/best_tracks/2008/2008s-bwp/bwp192008.txt).

Craig, G. C., and S. L. Gray, 1996: CISK or WISHE as the mechanism for tropical cyclone intensification. *J. Atmos. Sci.,* **53**, 3528–3540.

Deardorf, J. W., 1972: Parameterization of the planetary boundary layer for use in general circulation models. *Mon. Wea. Rev.*, **100,** 93–106.

Drennan, W. M., J. A. Zhang, J. R. French, C. McCormick, and P. G. Black, 2007: Turbulent fluxes in the hurricane boundary layer. Part II: Latent heat flux. *J. Atmos. Sci.,* **64**, 1103–1115.

Eastin, M. D., P. G. Black, and W. M. Gray, 2002: Flight-level thermodynamic instrument wetting errors in hurricanes. Part I: Observations. *Mon. Wea. Rev.,* **130**, 825–841.

_____, W. M. Gray, and P. G. Black, 2005: Buoyancy of convective vertical motions in the inner core of intense hurricanes. Part I: General statistics. *Mon. Wea. Rev.,* **133**, 188–208.

Elsberry, R. L., and P. A. Harr, 2008: Tropical cyclone structure (TCS08) field experiment: Science basis, observational platforms, and strategy. *Asia-Pacific J. Atmos. Sci.,* **44**, 209–231.

_____, R. R. Ferek, S. W. Chang, P. A. Harr, and D. Eleuterio, 2008: Tropical cyclone structure (TCS08) field experiment in the western North Pacific during 2008. *Extended Abstracts, 28th Conf. on Hurricanes and Tropical Meteorology,* Orlando, FL, Amer. Meteor. Soc., 7C.6.

Emanuel, K. A., 1986: An air-sea interaction theory for tropical cyclones. Part I: Steady-state maintenance. *J. Atmos. Sci.,* **43**, 585–605.

_____, 1989: The finite-amplitude nature of tropical cyclogenesis. *J. Atmos. Sci.,* **46**, 3431–3456.

_____, 1991: The theory of hurricanes. *Annu. Rev. Fluid Mech.,* **23**, 179–196.

_____, 1995: Sensitivity of tropical cyclones to surface exchange coefficients and a revised steady-state model incorporating eye dynamics. *J. Atmos. Sci.,* **52**, 3969–3976.

_____, 1997: Some aspects of hurricane inner-core dynamics and energetics. *J. Atmos. Sci.,* **54**, 1014–1026.

_____, 2005: *Divine wind: the history and science of hurricanes.* Oxford University Press, USA, 285 pp.

_____, J. D. Neelin, and C. S. Bretherton, 1994. On large-scale circulations in convecting atmosphere. *Quart. J. Roy. Meteor. Soc.*, **120,** 1111–1143.

Enagonio, J., and M.T. Montgomery, 2001: Tropical cyclogenesis via convectively forced vortex Rossby waves in a shallow water primitive equation model. *J. Atmos. Sci.,* **58**, 685–706.

Franklin, J. L., M. L. Black, and K. Valde, 2003: GPS dropwindsonde wind profiles in hurricanes and their operational implications. *Wea. Forecasting,* **18**, 32–44.

French, J. R., W. M. Drennan, J. A. Zhang, and P. G. Black, 2007: Turbulent fluxes in the hurricane boundary layer. Part I: Momentum flux. *J. Atmos. Sci.*, **64**, 1089–1102.

Garstang, M., 1979: The tropical atmospheric boundary layer: Role in the formation and maintenance of hurricanes. *Aust. Meteor. Mag.,* **27**, 229–248.

Giammanco, I. M., J. L. Schroeder, M. D. Powell, and D. A. Smith, 2008: GPS dropwindsonde observations of tropical cyclone low-level wind maxima. *Extended Abstracts, 28th Conf. on Hurricanes and Tropical Meteorology,* Orlando, FL, Amer. Meteor. Soc., P2E.1.

Gray, S. L., and G. C. Craig, 1998: A simple theoretical model for the intensification of tropical cyclones and polar lows. *Quart. J. Roy. Meteor. Soc.*, **124**, 919–947.

Guiney, J. L., 1999: Preliminary report on Hurricane Georges: 15 September - 1 October 1998. (Available online at http://www.nhc.noaa.gov/1998georges.html).

Hendricks, E. A., M. T. Montgomery, and C. A. Davis, 2004: The role of "vortical" hot towers in the formation of tropical cyclone Diana (1984). *J. Atmos. Sci.,* **61**, 1209–1232.

Heymsfield, G. M., J. B. Halverson, J. Simpson, L. Tian, and T. P. Bui, 2001: ER-2 Doppler radar investigations of the eyewall of Hurricane Bonnie during the Convection and Moisture Experiment-3. *J. Appl. Meteor.* **40,** 1310–1330.

Hildebrand, P. H., and Coauthors, 1996: The ELDORA/ASTRAIA airborne Doppler weather radar: High-resolution observations from TOGA COARE. *Bull. Amer. Meteor. Soc.,* **77,** 213–232.

Hock, T. F., and J. L. Franklin, 1999: The NCAR GPS Dropwindsonde. *Bull. Amer. Meteor. Soc.,* **80**, 407–420.

Holliday, C. R., and A. H. Thompson, 1979: Climatological characteristics of rapidly intensifying typhoons. *Mon. Wea. Rev.,* **107**, 1022–1034.

Holton, J. R., 2004: *An Introduction to Dynamic Meteorology.* Fourth ed. Academic Press, 535 pp.

Houze, R. A., Jr., W. C. Lee, and M. M. Bell, 2009: Convective contribution to the genesis of Hurricane Ophelia (2005). *Mon. Wea. Rev.,* **137,** 2778–2800.

Kaplan, J., and M. DeMaria, 2003: Large-scale characteristics of rapidly intensifying tropical cyclones in the North Atlantic basin. *Wea. Forecasting,* **18**, 1093–1108.

Kepert, J., 2001: The dynamics of boundary layer jets within the tropical cyclone core. Part I: Linear theory. *J. Atmos. Sci.,* **58**, 2469–2484.

_____, 2006a: Observed boundary layer wind structure and balance in the hurricane core. Part I: Hurricane Georges. *J. Atmos. Sci.,* **63**, 2169–2193.

_____, 2006b: Observed boundary layer wind structure and balance in the hurricane core. Part II: Hurricane Mitch. *J. Atmos. Sci.,* **63**, 2194–2211.

_____,and Y. Wang, 2001: The dynamics of boundary layer jets within the tropical cyclone core. Part II: Nonlinear enhancement. *J. Atmos. Sci.,* **58**, 2485–2501.

Kundu, P. K., 1990: *Fluid Mechanics.* Academic Press, 638 pp.

Lighthill, J., 1998: Fluid mechanics of tropical cyclones. *Theor. Comput. Fluid Dyn.,* **10**, 3–21.

Mallen, K. J., M. T. Montgomery, and B. Wang, 2005: Reexamining the near-core radial structure of the tropical cyclone primary circulation: Implications for vortex resiliency. *J. Atmos. Sci.,* **62**, 408–425.

Marks, F. D., Jr., and R. A. Houze, Jr., 1984: Airborne Doppler radar observations in hurricane Debby. *Bull. Amer. Meteor. Soc.,* **65**, 569–582.

_____, P. G. Black, M. T. Montgomery, and R. W. Burpee, 2008: Structure of the eye and eyewall of Hurricane Hugo (1989). *Mon. Wea. Rev.,* **136**, 1237–1259.

McTaggart-Cowan, R., L. F. Bosart, J. R. Gyakum, and E. H. Atallah, 2007: Hurricane Katrina (2005). Part I: Complex life cycle of an intense tropical cyclone. *Mon. Wea. Rev.,* **135**, 3905–3926.

McWilliams, J. C., and G. R. Flierl, 1979: On the evolution of isolated, nonlinear vortices. *J. Phys. Oceanogr.*, **9**, 1155–1182.

Molinari, J., D. Vollaro, and K. L. Corbosiero, 2004: Tropical cyclone formation in a sheared environment: A case study. *J. Atmos. Sci.*, **61**, 2493–2509.

Möller, J. D., and M. T. Montgomery, 2000: Tropical cyclone evolution via potential vorticity anomalies in a three-dimensional balance model. *J. Atmos. Sci.*, **57**, 3366–3387.

Montgomery, M. T., and J. Enagonio, 1998: Tropical cyclogenesis via convectively forced vortex Rossby waves in a three-dimensional quasigeostrophic model. *J. Atmos. Sci.*, **55**, 3176–3207.

_____, H. D. Snell, and Z. Yang, 2001: Axisymmetric spindown dynamics of hurricane-like vortices. *J. Atmos. Sci.*, **58**, 421–435.

_____, M. E. Nicholls, T. A. Cram, and A. B. Saunders, 2006a: A vortical hot tower route to tropical cyclogenesis. *J. Atmos. Sci.*, **63**, 355–386.

_____, M. M. Bell, S. D. Aberson, and M. L. Black, 2006b: Hurricane Isabel (2003): New insights into the physics of intense storms. Part I: Mean vortex structure and maximum intensity estimates. *Bull. Amer. Meteor. Soc.*, **87**, 1335.

_____, S. V. Nguyen, R. K. Smith, and J. Persing, 2009: Is WISHE essential for tropical cyclone intensification? *Quart. J. Roy. Meteor. Soc.*, **135**, 1697–1714.

Moss, M. S., and F. J. Merceret, 1976: A note on several low-layer features of Hurricane Eloise (1975). *Mon. Wea. Rev.*, **104**, 967–971.

Nguyen, S. V., R. K. Smith, and M. T. Montgomery, 2008: Tropical cyclone intensification and predictability in three dimensions. *Quart. J. Roy. Meteor. Soc.*, **134**, 563–582.

Ooyama, K. V., 1969: Numerical simulation of the life cycle of tropical cyclones. *J. Atmos. Sci.*, **26**, 3–40.

_____, 1982: Conceptual evolution of the theory and modeling of the tropical cyclone. *J. Meteor. Soc. Japan*, **60**, 369–379.

Oye, R., C. Mueller, and S. Smith (1995): Software for radar translation, visualization, editing, and interpolation. Preprints, *27th Conf. on Radar Meteor.*, Vail, CO, Amer. Meteor. Soc., 359–361.

Parsons, D., P. A. Harr, T. Nakazawa, S. Jones, and M. Weissmann, 2008: An overview of the THORPEX-PACIFIC Asian regional campaign (T-PARC) during August-September 2008, *Extended Abstracts, 28th Conf. on Hurricanes and Tropical Meteorology*, Orlando, FL, Amer. Meteor. Soc., 7C.7.

Pasch, R. J., A. L. Avila, and J. L. Guiney, 2001: Atlantic hurricane season of 1998. *Mon. Wea. Rev.*, **129**, 3085–3123.

Persing, J., and M. T. Montgomery, 2003: Hurricane superintensity. *J. Atmos. Sci.*, **60**, 2349–2371.

Powell, M. D., P. J. Vickery, and T. A. Reinhold, 2003: Reduced drag coefficient for high wind speeds in tropical cyclones. *Nature*, **422**, 279–283.

Rauber, R. M., J. Walsh and D. Charlevoix, 2008: *Severe and hazardous weather, an introduction to high impact meteorology*, 3rd Ed., Kendall Hunt Publishing Company, 640 pp.

Rayleigh, Lord, 1916: On the dynamics of revolving fluids. *Proc. Roy. Soc. London*, **A93,** 148–154.

Raymond, D. J., and C. Lopez-Carrillo, 2011: The vorticity budget of developing Typhoon Nuri (2008). *Atmos. Chem. Phys.*, **11,** 147–163.

Reasor, P. D., M. T. Montgomery, and L. F. Bosart, 2005: Mesoscale observations of the genesis of Hurricane Dolly (1996). *J. Atmos. Sci.*, **62**, 3151–3171.

_____, M. D. Eastin, and J. F. Gamache, 2009: Rapidly intensifying Hurricane Guillermo (1997). Part I: Low-wavenumber structure and evolution. *Mon. Wea. Rev.*, **137**, 603–631.

Rogers, R., and Coauthors, 2006: The intensity forecasting experiment: A NOAA multiyear field program for improving tropical cyclone intensity forecasts. *Bull. Amer. Meteor. Soc.*, **87**, 1523–1537.

Sanger, N. T., 2008a: Mission report for Tropical Storm Jangmi from 24 - 25 Sep 2008. (Available online at http://catalog.eol.ucar.edu/cgi-bin/tparc_2008/htmlwrap?file_url=/tparc_2008/report/usaf_c130/20080924/report.usaf_c130.200809241713.mission_summary.html).

_____, 2008b: Mission report for Typhoon Jangmi from 25 - 26 Sep 2008. (Available online at http://catalog.eol.ucar.edu/cgi-bin/tparc_2008/htmlwrap?file_url=/tparc_2008/report/usaf_c130/20080925/report.usaf_c130.200809252003.mission_summary.html).

_____, 2008c: Mission report for Supertyphoon Jangmi from 27 Sep 2008. (Available online at http://catalog.eol.ucar.edu/cgi-bin/tparc_2008/htmlwrap?file_url=/tparc_2008/report/usaf_c130/20080927/report.usaf_c130.200809270208.mission_summary.html).

Schecter, D. A., and D. H. E. Dubin, 1999: Vortex motion driven by a background vorticity gradient. *Phys. Rev. Lett.*, **83**, 2191–2194.

Shapiro, L. J., 1983: The asymmetric boundary layer flow under a translating hurricane. *J. Atmos. Sci.*, **40**, 1984–1998.

Shin, S., and R. K. Smith, 2008: Tropical cyclone intensification and predictability in a minimal three dimensional model. *Quart. J. Roy. Meteor. Soc.*, **134,** 1661–1671.

Simpson, R. H., 1952: Exploring eye of Typhoon Marge (1951). *Bull. Amer. Meteor. Soc.*, **33**, 286–298.

Smith, R. K., 2003: A simple model of the hurricane boundary layer. *Quart. J. Roy. Meteor. Soc.*, **129**, 1007–1027.

_____, and W. Ulrich, 1990: An analytical theory of tropical cyclone motion using a barotropic model. *J. Atmos. Sci.*, **47**, 1973–1986.

_____, and S. Vogl, 2008: A simple model of the hurricane boundary layer revisited. *Quart. J. Roy. Meteor. Soc.*, **134**, 337–351.

_____, and G. L. Thomsen, 2009: Dependence of tropical cyclone intensification on the boundary layer representation in a numerical model. *Quart. J. Roy. Meteor. Soc.*, **136,** 1671–1685.

_____, and M. T. Montgomery, 2010: Hurricane boundary-layer theory. *Quart. J. Roy. Meteor.Soc.*, **136,** 1665–1670.

_____, M. T. Montgomery, and S. Vogl, 2008: A critique of Emanuel's hurricane model and potential intensity theory. *Quart. J. Roy. Meteor. Soc.*, **134**, 551–561.

_____, M. T. Montgomery, and S. V. Nguyen, 2009: Tropical cyclone spin up revisited. *Quart. J. Roy. Meteor. Soc.*, **135**, 1321–1335.

_____, C. Schmidt, and M. T. Montgomery, 2011: Dynamical constraints on the intensity and size of tropical cyclones. *Quart. J. Roy. Meteor. Soc.*, in press.

Stull, R. B., 1988: *An introduction to boundary layer meteorology.* D Reidel Pub Co, 666 pp.

Testud, J., P. H. Hildebrand, and W. C. Lee, 1995: A procedure to correct airborne Doppler radar data for navigation errors using the echo returned from the Earth's surface. *J. Atmos. Oceanic Technol.*, **12,** 800–820.

Uhlhorn, E. W., P. G. Black, J. L. Franklin, M. Goodberlet, J. Carswell, and A. S. Goldstein, 2007: Hurricane surface wind measurements from an operational stepped frequency microwave radiometer. *Mon. Wea. Rev.*, **135**, 3070–3085.

Wang, B., and X. Zhou, 2007: Climate variation and prediction of rapid intensification in tropical cyclones in the western North Pacific. *Meteor. Atmos. Phys.*, **99**, 1–16.

Wang, Y., and C. C. Wu, 2004: Current understanding of tropical cyclone structure and intensity changes–a review. *Meteor. Atmos. Phys.*, **87**, 257–278.

Wikipedia, 2009 Typhoon Jangmi (2008). (Available online at http://en.wikipedia.org/wiki/Typhoon_Jangmi_(2008).

Williamson, S. P., and Coauthors, 2009: Office of federal coordinator for meteorological services and supporting research (OFCM) national hurricane operations plan. **FCM-P12-2009**, 160 pp.

Willoughby, H. E., 1988: The dynamics of the tropical cyclone core. *Aust. Meteor. Mag.*, **36**, 183–191.

_____, 1995: Mature structure and evolution. *Global Perspectives on Tropical Cyclones*, R. L. Elsberry, Ed., 1st ed. World Meteorological Organization, 21–62.

_____, and M. B. Chelmow, 1982: Objective determination of hurricane tracks from aircraft observations. *Mon. Wea. Rev.*, **110**, 1298–1305.

_____, R. W. R. Darling, and M. E. Rahn, 2006: Parametric representation of the primary hurricane vortex. Part II: A new family of sectionally continuous profiles. *Mon. Wea. Rev.*, **134**, 1102–1120.

Wissmeier U., and R. K. Smith, 2011: Tropical cyclone convection: The effects of ambient vertical vorticity. *Quart. J. Roy. Meteor. Soc.*, in press.

Yano, J. I., and K. Emanuel, 1991: An improved model of the equatorial troposphere and its coupling with the stratosphere. *J. Atmos.Sci.*, **48**, 377–389.

Zhang, D., Y. Liu, and M. K. Yau, 2001: A multiscale numerical study of hurricane Andrew (1992). Part IV: Unbalanced flows. *Mon. Wea. Rev.*, **129**, 92–107.

Zhang, J. A., W. M. Drennan, P. G. Black, and J. R. French, 2009: Turbulence structure of the hurricane boundary layer between the outer rainbands. *J. Atmos. Sci.*, **66,** 2455–2467.

THIS PAGE LEFT INTENTIONALLY BLANK

INITIAL DISTRIBUTION LIST

1. Defense Technical Information Center
   Ft. Belvoir, VA

2. Dudley Knox Library
   Naval Postgraduate School
   Monterey, CA

3. Air Force Weather Agency
   Offutt AFB, NE

4. Michael T Montgomery
   Naval Postgraduate School
   Monterey, CA

5. Roger K. Smith
   Meteorological Institute, University of Munich
   Munich, Germany

6. Texas A&M University Department of Meteorology
   Texas A&M University
   College Station, TX

7. Florida State University Department of Meteorology
   Florida State University
   Tallahassee, FL

8. Neil T. Sanger
   Air Force Global Strike Command
   Bossier City, LA